In silico investigation of the mechano-regulation of sprouting angiogenesis during bone healing

Dissertation (monograph) approved by the
Doctoral Degree Committee of
Hamburg University of Technology
in pursuit of the academic degree of

Doktor-Ingenieurin (Dr. -Ing)

written by
Chiara Dazzi

from
Lugo, Italy

2026

Reviewers:
Prof. Dr. Sara Checa Esteban
Univ.- Prof. Dr.-Ing. Georg Duda

Date of oral examination: 15.06.2026

DOI: https://doi.org/10.15480/882.17765
ORCID: https://orcid.org/0000-0002-5435-0554

Abstract

Sprouting angiogenesis – the growth of new capillaries from existing vessels – is essential during bone regeneration, as its impairment has been linked to poor bone healing outcomes. The success of bone tissue engineering approaches, such as 3D-printed scaffolds, likewise relies on achieving adequate vessel infiltration. While mechanical and structural cues such as external loading, cell-generated traction forces and scaffold architectural features are all thought to influence angiogenesis, their specific contributions and interactions remain largely unknown. The aim of this thesis was therefore to investigate the individual and combined role of mechanical and structural cues in regulating angiogenesis during bone regeneration.

To achieve this, multi-scale computer models of the mechano-regulation of angiogenesis were developed, replicating different *in vitro* and *in vivo* experiments. Finite element models at the tissue scale were used to predict the mechanical environment, while agent-based models were developed to simulate cell activities. First, a computer model of the mechanical crosstalk between endothelial and stromal cells within anisotropic scaffolds *in vitro* was developed. Second, the model was extended to simulate angiogenesis and cell organisation during early bone healing under external fixators of different stiffness. Finally, a mechanobiological computer model of angiogenesis and bone regeneration during scaffold-aided bone healing was developed, considering two different 3D printed-scaffold designs.

Comparison of *in silico* predictions with experimental data allowed to identify several mechanobiological principles behind angiogenesis during bone healing. *Durotaxis,* the tendency of cells to migrate toward stiffer regions, appeared to guide vessel and cell organisation within aligned pores. Strain levels induced by cell traction forces could explain vessel elongation through the scaffold pores, while the spatial distribution of cell traction forces appeared to govern vessel branching. *In vivo*-like external loads were found to overrule cell-cell interactions mediated by cell traction forces during early bone healing, with the principal strain magnitude and orientation modulating vessel patterning within the healing region. Finally, pore size, porosity and surface area-to-volume ratio emerged as key regulators of the local mechanical environment, angiogenesis and bone regeneration within scaffolds.

Future work should aim to further corroborate and generalise the current findings by extending the models across experimental settings. The knowledge gained could be used to inform the development of treatment strategies to enhance angiogenesis and, ultimately, bone healing.

Contents

Abbreviations

ABM	agent-based model.
Blebb	nitro-blebbistatin.
Ctrl	control.
ECM	extracellular matrix.
EC_MR_KO	inhibition of tip ECs mechano-response.
ECs	endothelial cells.
FDM	fused deposition modelling.
FE	finite element.
FEM	finite element method.
LPA	lysophosphatidic acid.
MEW	melt electrowriting.
MSCs	mesenchymal stromal cells.
nnHA	nano-needle hydroxyapatite.
OVSC_TF_KO	inhibition of OVSCs traction forces.
OVSCs	outer-vascular stromal cells.
PCL	polycaprolactone.
RE	relative error.
TFM	traction force microscopy.
Y27	Y-27632 dihydrochloride.
μCT	micro-computed tomography.

1

Introduction

1.1 Clinical motivation

Sprouting angiogenesis is the growth of new capillary vessels out of pre-existing ones, and it constitutes a fundamental physiological process during the development and regeneration of many tissues, including bone [1]. Bone is a highly vascularised tissue with the remarkable capacity to regenerate after injury [1]. After a bone injury, blood vessels crossing the fracture line are disrupted, and the vascular network needs to be re-established to allow oxygen, cells and growth factor supply. The lack or inhibition of angiogenesis results in delayed healing or even a non-union (i.e., fractures that do not heal) [2, 3]. More precisely, non-unions account for approximately 10% of all fractures, but this rate increases to 46% when fractures are associated with significant vascular impairments [4].

Vascularisation also plays a crucial role in bone tissue engineering approaches, aiming at developing bone substitutes, such as 3D bone scaffolds, to replace large bone losses. Despite 3D scaffolds proved to be promising in enhancing tissue regeneration, revascularisation of large 3D scaffolds is one of the main obstacles to their clinical application. Vessel invasion is often too slow to provide adequate oxygen levels and nutrients to the cells, as well as waste removal, resulting in cell death in the interior of large scaffolds.

There is a clinical need to develop bone regeneration treatment strategies that effectively target angiogenesis and vessel growth. To tackle this, a comprehensive understanding of the processes influencing sprouting angiogenesis during bone regeneration is indispensable. Although it is known that angiogenesis is highly sensitive to the biological,

chemical and mechanical microenvironments, the regulatory function of structural or mechanical signals is not fully understood.

1.2 Background

1.2.1 Angiogenesis during bone healing

Upon bone injury, the timely re-establishment of a functional vascular network through sprouting angiogenesis is essential for supporting effective bone healing. The vascular response originates from vessels in the periosteum (bone's outer layer), bone marrow (soft tissue inside the bone) and adjacent tissues, with a stronger response observed from the periosteum [5]. Bone regeneration is a highly dynamic and complex process in which the different phases are interwoven and overlap both in time and space. For simplicity, four main stages are identified to describe the bone healing process, from the fracture opening to the full restoration of the bone original function [6, 7] (Fig. 1.1 A): inflammatory or hematoma phase, soft callus phase, hard callus phase and remodelling phase.

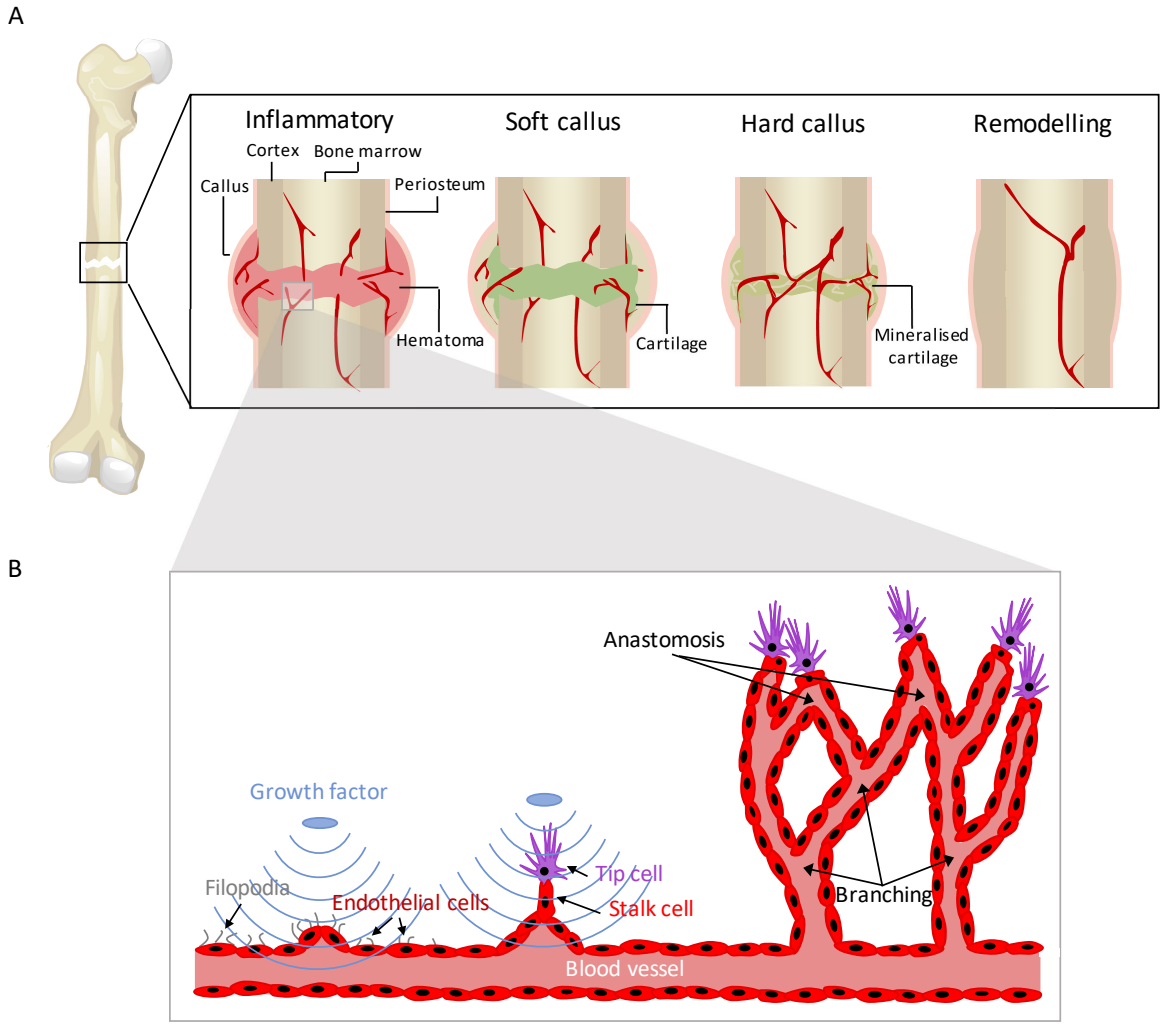

Figure 1.1: Schematic of bone healing and angiogenic processes. ***(A)*** *Magnified view of the fracture site illustrating the four main phases of bone healing.* ***(B)*** *Magnified view of a sprouting vessel at the fracture site depicting the key events of sprouting angiogenesis.*

Following bone fracture and blood vessel disruption, a hematoma forms at the onset of healing (first hours), followed by an inflammatory response. During early inflammation, immune cells are recruited to the injured site and secrete signalling molecules that initiate the healing process, such as growth factors (e.g., vascular endothelial growth factor, VEGF) that attract directional sprouting. Endothelial cells (ECs) within existing blood vessels migrate into the extra-cellular matrix (ECM) and form sprouts that elongate and eventually mature into new vasculature according to the following steps (Fig. 1.1 B): (i) a "tip" EC is selected; (ii) "tip" cell extends filopodia (membrane protrusions) sensing the haptotactic (e.g., fibre guidance), chemotactic (e.g., VEGF gradient) and mechanical cues in the environment and leads the newly formed sprout composed of following and proliferating "stalk" ECs; (iii) the newly formed sprout, or branch, can then connect with another sprout

in a process called anastomosis, which results in the formation of a closed loop allowing the initiation of blood flow [8]. During the inflammatory phase, several cells, including Mesenchymal Stromal Cells (MSCs), are recruited to the healing site. Around 7 days post-fracture, MSCs start differentiating into chondrocytes and osteoblasts, promoting the formation of a soft callus that stabilises the fracture. Thereafter, cartilage hypertrophy induces a second wave of vascularisation through sprouting angiogenesis, and the vascular network continues to be dynamically remodelled until complete bone regeneration is achieved. The cartilaginous callus is mineralised and resorbed through endochondral ossification (bone formation from a cartilage template), resulting in the formation of a hard callus. Lastly, the remodelling phase adapts the mineralised callus to the original bone shape through a slow process that takes months to years to be completed.

1.2.2 Influence of mechanics on angiogenesis during bone healing

Mechanics plays a fundamental role during sprouting angiogenesis [9-11]. Through mechano-sensing mechanisms, ECs within a vessel sense and convert mechanical signals (e.g. stresses, strains, substrate stiffness) intracellularly into biochemical signals and adapt their behaviour (e.g. migration, proliferation) [9]. The mechanical environment perceived by ECs within a bone fracture is highly complex and dynamic. In the clinical scenario of bone healing, mechanical strains within the ECM are determined not only by the patient's physical activity, but also by the gap size, tissue mechanical properties and the mechanical stability of the fracture fixation system. These can be defined as "external" mechanical cues, meaning they originate from outside the cell. In addition, ECs and outer-vascular stromal cells (OVSCs, a heterogeneous class of cells that make up the connective tissue, e.g. fibroblasts, MSCs [12]), pull on the ECM to move forward during migration, thereby contributing to the ECM deformation [13, 14]. These can be defined as "cell-induced" mechanical cues, as they are produced by the cells themselves. Several experimental studies have attempted to shed light on the role of external and cell-induced mechanical cues on angiogenesis, and relevant findings are summarised in the next paragraphs. However, how these dynamic mechanical signals acting at different scales (cells and tissues) interact to drive sprouting angiogenesis during bone healing remains largely unknown.

1.2.2.1 Influence of external mechanical cues on angiogenesis

Experimental studies have shown that externally applied boundary conditions influence vessel sprouting, elongation and alignment during angiogenesis. Specifically, intermediate levels of mechanical strains foster angiogenesis while too high mechanical strains hinder vessel growth and sprouting [15-18]. In order to minimise the stress experienced by the cells, vessels align orthogonal to the load direction in highly strained regions [19-22]. In addition, the mechanical properties of the substrate, such as the local stiffness, are sensed by cells and impact their response. For example, both ECs and OVSCs tend to migrate and reorient towards stiffer regions, a behaviour known as the *durotaxis phenomenon* [9, 23]. It is important to mention that ECM fibres, including fibronectin and collagen, offer topological cues that direct cell migration and vessel growth through contact guidance [24]; however, this specific aspect was not directly addressed in this thesis.

1.2.2.2 Influence of cell-induced mechanical cues on angiogenesis

On a microscopic level, migrating cells exert appreciable traction forces on the ECM and the induced ECM deformation can impact the behaviour of surrounding cells. OVSCs are thought to support vessel formation and organisation [25] and cell traction forces appear to be key in this interaction. Inhibition of OVSC traction forces resulted in a damaged vascular network [26], while an increase in cell traction forces promoted sprout formation [27]. These experimental observations suggest that a complex mechanical interplay exists between ECs and OVSCs via ECM deformation; however, their role in angiogenesis during bone healing remains to be elucidated.

1.2.3 Angiogenesis within scaffolds to treat large bone defects

1.2.3.1 Bone scaffolds as a treatment for large defects

Bone defects exceeding a critical size, also known as large defects, result in non-unions [28]. Current treatment approaches such as autologous bone grafting, Masquelet technique and distraction osteogenesis present several drawbacks: additional surgeries, limited available amount of bone, infection risks, pain and donor site co-morbidities [28, 29]. In the last decades, tissue engineering research has focused on bone scaffolds as a treatment alternative. Bone scaffolds are 3D structures capable of enhancing the endogenous bone

regeneration capacity, which are implanted into a bone defect, usually in combination with a fixation system to bear the load. Although several preclinical and clinical studies have shown encouraging results in terms of bone regeneration within scaffolds [30-37], the lack of a functional vascular network in the interior of large scaffolds limits their clinical translation. Oxygen diffusion is limited to a distance of approximately 100-200 μm from a blood vessel. Therefore, without adequate vascular perfusion, newly formed tissue lacks nutrients and undergoes necrosis.

1.2.3.2 Influence of structural cues on angiogenesis

The structure design of bone scaffolds offers a promising approach to promote angiogenesis without the risks associated with biological approaches. Geometrical properties of the scaffolds, such as pore size, porosity, surface area and surface area to volume ratio, are all known to affect angiogenesis and bone regeneration [34, 38-49]. Medium-sized pores (470–590 μm) were reported to promote vascularisation compared to both larger pores (>590 μm) [42] and smaller pores (<400 μm) [46]. However, smaller pores and thus a higher available surface area were shown to be beneficial for cell attachment [47]. A high surface area to volume ratio is considered advantageous for bone regeneration, by optimising cell attachment [48] and cell migration [50]. Although some studies found that pores larger than 300 μm enhanced cell proliferation and migration [41], other experimental work found no significant correlation between cell proliferation and pore size [42, 45]. High porosity levels (70-80%) supported greater cell proliferation, differentiation [51] and vessel infiltration [52] compared to lower porosity values (60%).

However, these studies are often limited to a single parameter variation, ignoring the interdependency of these parameters. For example, the scaffold porosity alters its mechanical stiffness and thus affects the mechanical strains induced within the healing region. Due to the complexity of these interactions and contradicting results reported in these studies, it is difficult to derive conclusions on how to tune scaffold parameters to promote bone and vessel formation.

1.3 State of the art

1.3.1 *In silico* models of angiogenesis

Biological, chemical and mechanical cues likely have synergistic effects on angiogenesis, which are challenging to investigate through experimental approaches alone. *In silico* methods allow to systematically analyse the independent effect of various factors and thus test hypotheses in ways not possible in the laboratory. Moreover, most experimental methods have limited temporal resolutions, often providing data at only 1 or 2 time points, which is insufficient to fully understand dynamic processes such as sprouting angiogenesis during bone healing. Yet *in silico* approaches allow to analyse the system of interest at time points not sampled during the experiment.

Depending on the scientific question that the model seeks to address, two main approaches have arisen when modelling angiogenesis. In continuum models, angiogenesis is approximated as a set of processes described as continuous in space and time usually by solving systems of differential equations. These models are not suitable for studying the morphology of the growing vascular network since the cell-level details are overlooked. In discrete models, ECs and their behaviour (e.g. proliferation, migration) are explicitly represented. For example, in agent-based models, each endothelial cell is treated as an individual entity, called "agent", with computational algorithms defining sets of rules that dictate its behaviour.

The first computer models of sprouting angiogenesis emerged in the mid-1970s to investigate vessel sprouting in response to some generic tumour growth factors [53]. Over the past decades, *in silico* models of angiogenesis have provided insights into how biochemical signals, such as growth factors, influence the angiogenic process [54, 55]. For instance, these models have allowed gaining a better understanding of the regulation of intracellular signalling pathways governing tip/stalk cell selection [56-58]. Although the role of mechanical and structural signals on angiogenesis has traditionally received less attention compared to biochemical cues, a few computer models of mechanics-driven angiogenesis have been developed in recent years. These models are categorised in the Section below (1.3.2) based on the mechanical factors they consider: cell-induced traction forces and external loads. Computer models of angiogenesis within scaffolds are summarised in Section 1.3.3.

1.3.2 *In silico* models of mechanics-driven angiogenesis

1.3.2.1 Cell-induced mechanical cues

Only a few computer models of sprouting angiogenesis explicitly included cell-induced traction forces. Santos-Oliveira and colleagues [59] showed that tip EC traction forces direct sprout elongation and trigger stalk cell proliferation, essential to support continuous vessel growth. Stephanou et al. [60] identified a limited range of traction forces for which a vascular network can develop. Van Oers and colleagues [61] demonstrated that cell traction force-induced matrix strain can explain *in vitro* angiogenesis. However, these models were only partially validated and not compared to dedicated *in vitro* experiments. A coupled *in silico*/*in vitro* approach was presented Edgars et al. [62]. By introducing a more detailed description of ECM fibres and viscoelastic properties, they were able to show that tip cell traction forces align and compact ECM fibres around the sprout tip, which in turn promotes directional sprout elongation and patterning. All these models allowed to identify key mechanisms behind the cell-matrix mechanical interplay during *in vitro* angiogenesis; however, neither the effect of external loads nor the presence of OVSCs was considered.

1.3.2.2 External mechanical cues

The role of external mechanical loads, boundary conditions and matrix topology on angiogenesis has been investigated by several computational studies often coupled to *in vitro* experiments. Burke and Kelly [63] found that dynamic external loading leads to increased EC migration, proliferation and biased migration in the direction perpendicular to the applied strain. Edgar et al. [62] showed that boundary conditions and externally applied loads influence the vessel growth direction and alignment. A few studies have focused on the interaction between matrix mechanics and angiogenesis. Specifically, ECM fibre organisation was shown to impact vessel alignment and branching [64-66]. In the specific context of computer models for bone healing, a description of the angiogenic process has been traditionally included to incorporate the effect of oxygen supply by the vascular network [67-69] rather than including a description of its mechano-regulation. Checa and Prendergast [70] coupled an algorithm for the mechano-regulation of angiogenesis with a model of bone regeneration for the first time. By including a mechanics-dependent rate of vessel growth, they were able to show that high mechanical loads cause slower vascular development and delayed healing. However, the model was not

quantitatively validated against a dedicated *in vivo* study. Building upon this model, Oreilly and colleagues [71] developed a computer model of bone regeneration including mechanics-driven angiogenesis. In particular, their model accounted for the influence of principal strain direction on vessel growth orientation, although the rate of vessel growth was assumed to be constant. These studies have provided valuable insights about the influence of external mechanical signals on the process of sprouting angiogenesis; however, the role of cell-induced mechanics has been overlooked so far.

1.3.3 *In silico* models of scaffold-aided angiogenesis

In silico models have allowed to systematically investigate the effect of scaffold architectural features on angiogenesis and bone regeneration. Mehdizadeh et al. [72] developed a computer model of angiogenesis within porous scaffolds and found that larger pore size, high interconnectivity and porosity support better vascularisation. The model was further extended to investigate how the degradation behaviour of the scaffold affected vessel growth [73] but did not include the bone regeneration process. Sun and colleagues [74] developed a computer model of bone regeneration and angiogenesis within scaffolds and demonstrated that scaffold porosity played a more dominant role in both processes compared with pore size. Although these studies have helped to identify some scaffold features promoting angiogenesis during bone regeneration, the role of mechanical signals induced within the scaffold was disregarded. On the other hand, a few studies have focused on how the mechanical environment within the scaffold affected vessel growth and bone regeneration, overlooking the role of structural and geometrical signals. Checa and Prendergast [75] used a computer model of tissue differentiation and angiogenesis within a scaffold to investigate how cell seeding and mechanical loading affected angiogenesis and bone regeneration. This model was adapted by Sandino et al. [76] to investigate angiogenesis and bone regeneration within an irregular scaffold morphology. They found that excessive strains within the scaffold can inhibit osteogenesis by reducing vascularisation. Similarly, Wang et al. [77] presented a model of bone regeneration within a scaffold including angiogenesis and proposed a synergistic effect between mechanical stimulation and VEGF in promoting bone regeneration and angiogenesis. A comprehensive computer model of angiogenesis during scaffold-aided bone regeneration including the influence of both mechanical and structural cues is still missing. Moreover, although these

models showed qualitative alignment with existing biological and experimental evidence, they were not directly validated against experimental data specific to these studies.

In summary, in the last decades computer models of angiogenesis have attempted to incorporate the effect of mechanical and structural signals, although they usually included a single aspect rather than analysing the interdependency of these factors. Moreover, although coupled *in vitro*/*in silico* approaches are powerful tools to identify principles behind the mechano-regulation of angiogenesis, coupling *in silico* models to *in vivo* studies offers a more realistic setting to gain knowledge that can effectively inform the development of new treatment strategies. In addition, only a few computer models of angiogenesis have been developed in the context of bone regeneration.

1.4 Thesis objectives and hypotheses

The main goal of this PhD thesis was to investigate the role of mechanical and structural cues on angiogenesis during bone regeneration through multi-scale *in silico* models coupled to *in vitro* and *in vivo* experiments. To achieve the overall goal, the following three objectives were defined (Fig. 1.2):

1. To investigate the mechanical interplay between ECs and OVSCs on sprout patterning within anisotropic scaffolds
2. To understand the relative contribution of cell-induced and external loads on sprout patterning at the onset of bone regeneration
3. To investigate the role of mechanical and geometrical cues on sprouting angiogenesis during scaffold-aided bone defect regeneration

For each objective, key hypotheses arising from experimental findings guided my work:

Hypothesis 1: *In vitro* results of a coculture of ECs and OVSCs within an anisotropic scaffold showed a preferential alignment of vessels and OVSCs. Moreover, vessel patterning differed upon modulating OVSCs traction forces. I hypothesised that *durotaxis* (the preference of cells for stiff environments) can explain vessel and cell alignment, whereas OVSCs mechanics and morphology regulate vessel sprouting.

Hypothesis 2: A mouse osteotomy stabilised with external fixators exhibited variations in vessel density and alignment after 7 days, depending on the stability of the fixation system (rigid vs. semirigid). I hypothesised that external loads primarily drive angiogenesis over

cell-induced mechanics, and the strain magnitude and orientation induced within the healing region can explain vessel patterning during early bone healing.

Hypothesis 3: Experimental data of large bone defects in rats augmented with scaffolds showed that scaffolds with different architectures led to different levels and patterns of bone regeneration and revascularisation. I hypothesised that not only the scaffold architecture but also the induced mechanical environment within the scaffold pores orchestrates bone regeneration and angiogenesis.

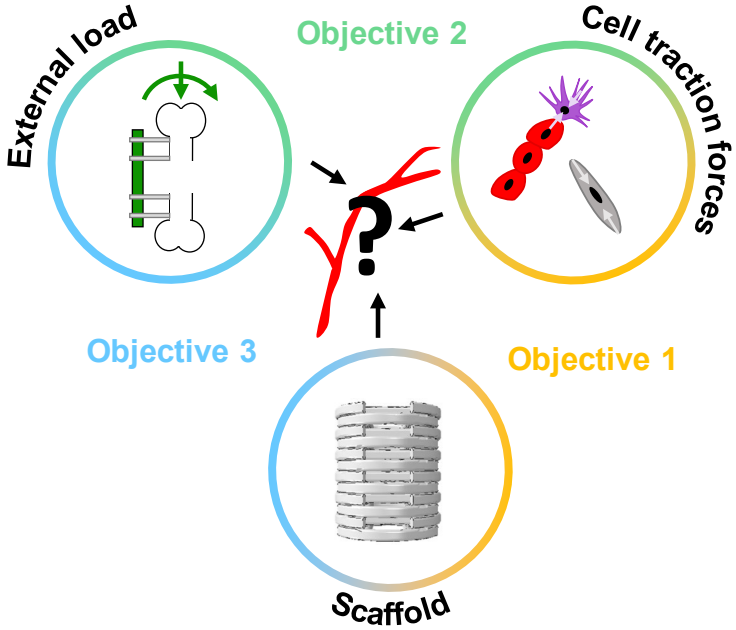

Figure 1.2: Schematic overview of the three thesis objectives. *Each objective of this thesis explores the interplay between two cues (mechanical or geometrical) that regulate angiogenesis: 1) scaffold architecture and cell-traction forces, 2) cell traction forces and external loads, 3) external loads and scaffold architecture.*

1.5 Thesis outline

Chapter 1 introduced the clinical motivation for this work, together with the scientific background, state of the art, and the three objectives of the thesis. **Chapter 2** describes the computer models and algorithms developed in this thesis, first outlining the general framework common to all models and then detailing the three different models tailored to replicate the respective experiment. The results obtained for the different thesis objectives are presented and discussed in three different chapters: *in silico* modelling of the mechanical interaction between ECs and OVSCs on sprout patterning within scaffolds in **Chapter 3**, *in*

silico modelling of the relative contribution of cell-induced and external loads on sprout patterning at the onset of bone regeneration in **Chapter 4**, and *in silico* modelling of the role of mechanical and geometrical cues on sprouting angiogenesis during scaffold-aided bone defect regeneration in **Chapter 5**. Finally, **Chapter 6** summarises the main conclusions and provides perspectives for future research. An overview of the thesis structure is depicted in Figure 1.3.

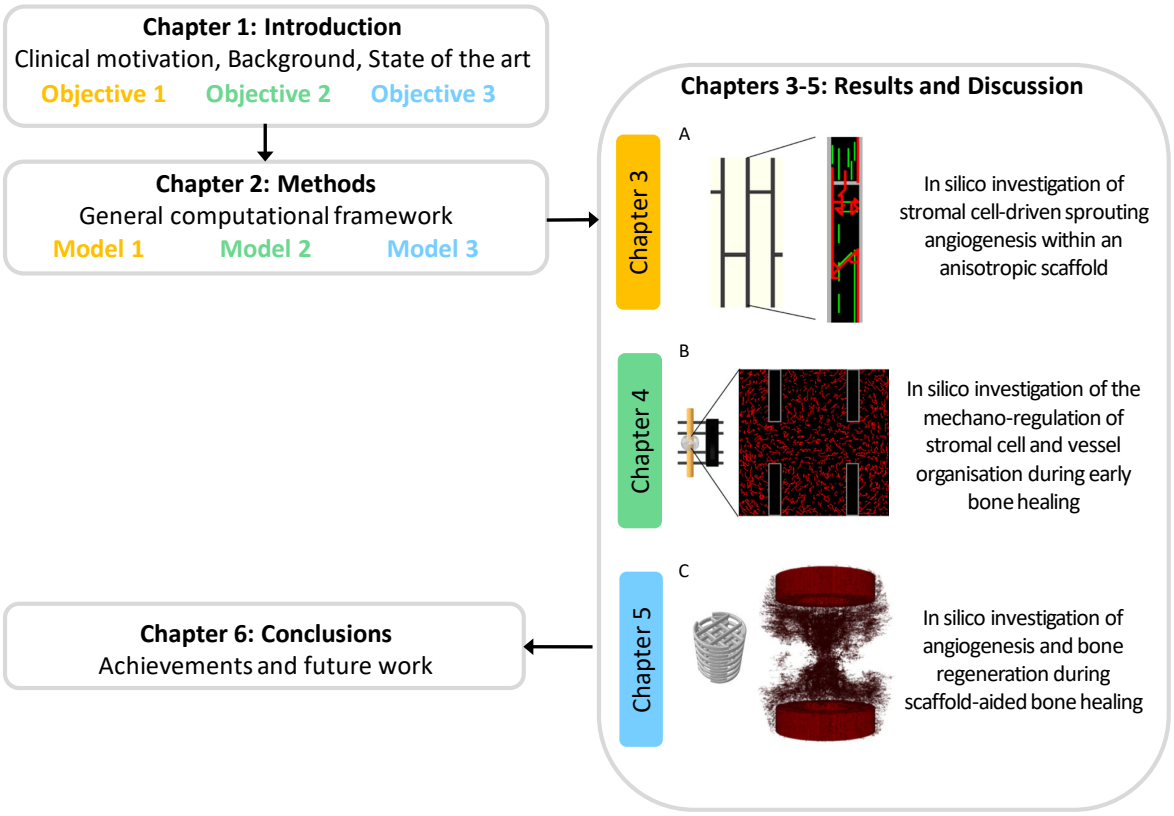

Figure 1.3: Thesis outline. ***(A)*** *predicted cell (green) and vessel (red) organisation within a scaffold pore,* ***(B)*** *predicted early vessel patterning within the healing region,* ***(C)*** *predicted vessel infiltration within a scaffold.*

2

Methods

This chapter will describe the methods used in the thesis. Three computer models were developed to address the three research questions outlined in the previous chapter. Despite relying on the same computational framework coupling mechanical signals to biological processes, described in Section 2.1, each computer model replicates a different experimental setup. The computer model developed for each objective will be detailed in a separate Section. The specific features of each one of the three computer models are summarised in Table 2.1.

Model name	Experiment type	Healing phase	Cell types	Mechanical / structural cues	Cell activities	Model dimension
In silico model of stromal cell-driven sprouting angiogenesis within an anisotropic scaffold	*In vitro*	Initial (2 weeks)	• fibroblasts • ECs	• cell traction forces • scaffold geometry	• cell migration • cell reorientation • angiogenesis	2D
In silico model of stromal cell and vessel organisation during early bone healing	*In vivo*	Initial (1 week)	• generic OVSCs • ECs	• external loads • cell traction forces	• cell migration • cell reorientation • cell proliferation • cell apoptosis • angiogenesis	2D
In silico model of angiogenesis and bone regeneration during scaffold-aided bone healing	*In vivo*	Full (12 weeks)	• MSCs • fibroblasts • osteoblasts • chondrocytes • ECs	• external loads • scaffold geometry	• cell migration • cell differentiation • cell proliferation • cell apoptosis • angiogenesis	3D

Table 2.1: Summary of the computer model features. *For each computer model, the table specifies the corresponding experiment type (in vitro vs. in vivo), temporal scale (initial vs. full bone healing), relevant cell types, mechanical and structural cues considered, cellular activities included, and model dimensionality.*

2.1 Multi-scale *in silico* models of angiogenesis coupling mechanics and biology

2.1.1 General computational framework

Multi-scale *in silico* models of the mechanobiological regulation of angiogenesis were developed to investigate the mechanical regulation of angiogenesis in the context of bone regeneration. To achieve this, Finite Element (FE) models at the tissue scale, investigating the mechanical environment, were coupled to Agent-Based Models (ABMs) at the cell scale, describing the cellular activity. FE models were built through the commercial finite element solver Abaqus (Abaqus 3DEXPERIENCE R2019x) to replicate the geometry, tissue properties, loading and boundary conditions of the experimental setup. ABMs consist of algorithms, written in C++, describing how various agents (i.e., cell types) respond to mechanical stimuli according to sets of rules derived from the available literature and/or findings from the dedicated experiments. The two model layers accounting for biology and mechanics are coupled iteratively to represent the mechanobiology of angiogenesis in bone regeneration. A schematic of the flow of information between the ABMs and FE models is depicted in Figure 2.1. Initially, the ABM space is seeded with cells so as to replicate the initial condition of the simulated experiment. The output of the ABM is the cell distribution and organisation within the domain, which informs the FE models in terms of loading conditions (cell traction forces) or tissue properties based on the cell distribution. Abaqus analysis is executed automatically as a BATCH process and the output is the mechanical environment within the simulated domain. The outputted mechanical signals (stresses, strains, fluid flow velocity) are read by the ABM and influence cell activities. The updated cell distribution and organisation (ABMs outputs) affect loading conditions or tissue properties defined in the new FE model. Iterations continue until the end of the simulation, so as to replicate the total duration of the experiment, with one iteration representing from 20 minutes to 1 day of real time, depending on the temporal scale of simulated events. Model predictions were compared to the respective experimental study.

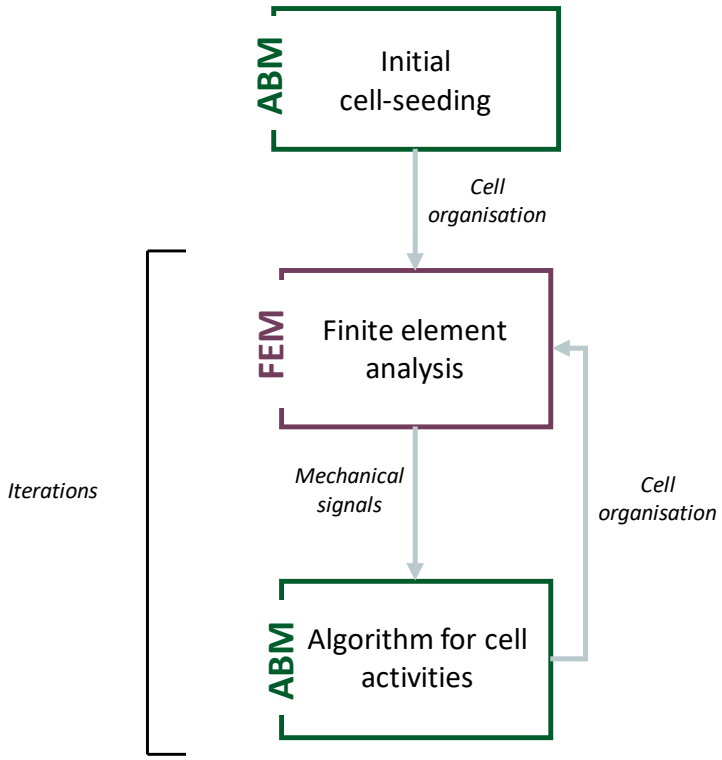

Figure 2.1: Computer model general framework. *ABM boxes indicate steps performed within the agent-based model, FEM box indicates steps performed by the finite element model. Arrows represent the flow of information between the two model layers.*

2.1.2 Baseline cell activity algorithms

The baseline cell activities included in each computer model, as summarised in Table 2.1, were derived from the available literature. Even though most cellular activities are shared, each computer model includes specific cell behaviours related to the distinct experimental conditions. For example, cell differentiation is included in the computer model simulating the full bone healing process only, since the *in vitro* experiment included already differentiated cells (fibroblasts and ECs), while the early bone healing model simulates only the first week of healing, during which differentiation has not yet started. The implementation details for each computer model are presented in the respective Sections.

2.1.2.1 Agents

The ABMs consisted of 2D or 3D lattice grids of potential positions for agents (Fig. 2.2). Each agent represented an individual cell. Vessels were modelled as a sequence of ECs occupying subsequent lattice points, with a tip EC leading the vessel.

In the 2D ABMs, two types of agents (i.e., cells) were included: OVSCs (e.g. fibroblasts) and ECs. Both OVSCs and tip ECs were assumed to apply traction forces. OVSCs, such as fibroblasts, are usually considered to behave like active force dipoles [78, 79]. The configuration of traction forces exerted by ECs was derived from 3D Traction Force Microscopy (TFM) data of small angiogenic sprouts composed of 2–3 ECs. These data were complemented with finite element analyses to identify the traction force distribution that most accurately reproduced the experimentally measured matrix deformations (Appendix B.1). The contractile behaviour of tip ECs was best approximated by an active force dipole as well. Two traction forces were applied onto the tip ECs and OVSCs lattice points adjacent to each cell core, aligned along the dipole direction and directed towards the cell core (Fig. 2.2). Stalk ECs were assumed to exert no traction forces since negligible ECM deformations have been observed experimentally near stalk cells as compared to those generated close to the sprout tips [57,58]. Both tip ECs and OVSCs could assume four possible orientations in the plane, measured counterclockwise from the x-axis: horizontal or 0° (along the x-axis), vertical or 90° (along the y-axis), diagonal right or 45° and diagonal left or 135°.

In the 3D ABMs, cells were modelled as volumetric entities occupying positions within the 3D lattice grid (Fig. 2.2). Cell types known to be relevant throughout the bone healing progression were included in the model: MSCs, fibroblasts, chondrocytes, osteoblasts, ECs.

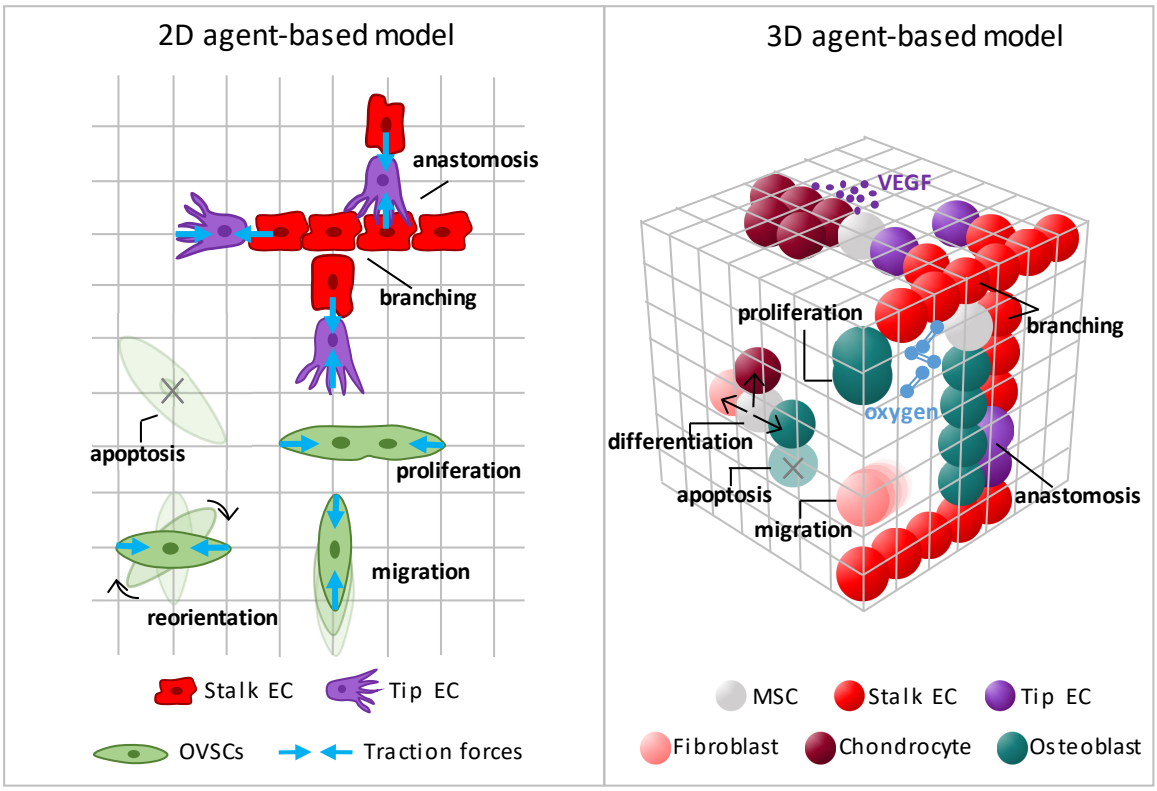

Figure 2.2: Schematic of the agent-based models. *The 2D (left) and 3D (right) lattice grids are shown, highlighting how cells are represented for each dimensionality. The baseline cellular activities included in the models are illustrated.*

2.1.2.2 Cell migration

Baseline cell migration was implemented as a random walk. Essentially, at each iteration, a new position was randomly picked for each migrating cell among its adjacent neighbour locations. If the position was free, the cell was moved there.

2.1.2.3 Cell reorientation

Cell re-orientation was modelled as driven by *durotaxis* [80] since OVSCs, like fibroblasts, have been reported to probe the local deformation [9] and to change their position and orientation towards areas of highest stiffness (*durotaxis*) [23]. To implement this, an intermediate status was introduced within each iteration, allowing fibroblasts to jump to a temporary random location with a random orientation. An intermediate FEA was run to compute the deformation induced by cell contractile activity in the temporary configuration. At the end of the intermediate step, cells measure the local effective stiffness and either adopt the intermediate configuration (if the effective local stiffness is higher than in the previous configuration) or not.

2.1.2.4 Cell differentiation

"Mature" MSCs aged at least 6 days, considered to be the maturation age [75], were implemented to differentiate. MSCs differentiation into fibroblasts, chondrocytes, and mature or immature osteoblasts was governed by the mechano-regulation theory proposed by Prendergast et al. (1997), which relates phenotype commitment to the local mechanical stimulus, defined by octahedral shear strain and fluid flow velocity [81]. ECM deposition was not directly modelled; however, its effect was incorporated during MSCs differentiation as the newly created cell type will further deposit its corresponding ECM. The model also includes a resorption zone, where tissue is resorbed and cells are removed from the lattice grid.

2.1.2.5 Cell proliferation and apoptosis

To implement cell proliferation and apoptosis, at each iteration, the total number of cells was tracked and the number of cells to proliferate and undergo apoptosis was computed. Cells that would undergo proliferation were then randomly picked until the number was reached, and a new random position adjacent to the original cell was chosen for the daughter cell. Subsequently, cells that would undergo apoptosis were randomly selected and removed from the lattice grid.

2.1.2.6 Angiogenesis

To model angiogenesis, three main events were considered: (1) sprout elongation, (2) the formation of a new sprout from an existing one (branching), and (3) the fusion of the sprout tip to another sprout (anastomosis). Vessel growth direction was determined by the leading tip ECs, known to probe the surrounding environment through filopodia (cell membrane protrusions) and respond to guidance cues by determining the directionality of vessel growth [82], while following stalk cells proliferate and occupy the positions left empty. The vessel growth rate was assumed to be higher during the first 15 days, in agreement with the experimental observation that vessels grow faster during the early healing phase [83]. Vessel branching was modelled as a stochastic process where the probability of a sprout to branch out from a parent vessel is proportional to the vessel length, based on Checa & Prendergast, 2009 [70]. When the leading tip EC encounters an EC belonging to another

vessel or its own segment, the two vessel segments fuse in the process of anastomosis and the EC loses its tip phenotype.

2.2 *In silico* model of stromal cell-driven sprouting angiogenesis within an anisotropic scaffold

The first objective of this thesis was to investigate the mechanical interplay between ECs and OVSCs on sprout patterning within an anisotropic scaffold.

2.2.1 Simulated *in vitro* experiment

A cylindrical collagen scaffold (diameter=4 mm, height=3 mm, axial stiffness=4 kPa) was fabricated with highly aligned channel-like pores (Fig. 2.3 A) with an average diameter of 101±30 μm. The scaffold was co-seeded with ECs (1 part, human umbilical vein endothelial cells) and fibroblasts (5 parts, primary human dermal fibroblasts) embedded within a fibrin gel, at an overall concentration of 7500 cells/mm^3. After 1 week of culture, chemical modulators of cell traction forces were administered to investigate the effect of changes in cell mechanics on sprouting angiogenesis. The scaffolds were kept in culture with chemical modulators for another week, for a total experimental time of 2 weeks. Specifically, the following chemical modulators were used: (1) LPA, known to increase cell traction forces; (2) Y-27632, known to decrease cell traction forces; (3) nitro-blebbistatin, another inhibitor of cell traction forces. In the remaining of the thesis, the chemical modulators will be referred to as **"LPA+"**, **"Y27-"**, and **"Blebb-"**, respectively, with the positive or negative sign indicating their effect on cell traction force magnitude. **"Ctrl"** refers to the control experiment, without any chemical modulator. Traction force magnitude and distribution exerted by cells in the different cases were calculated through 2D TFM experiments (Fig. 2.3 B). Histological images of the middle section of the scaffold were analysed in terms of cell alignment and vascular morphological features after 1 and 2 weeks.

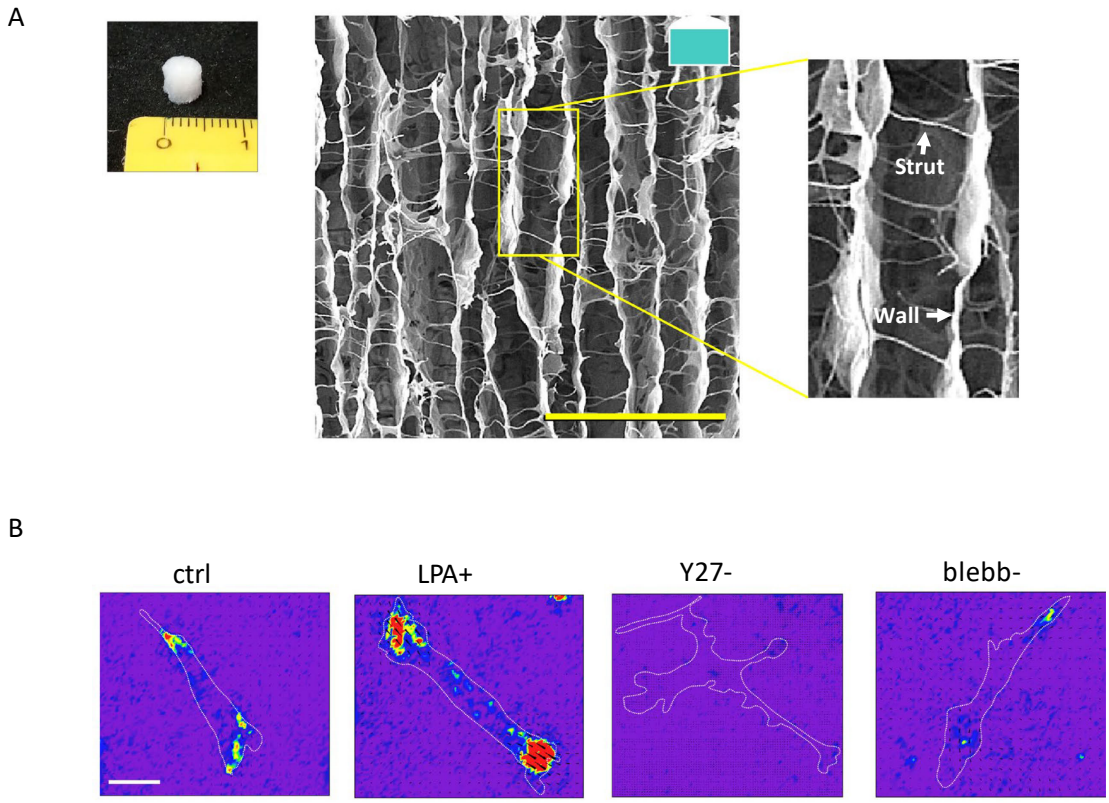

Figure 2.3: In vitro macroporous scaffold and 2D TFM data. ***(A)*** *Macroporous scaffold with magnifications illustrating the struts and walls. Scale bar 500 µm.* ***(B)*** *Reconstructed stress magnitude maps with overlaid displacement vectors (black arrows) from Traction Force Microscopy data of individual cells, either untreated (control) or treated with LPA+, Y27-, blebb-. Scale bar 50µm.*

2.2.2 Model-specific computational framework

A mechanobiological computer model of stromal cell-driven sprouting angiogenesis within the macroporous collagen scaffold was developed. The computational framework described in Section 2.1 was adapted to iteratively integrate mechanical signals, generated by cell contractile activity within the scaffold pores, with the cell biological responses, including cell migration, re-orientation and vessel growth. The simulations were run for 42 iterations, each one corresponding to 8 hours, to cover the 14 days of the experiment. The two model layers accounting for the mechanics and the biology are detailed in the following paragraphs.

2.2.3 Finite Element Model (mechanics)

FE models were built to predict the mechanical environment within the scaffold pores.

2.2.3.1 Geometry

The mid-cross-section of the macroporous collagen scaffold was modelled based on the experimental average dimensions (Fig. 2.4). A 4mm x 3mm rectangular area, consisting of 100 µm-apart collagenous walls defining the channel-like pores and connected by strut elements, was replicated. The average wall and strut thicknesses (2.3 µm) were measured experimentally [84] (Fig. 2.4). The number of struts per pore was calculated based on the average strut density (3626 struts/mm^3, [85]) and resulted in 2.5 struts/pore. Therefore, pores featuring 2 or 3 struts were alternated (Fig. 2.4).

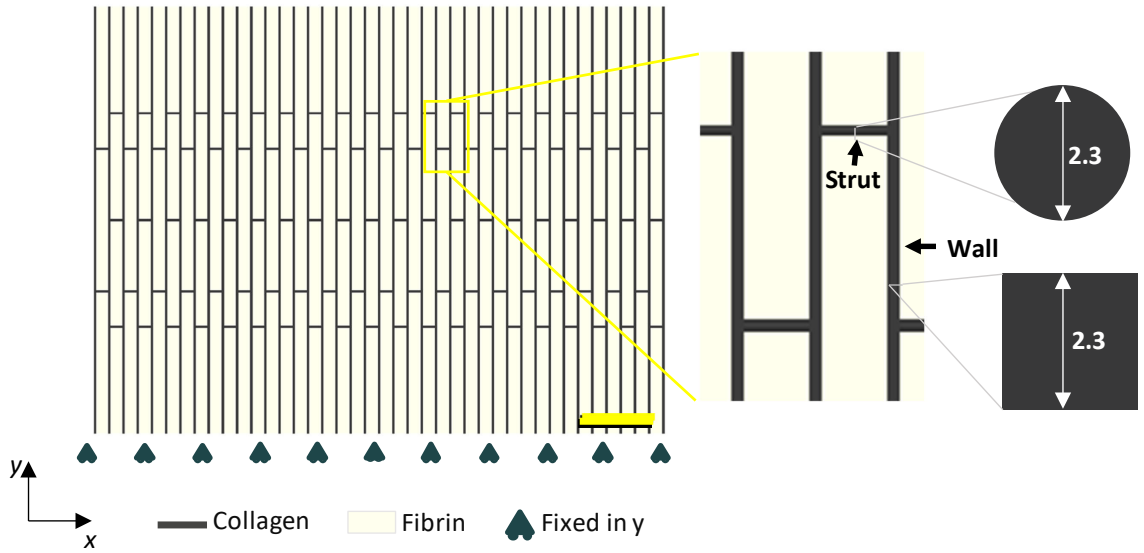

Figure 2.4: In silico macroporous scaffold. *In silico geometry of the scaffold with a magnification showing struts, walls and their cross-sections. All measures are in µm. Scale bar 500 µm.*

2.2.3.2 Mesh

Collagenous walls and struts were modelled as beam elements (Abaqus element type B21). Beam elements discretising the walls were assigned a rectangular profile since they represent the wall's longitudinal section, while those discretising the struts were assigned a circular profile. The space filled by fibrin gel within the scaffold pores was discretised with 4-node plane strain solid elements (Abaqus element type CPE4R). Plane strain elements were used as the geometry is extended in the out-of-plane direction and the section modelled lies in the central region, away from boundaries where 3D effects may be significant. Beam and solid elements shared common nodes to ensure proper mechanical coupling between the scaffold walls and the substrate. A custom MATLAB script (R2020b) was used to generate the Abaqus input file (*.inp), enabling a precise definition of nodal

positions and element connectivity. The distance between adjacent nodes was set to 0.01 mm and a mesh convergence analysis was performed to ensure the robustness of the results (Appendix A.1).

2.2.3.3 Material properties

Both the collagen forming the scaffold and the fibrin gel filling its pores were assumed to behave as linear elastic materials. The collagen elastic modulus was back-calculated to obtain a scaffold mechanically equivalent to the real one along the axial direction [84]. Essentially, a mono-axial compression test was performed *in silico* along the scaffold axial direction and the collagen elastic modulus that allowed to match the scaffold's axial stiffness was 1740 kPa, which is in the range of the elastic modulus of collagen walls measured by means of atomic force microscopy in an analogous scaffold [85]. The elastic modulus of the fibrin gel was assumed to be 1 kPa [86]. All material parameters are reported in Table 2.2.

Material	**Young's modulus (MPa)**	**Poisson's ratio**
Collagen (macroporous scaffold)	1.74*	0.3
Fibrin gel	0.001[a]	0.167

[a][86], *estimated.

Table 2.2: Material properties.

2.2.3.4 Loading and boundary conditions

The bottom edge of the scaffold cross-section was fixed in y (Fig. 2.4) with the central node fixed in all the degrees of freedom, to allow the scaffold to expand and contract horizontally (along x, Fig. 2.4) throughout the simulated experiment. Fibroblast and tip ECs traction forces were modelled as concentrated loads (*CLOAD). To verify whether fibroblasts behave as active force dipoles also upon chemical modulators, preliminary simulations replicating the TFM experiments in the different scenarios (Ctrl, LPA+, Y27-, Blebb-) were performed by assigning either a dipole or an isotropic force configuration to fibroblasts. The goal was to assess whether non-axial force components were still negligible, and therefore the cell could be approximated as a dipole, or a more isotropic representation was needed. Note that, since the TFM gel is stiffer than fibrin gel (12.3 kPa vs. 1kPa) and traction forces are known to vary with substrate stiffness [87], traction force values measured experimentally were scaled proportionally. Traction force alterations induced by

the chemical modulators were incorporated into the computer model after 1 week to be consistent with the experiment.

2.2.4 Agent-based model (biology)

ABMs aimed at describing cell and vessel organisation within an anisotropic scaffold. Coordinates of finite element nodes were used to create the 2D lattice grid of potential positions for cells and traction force application points. Therefore, the distance between lattice points was equal to 0.01 mm.

2.2.4.1 Cell phenotypes and seeding

Consistent with the experimental setup, two cell types were included in the ABM: fibroblasts and ECs. Vessels were assumed to have a constant diameter of 10 μm, with a tip EC spanning distance (distance between cell traction force application points) of 20 μm, while the fibroblast spanning distance was assumed to be 60 microns, in agreement with cell dimensions retrieved from images of the cultured cells within the scaffold. In the computer model, this was implemented by applying traction forces at the nodes directly adjacent to the cell core for ECs, and three positions away from the core for fibroblasts. Fibroblast and endothelial cells were seeded only within the central pore of the scaffold, to reduce the computational cost of the simulation, as follows: 5 parts of fibroblasts (n=100) and 1 part of endothelial cells (n=20) were randomly co-seeded within the pore so as to occupy 5% of available positions, in agreement with the experimental initial cell density.

2.2.4.2 Cell activity

Fibroblast activities

Fibroblast migration and re-orientation were modelled as driven by *durotaxis* [80]. In case no available positions are present surrounding a migrating cell, the cell does not migrate (contact inhibition). The fibroblast migration rate was set to 1.25μm/h, based on the average fibroblast migration speed measured within a similar scaffold [88]. Fibroblast proliferation and apoptosis were not observed *in vitro* and were therefore excluded from the model.

Angiogenesis

Experimental observations indicated that angiogenesis began within the scaffold around days 3 to 4; therefore, ECs were modelled to be quiescent during the first 3 days. From day 4, vessels could elongate, branch and undergo anastomosis. Analogous to fibroblasts, tip EC migration and re-orientation were modelled as driven by *durotaxis*, based on the experimental literature [9], with a similar implementation as explained in Section 2.1.2.3. The baseline rate of vessel growth was assumed to correspond to the fibroblast migration rate, as experimental observations indicated comparable infiltration speeds of cells and vessels in the scaffold. Mechanical strains are known to affect endothelial cell proliferation and thus the rate of vessel growth [15-18]. Therefore, the rate of vessel growth was implemented as strain-dependent and assumed to double its value for strain magnitude between 5% to 10%. Strains above 30% were assumed to hinder vessel growth, according to the reduced vascularity observed experimentally above this strain value [89]. In an attempt to explain experimental results and better understand how fibroblast mechanics and morphology affect vessel sprouting, it was hypothesised that vessel branching is triggered by orthogonal forces, generated by the fibroblast's contractile activity, acting on the vessel body. Therefore, a branching event could happen at a specific location along the vessel if principal strains acting on that EC are orthogonal to both adjacent vessel segments. To implement this, the dot products between the principal strain vector and the orientation of the two vessel segments adjacent to the EC of interest were computed at each iteration. When both products fell below a threshold of 10^{-2}, the new sprout branched out along the direction of principal strains.

2.2.5 Output analysis and visualisation

Stochastic elements are included in the computer model, such as the initial random cell seeding and orientation assignment and the migration and re-orientation rules. Therefore, 20 realisations were run for each simulated scenario to allow statistical analyses. *In vitro* and *in silico* data are reported as mean ± standard deviation, while dots represent the individual measurements.

Histology-like images were generated from *in silico* results in Matlab (R2020b) for each scenario simulated and compared to *in vitro* histological images of the middle section of the scaffold. Cell and vessel orientation with respect to the pore long axis was computed in

Matlab (R2020b) and qualitatively compared to the experiment due to the lack of data. Relevant vascular morphological features were quantified in Matlab (R2020b) and compared with the experimental data for each simulated scenario: the number of branches per vessel, the average vessel length and the total network length.

2.2.6 Statistics

Significance was tested by the Mann-Whitney U test implemented in Matlab (R2020b), complemented with Bonferroni correction for comparison of multiple groups n>2. The level of significance was defined as $p \leq 0.05$.

2.3 *In silico* model of stromal cell and vessel organisation during early bone healing

The second objective of this thesis was to unravel the relative contribution of cell-induced and externally applied loads on sprout patterning at the onset of bone regeneration.

2.3.1 Simulated *in vivo* experiment

A 0.7-mm bone defect was created in the left femur of mice [90, 91]. The bone fragments were stabilised by either rigid or semirigid external fixation systems (MouseExFix 100% and 50%, RISystem), mounted with 4 screws. Mice (n=4 per fixation system type) were sacrificed 7 days post-surgery and histological images of the bone longitudinal section within the healing region were produced to identify vessels and quantify microvascular network parameters.

2.3.2 Model-specific computational framework

A mechanobiological computer model of stromal cell and vessel organisation during the early stage of bone healing was developed. The computational framework described for the first model (Section 2.2.2) was adapted to replicate a mouse small defect stabilised using fixators with different stiffness. FE models to predict the mechanical environment within the healing region were coupled to ABMs, describing cellular behaviours at the onset of

bone healing, such as cell migration, re-orientation, proliferation, apoptosis and vessel growth. One iteration represents a time step of 20 minutes in a cascade of mouse bone healing. Simulations were performed so as to replicate the first week post-fracture. The two model layers accounting for the mechanics and the biology are detailed in the following paragraphs.

2.3.3 Finite Element Model (mechanics)

FE models were developed to compute the mechanical environment within the healing region of a mouse bone defect stabilised with a rigid or semirigid fixator and subjected to *in vivo*-like loading. A 2D model of the healing region was derived from a previously developed and validated 3D FE model of a similar experimental setup [92], adapted to mimic the current *in vivo* experiment (Fig. 2.5 A).

2.3.3.1 Geometry

A 2.5 mm x 2.5 mm region within the mid-longitudinal section of the healing region was replicated (Fig. 2.5 A). The model includes the cortical bone ends, the bone marrow cavity and the 0.7-mm defect gap (Fig. 2.5 B). The external fixators, for both a rigid and semi-rigid fixation system, were virtually simulated using corresponding boundary conditions retrieved from the 3D model, as explained below (Section 2.3.3.4).

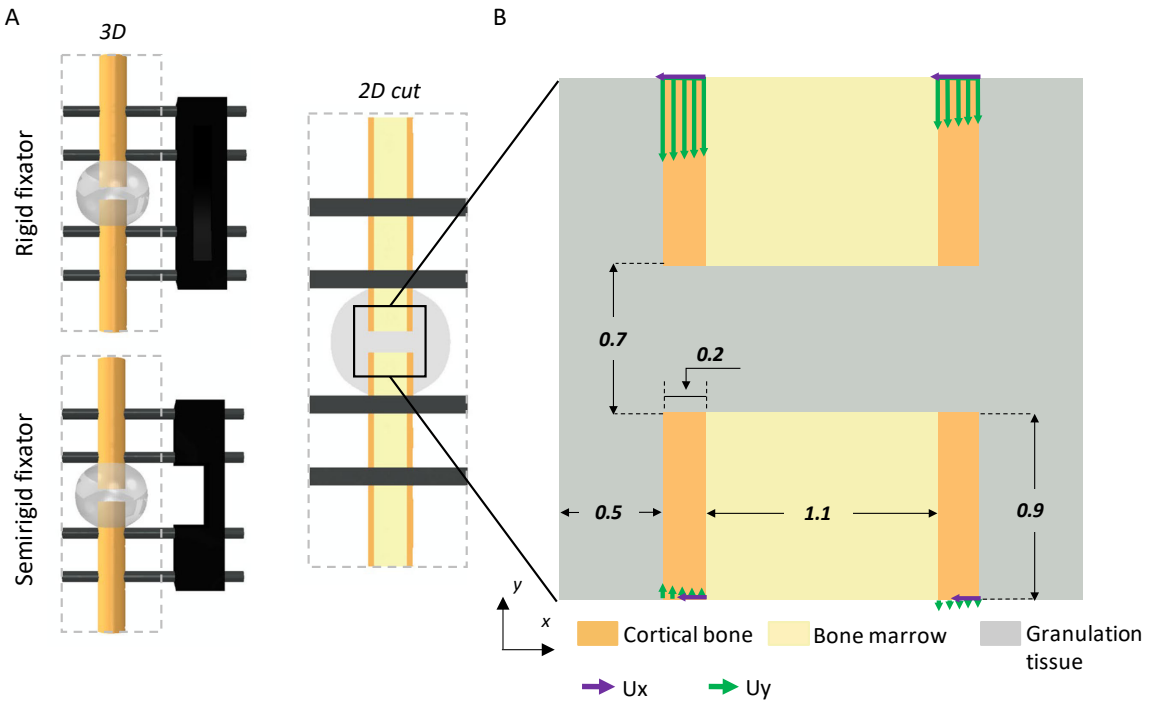

Figure 2.5: In silico geometry of the mouse osteotomy stabilised with external fixators. ***(A)*** *3D in silico model of the mouse osteotomy with a rigid (top) and semirigid (bottom) fixator, alongside a longitudinal section view (right). The black box represents the region actually simulated in this study.* ***(B)*** *2D in silico model of the mouse osteotomy illustrating the dimensions and applied displacement boundary conditions (Ux: displacement along the x-axis; Uy: displacement along the y-axis). All measures are in mm.*

2.3.3.2 Mesh

The models were meshed through a regular grid of 4-node plane strain elements (Abaqus element type CPE4), similar to the approach described in Section 2.2.3.2. A mesh convergence study was conducted for the 3D finite element model and resulted in an optimal average characteristic element size of 0.1 mm [92]. However, the distance between adjacent nodes was set to 0.01 mm to capture the mechanical effect of cell traction forces at the µ-scale.

2.3.3.3 Material properties

Linear elastic material properties were assigned to the tissues comprised within the healing region, as reported in Table 2.3. The gap and the area surrounding the cortices were assumed to be filled with granulation tissue at the onset of healing, bone marrow properties

were assigned to the marrow cavity and cortical bone properties to the cortical bone ends (Fig. 2.5).

Material	Young's modulus (MPa)	Poisson's ratio
Granulation tissue	0.2[a]	0.167[a]
Cortical bone	5000[a]	0.3[a]
Bone marrow	2[a]	0.167[a]

[a][93]

Table 2.3: Material properties.

2.3.3.4 Loading and boundary conditions

Traction forces exerted by the cells and boundary conditions mimicking the bone fragments' movements during *in vivo*-like loading under external fixators were included in the model. Similar to the model of stromal cell-driven sprouting angiogenesis within scaffolds (Section 2.2.3.4), both OVSCs and tip ECs traction forces were modelled using concentrated loads. The total traction force magnitude exerted by tip ECs and OVSCs was derived from the experimental literature [94, 95] on softer substrates. Based on the linear relationship between the substrate elastic modulus and traction force magnitude [94], the total traction force values were scaled proportionally for the granulation tissue stiffness and resulted in 32 x 10^{-6} N for OVSCs and 20 x 10^{-6} N for tip ECs.

The displacement profiles of the cortices during *in vivo*-like loading under the two different fixators were recorded from the 3D model along the two orthogonal axes of the mid-longitudinal plane. The displacement profiles were applied as displacement boundary conditions (Ux, Uy, Fig. 2.5 B) to the cortical bone fragments of the 2D model. Since a negligible tissue formation was experimentally measured during the first week post-fracture [96], displacement boundary conditions to account for the fixators and the external loading were considered acceptable.

2.3.4 Agent-based model (biology)

ABMs were developed to describe cell and vessel organisation during early bone healing. Similar to the model of stromal cell-driven angiogenesis within anisotropic scaffolds, coordinates of finite element nodes spaced 0.01 mm were used to create the 2D lattice grid of potential positions for cells and traction force application points.

2.3.4.1 Cell phenotypes and seeding

The ABM includes two types of agents: OVSCs and ECs forming the vessels. At the beginning of the simulation, ECs were initialised on 10% and 1% of lattice points in the periosteum (external to the cortical bone) and bone marrow, respectively, considering that a dominant vascular response is known to come from the periosteum [5, 97], while a diminished vessel ingrowth is generally observed from the medullary cavity [98] during early bone healing. Additionally, to mimic vessel ingrowth from surrounding soft tissues, ECs were virtually placed along a circumference of 4 mm-diameter representing the callus perimeter (Fig. 2.6). This boundary progressively contracted at the vessel growth rate, allowing ECs to occupy lattice points with a 0.5% probability, provided local EC density remained below 10% [99]. OVSCs were assumed to fill 20% of lattice points within the bone marrow and periosteum [100]. Vessels were assumed to have a diameter of 10 µm while tip ECs and OVSCs spanning distance (distance between traction force application points) was assumed to be 20 µm [101].

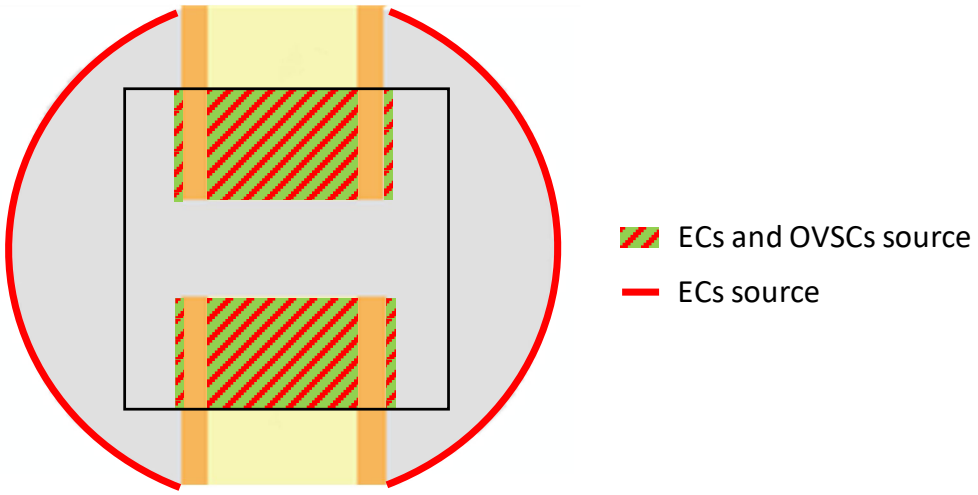

Figure 2.6: Schematic representation of the initial seeding locations within the healing region. *Regions seeded with both ECs and OVSCs are represented with a green-red pattern, the red continuous line indicates regions seeded with ECs only. The exact seeding percentages are provided in the main text. The black square outlines the simulated domain.*

2.3.4.2 Cell activity

OVSCs activities

Immediately after fracture, growth factors are released at the injured site to recruit cells and initiate the healing process. To simulate directed OVSC migration towards the fracture,

cell migration was modelled as a biased random walk favouring areas of lower cell density during the first 4 days post-surgery. Afterwards, to include cell preference for stiffer environments (*durotaxis*), OVSCs migration and re-orientation were further biased by a rule dependent on the local stiffness (Section 2.1.2.3). To correctly capture the dynamic biological response during bone healing, OVSC proliferation and apoptosis were included in the model. Since OVSCs were restrained to the 2D plane, proliferation and apoptosis rates retrieved from the literature [92] were corrected to account for daughter cells that, in 3D, could be placed out of the plane. Therefore, rates were divided by a factor of 2.25, corresponding to the ratio of accessible lattice points in 3D (18) vs. 2D (8). All cell activity rates are reported in Table 2.4.

Cell type	Proliferation rate (day^{-1})	Apoptosis rate (day^{-1})	Migration speed ($\mu m.h^{-1}$)	Vessel growth rate ($\mu m.h^{-1}$)
OVSC	0.24[a]	0.02[a]	30[b]	-
EC	-	-	-	15[c]

[a]adapted from [101], [b][102], [c][103].

Table 2.4: Cell activity parameters.

Angiogenesis

The angiogenesis algorithm used in the previous model (Section 2.2.4.2) was expanded to account for the influence of externally applied loads. The growth direction at the EC tip was determined based on three options, weighted by assigned probabilities: at each iteration, the vessel can grow (1) according to a strain-based rule (20%), (2) towards the direction of the previous iteration to account for directional persistence of vessel growth (40%), (3) towards a random direction (40%). A parameter sweep analysis was carried out to estimate the values of these probabilities in order to obtain the combination of values that better matched experimental data in terms of sprout patterning (Appendix B.2). The strain-based rule describing the mechano-response of tip ECs during early bone healing was established according to the experimental evidence. Vessels were assumed to grow along the absolute maximum principal strain (EP_{max_abs}) directions where shear strains, known to be detrimental to angiogenesis [104], are 0. It was hypothesised that vessels grew along the principal strain direction for strain values <5%, identified as the upper limit strain value for bone growth [105]. Vessels were assumed to gradually avoid the direction of maximum principal strains and align fully perpendicular for strains above 10%, as a structural response to minimise the stress experienced by the cells [19-22, 106]. Vessel growth direction (θ_{vessel}) according to the strain-based rule is described by equation 2.1:

$$\theta_{vessel}=K\theta_{EP_{max\_abs}} + (1-K)\theta_{\perp EP_{max\_abs}} \quad (2.1)$$

$$\text{with K} = \begin{cases} 1, & EP_{max\_abs} \leq 5\% \\ \frac{10\%-EP_{max\_abs}}{5\%}, & 5\% < EP_{max\_abs} < 10\% \\ 0, & EP_{max\_abs} \geq 10\% \end{cases} ;$$

EP_{max_abs}= absolute maximum principal strain; $\theta_{EP_{max\_abs}}$= absolute maximum principal strain direction; $\theta_{\perp EP_{max\_abs}}$= perpendicular to the absolute maximum principal strain direction.

Moreover, vessel growth was inhibited for strain values >30%, according to the reduced vascularity observed under cyclic compressive strains >30% at the early stage of healing [89]. To better capture the 3D nature of the callus within a 2D model, vessels were allowed to virtually grow in the 3D space. To achieve this, every 15 iterations, representing the estimated in-plane persistence time [72], tip ECs could migrate to any of the 17 neighbouring positions (7 in-plane, 10 out-of-plane). Assuming each section experienced the same, an equal number of tip ECs re-entered the 2D simulated domain in the same iteration, at random locations.

2.3.5 *In silico* experiments

In silico experiments were carried out to better understand the relative contribution of each mechanical signal (cell traction forces vs. external loads) to sprout patterning at the onset of bone healing. Therefore, mechanical signals were selectively removed from the model as explained below. In the remaining of the thesis, **"Baseline"** will refer to the mechano-biological rules explained above.

2.3.5.1 Inhibition of tip ECs mechano-response

To better understand how an altered tip EC mechano-response affects sprouting angiogenesis, we assumed that tip ECs response to mechanical signals was hampered by setting the probability to follow the strain-based rule equal to 0 and raising the probability to follow a random direction to 60%. Hereafter, this configuration will be referred to as **"EC_MR_KO"**.

2.3.5.2 Inhibition of OVSCs traction forces

To better understand the contribution of cell-induced mechanics and external loads on sprout patterning, OVSC traction forces were first inhibited by setting their magnitude equal to 0 N. Hereafter, this configuration will be referred to as **"OVSC_TF_KO"**.

2.3.5.3 Unloading

To assess the role of mechanical communication at the cellular level, the cortices were fully constrained in all degrees of freedom, thereby unloading the defect. As a control, OVSC traction forces were inhibited in the unloaded configuration and results were compared to the unloaded scenario with active cell forces. Hereafter, these configurations will be referred to as **"Unloading baseline"** and **"Unloading OVSC_TF_KO",** respectively.

2.3.6 Output analysis and visualisation

The model includes elements of stochasticity, such as the initial random cell seeding, the migration rule for OVSCs, and the random probability dictating vessel growth direction. Therefore, 6 realisations for each simulation were performed to allow statistical analysis. *In silico* and *ex vivo* results are reported as mean ± standard deviation.

The predicted sprout patterning from the "Baseline" model at day 7 was compared to the *in vivo* experimental results at the same time point. Histology-like images of the mid-longitudinal section of the healing region were generated from *in silico* results in Matlab (R2020b) to resemble the experimental Endomiucin staining where vessels are coloured red. *Ex vivo* and *in silico* histological images were compared qualitatively and quantitatively. The vessel density was computed through the Fiji plugin "Vessel analysis" [107] within three regions of interest (ROIs) for both *in silico* and *ex vivo* data: defect gap, bone marrow cavity and periosteum. The plugin allowed to obtain the vessel length density ratio, that is the ratio of the skeletonised area to total area within each ROI, thereby disregarding the influence of vessel diameter that is constant in the computer model. The vessel orientation distribution was calculated through the Fiji plugin "Directionality" for both *in silico* and *ex vivo* data, within the same three ROIs. The plugin produces a histogram displaying the percentage of vessel structures in each direction from 0° to 180°, with respect to the x-axis (perpendicular to the bone long axis, Fig. 2.5). The output of the plugin was post-processed by grouping these values into 20°-wide bins. To highlight any preferential orientation

within each ROI, the average percentages of vessels aligned along the bone long axis direction (80°-100° bin), perpendicular to the bone axis (0°-20° and 160°-180°) or all the other directions were compared. Further vascular morphometric features were quantified in Matlab (R2020b) when comparing the baseline and the EC_MR_KO models: the average vessel lengths and the number of self-intersecting vessels that generate closed loops.

OVSCs orientation analysis was performed in Matlab (R2020b) by computing the percentage of cells aligned along each discrete possible direction in the plane.

2.3.7 Statistics

Experimental and simulation results were first tested for normal distribution through the Shapiro-Wilk normality test. The statistical significance of the vessel density between either different ROIs or experimental and simulation results within the same ROI was assessed through a two-tail student t-test implemented in Matlab (R2020b). The statistical significance of the percentage of vessel structures aligned along a preferred direction as compared to all other directions was assessed within each ROI both for *in silico* and *ex vivo* results. Due to the non-normal distribution of certain datasets, the Kruskal-Wallis H test was carried out to compare n>2 groups. In case a significant difference between groups was detected, the post-hoc non-parametric Mann-Whitney U-test was performed in Matlab (R2020b) for pairwise comparisons, complemented by Bonferroni correction. The level of significance was defined as $p \leq 0.05$.

2.4 *In silico* model of angiogenesis and bone regeneration during scaffold-aided bone healing

The third objective of this thesis was to investigate the role of mechanical and geometrical cues on sprouting angiogenesis during scaffold-aided bone defect regeneration.

2.4.1 Simulated *in vivo* experiment

A 4.8-mm bone defect stabilised with an internal PEEK fixation plate was realised in the rat femur and augmented with 3D printed scaffolds fabricated by either Fused Deposition Modelling (FDM) or Melt Elctrowriting (MEW), with n=9 per scaffold type [108]. Scaffolds

were made of polycaprolactone (PCL) with a nano-needle hydroxyapatite (nnHA) coating and were designed to have a comparable total surface area. FDM scaffolds resulted in higher pore size (1.2 mm vs. 0.6 mm) but lower porosity (76.1% vs. 97.6%) and surface area-to-volume ratio (18.04 mm^2/mm^3 vs. 201.31 mm^2/mm^3) as compared to MEW scaffolds. The healing progression was assessed through *in vivo* μCT at 6 and 12 weeks post-surgery. Animals were sacrificed at week 12 and histological analyses were conducted to study tissue formation and vessel ingrowth.

2.4.2 Model-specific computational framework

A previously developed and validated multi-scale computer model for scaffold-aided bone regeneration [109] was adapted to replicate the *in vivo* experiment consisting of a large rat bone defect stabilised with an internal fixator and augmented with FDM and MEW scaffolds, detailed in the previous Section (2.4.1). The computer model was expanded to include a description of the mechano-regulation of angiogenesis and its crosstalk with cartilage and bone formation. FE models at the tissue level, to determine the mechanical environment within the scaffolds, were coupled to ABMs at the cell level, describing biological processes occurring throughout the whole healing process, such as cell proliferation, migration, differentiation, apoptosis and vessel growth. Simulations were performed so as to replicate 12 weeks post-fracture, with one iteration corresponding to one day of bone healing. A detailed description of the two model layers is provided in the following paragraphs.

2.4.3 Finite Element Model (mechanics)

FE models were built to predict the mechanical environment within the FDM and MEW scaffolds.

2.4.3.1 Geometry

FE models of the experimental large bone defect stabilised with a PEEK internal fixation plate and augmented with PCL scaffolds were developed. The intact bone (30 mm long) was modelled as a hollow cylinder of diameter 4.5 mm containing the bone marrow, with a cortical bone thickness of 1 mm based on μCT images. The bone defect was replicated by

opening a 4.8-mm-wide gap in the middle of the intact bone using the Abaqus Boolean cut operation. The callus was defined based on histological data [110] and was modelled by revolving a circular arc with a maximum width of 3.25 mm at its midpoint, overlapping the adjacent bone segments by 1.1 mm on either side. The fixation plate and screws were designed according to technical drawings (Fig. 2.7), with the screw body approximated as a cylinder (Fig. 2.7 A). Scaffolds were modelled in Abaqus (Abaqus 3DEXPERIENCE R2019x) according to the CAD files (Fig. 2.7 B).

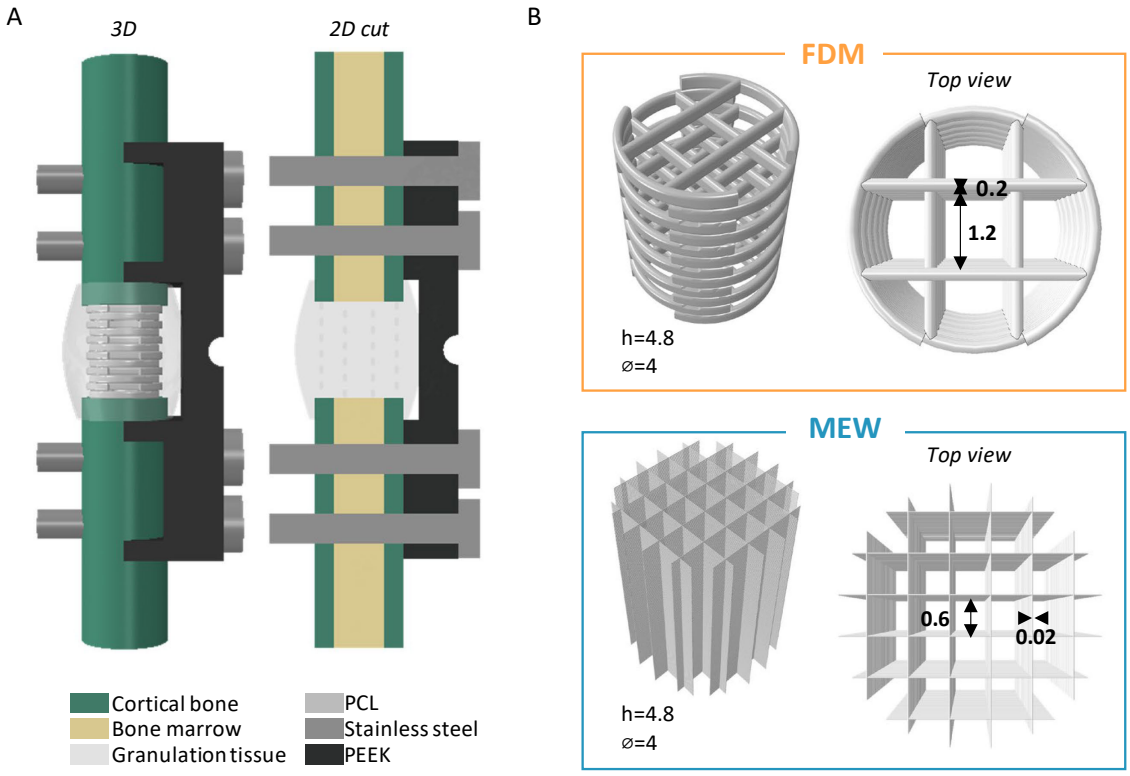

Figure 2.7: In silico geometry of the rat large bone defect augmented with 3D printed scaffolds. ***(A)*** *3D in silico model of the rat large bone defect augmented with a 3D printed scaffold and stabilised with an internal fixation plate (left), alongside the longitudinal section view (right).* ***(B)*** *3D in silico model of the FDM and MEW scaffolds. All measures are in mm.*

2.4.3.2 Mesh

The callus, cortical bone and bone marrow were assumed to behave as poro-elastic materials and were discretised with element types supporting coupled fluid flow and mechanical stress analysis (Abaqus element type C3D10MP). The internal fixation plate, FDM scaffold and screws were meshed using 3D quadratic tetrahedral elements (Abaqus element type C3D10), while MEW struts were meshed using quadratic beam elements (Abaqus element type B32). The callus and scaffold regions were meshed with an average

element size of 0.2 mm, whereas a coarser mesh of 0.5 mm was applied to the rest of the model. A mesh convergence study was conducted to balance computational cost with accuracy (Appendix A.2).

2.4.3.3 Material properties

Poro-elastic material properties were assigned to the intact cortical bone, bone marrow and the granulation tissue initially filling the callus, as well as to the regenerating tissues formed throughout the healing process, including fibrous tissue, cartilage, immature and mature bone (Table 2.5). The internal fixation plate (PEEK), screws (stainless steel) and scaffolds (PCL) were modelled as linear elastic materials (Table 2.5). During the simulation, callus FE material properties were determined through a rule of mixtures based on the proportions of cell types within each element [111], and averaged over the last 10 iterations to reflect delayed ECM deposition [112].

Material	**Young's modulus (MPa)**	**Poisson's ratio**	**Permeability (10^{-14} s m^4/N)**	**Bulk modulus grain (MPa)**	**Bulk modulus fluid (MPa)**
Granulation tissue	0.2[a]	0.167[a]	1[a]	2300[a]	2300[a]
Fibrous tissue	2[a]	0.167[a]	1[a]	2300[a]	2300[a]
Cartilage	10[a]	0.3[a]	0.5[a]	3700[a]	2300[a]
Immature bone	1000[a]	0.3[a]	10[a]	13940[a]	2300[a]
Mature bone	5000[a]	0.3[a]	37[a]	13940[a]	2300[a]
Cortical bone	5000[a]	0.3[a]	0.001[a]	13920[a]	2300[a]
Bone marrow	2[a]	0.167[a]	1[a]	2300[a]	2300[a]
PEEK (fixation plate)	3800	0.3	-	-	-
Stainless steel (screws)	210000	0.3	-	-	-
PCL (3D printed scaffolds)	350[b]	0.33	-	-	-

[a][93], [b] [113-119]

Table 2.5: Material properties.

2.4.3.4 Loading and boundary conditions

A combination of compression and bending load, corresponding to the peak loads experienced during normal walking conditions in rats, was applied on the intact bone proximal end: a 6 body weight (BW) proximal-distal compression load and an anteroposterior and a medial-lateral 10.7 BW mm moment at the femur mid-point [120].

Considering the average rat weight of 0.425 kg, this resulted in a proximal-distal compression load of 25 N and two tangential forces of 3 N applied to the proximal bone surface in the anteroposterior and medial-lateral directions. The distal bone surface was fully constrained. A pore pressure boundary condition was set to zero on the external surface of the callus domain.

The callus and FDM scaffold meshes were merged to avoid costly constraint definitions. For the MEW scaffold, merging was not feasible due to differing element types and associated degrees of freedom, therefore, beam elements were embedded within the 3D callus mesh by using the Abaqus *EMBEDDED ELEMENT constraint which kinematically linked the beam nodes to the surrounding solid elements.

2.4.4 Agent-based model (biology)

ABMs were developed to simulate the biological processes taking place throughout bone healing. A 3D lattice grid with 20 μm spacing was defined over the entire healing region.

2.4.4.1 Cell phenotypes and seeding

The ABM included the following agent types (cell phenotypes): MSCs, fibroblasts, chondrocytes, immature osteoblasts, mature osteoblasts and ECs. Initially, only MSCs and ECs were assumed to be present at the fracture site. To simulate the MSCs and vessel invasion from the bone marrow cavity and periosteum (the region surrounding the intact bone extremities), 30% [100] and 2% [91] of available positions within the bone marrow close to the defect and the periosteum were filled with MSCs and ECs, respectively. All cells were assumed to have a diameter of 20μm [101].

2.4.4.2 Cell activity

OVSCs activities

MSCs and fibroblasts were the only cells assumed to migrate. To replicate the cell surface-guided migration observed experimentally in scaffolds [121, 122], cell migration was conditioned by the presence of an adjacent surface, i.e. either previously deposited tissue (bone, cartilage, fibrous tissue) or scaffold. Essentially, for a cell to move to a new position, that position not only had to be free but was also required to have a neighbouring

lattice position occupied by deposited tissue or scaffold. MSCs were implemented to differentiate with an initial rate of 0.3 per day. To replicate the surface-guided ECM deposition observed experimentally [122, 123], i.e. ECM deposition needs a pre-existing substrate to adhere to, MSCs were allowed to differentiate into a new cell phenotype only when at least one of the adjacent neighbour lattice positions was an existing surface (previously deposited tissue or scaffold). Cells were modelled to proliferate and undergo apoptosis, and those processes were influenced by the local mechanical stimulus. This meant counting the number of cells of each phenotype in every FE and computing the number of proliferating cells when the local mechanical stimulus favoured that phenotype, or the number of apoptotic cells when it did not. All cell activity rates are derived from the literature and are reported in Table 2.6. To simulate the reduced biological activity observed in large bone defects [29], particularly impacting cell proliferation and differentiation [122], a 15-day latency period was introduced after which cell proliferation and differentiation rates were decreased (Table 2.6).

Cell type	**Proliferation rate (day^{-1})**		**Apoptosis rate (day^{-1})**	**Differentiation rate (day^{-1})**		**Migration speed ($\mu m.h^{-1}$)**	**Vessel growth rate ($\mu m.h^{-1}$)**	
	<15 days	≥15 days		<15 days	≥15 days		<15 days	≥15 days
MSC	0.6[a]	0.3[b]	0.05[a]	0.3 [a]	0.15[b]	30[c]	-	-
Fibroblast	0.55[a]	0.28[b]	0.05[a]	-	-	30[c]	-	-
Chondro-cyte	0.2[a]	0.1[b]	0.1[a]	-	-	-	-	-
Osteoblast	0.3[a]	0.15[b]	0.16[a]	-	-	-	-	-
EC	-	-	-	-	-	-	15[d]	0.6*

[a][101], [b][109, 122], [c][102], [d][103], *Estimated to obtain a final vessel density comparable to the experiment.

Table 2.6: Cell activity parameters.

Angiogenesis

The ABM was complemented with a description of the mechanobiological regulation of angiogenesis and its interaction with the bone regeneration process. The algorithm is similar to the one presented for the early bone regeneration model (Section 2.3.4.2), extended to account for the out-of-plane dimensions. During bone healing, hypertrophic chondrocytes (i.e. mature chondrocytes aged at least 6 days) secrete VEGF [124], known to induce directed ECs migration [125, 126]. To incorporate this aspect into the model, the direction of vessel growth at each iteration was determined based on the following

probabilistic rule: (1) following the strain-based rule (20%) described in Section 2.3.4.2, (2) directed towards high concentrations of hypertrophic chondrocytes (40%), (3) towards a random direction (40%). The vessel rate of growth was assumed to be dependent on local strain levels [10, 15-18], reaching the maximum value, reported in Table 2.6, for strains between 5% and 10% and linearly decreasing until 0 for strains above 30%, known to hinder vessel growth [89]. The maximum vessel growth rate was reduced after 15 days, consistent with experimental findings reporting a faster vessel infiltration during the early healing phase [83]. Oxygen influences MSC differentiation, with hypoxic conditions favouring cartilage formation and higher oxygen levels promoting bone formation. Given the limited diffusion range of oxygen from blood vessels (approximately 100–200 μm) [127], the extent and morphology of the vascular network can highly impact bone regeneration. This aspect was simulated by allowing MSCs differentiation towards chondrocytes in bone-favoured regions that were more than 100 μm away from the nearest blood vessel.

2.4.5 *In silico* experiments

To better isolate the contribution of FDM and MEW architectural features on vessel growth, the growth rate of vessels was made independent of mechanical signals: the growth rate was set to its maximum value, corresponding to strain levels between 5% and 10%, and was kept constant regardless of the mechanical environment.

To assess the contribution of each vascular source independently, simulations were performed where vessel sprouting was allowed exclusively either from the bone marrow or from the periosteum.

Finally, although vessels were assumed to have a fixed diameter of 20 μm, experimental observations indicated the presence of larger vessels within the FDM scaffold [108]. Therefore, additional simulations were carried out assuming a vessel diameter of 40 μm, to assess whether larger vessels would be more sensitive to pore size differences between the two scaffold architectures.

2.4.6 Output analysis and visualisation

Five simulations were conducted per scaffold type, and the median simulation based on the regenerated bone volume was selected to generate all 2D and 3D visual outputs. When

quantitatively comparing simulation outputs to the experimental data, the outcomes are presented as mean ± standard deviation.

Simulation results for both MEW and FDM scaffolds were qualitatively compared to the experimental μCT and histological images. To generate μCT-like images from *in silico* results, the predicted 3D lattice was converted into a binary format (1=bone, 0=not-bone) and visualised using the ImageJ module VolumeViewer plugin [65]. μCT-like images of the simulated vascular network were generated similarly, by assigning a value of 1 to lattice points occupied by vessels. To obtain histology-like 2D images, lattice points in the mid-longitudinal plane were coloured to reflect the predicted tissue, using palettes consistent with Goldner's Trichome or Safranin O staining: dark green for bone, pink for fibrous tissue and red for cartilage. Background tissue colours matched those in the experimental images.

Quantitative comparisons between model predictions and experimental results were made for the regenerated bone volume and vessel density. Bone volume within the defect region was calculated by counting the number of lattice points occupied by bone and multiplying by the point volume ($8x10^{-6}$ mm^3). Vascular density was assessed by post-processing simulation outputs to mimic the experimental procedures: for each simulation (n=5), three sections spaced 0.5 mm apart were selected and a central region of interest (ROI) measuring 2x2.5 mm^2 was analysed. Vessels containing more than 3 ECs were counted and the number of vessels per unit area was computed.

To better understand the role of the mechanical environment and scaffold architectural features on bone regeneration and vessel growth, additional visual outputs and measurements were made. Absolute maximal principal strain distributions post-surgery were extracted in the mid-longitudinal plane from the FE simulation and the volumetric percentages falling within strain ranges known to influence angiogenesis were computed for both MEW and FDM. In addition, the number of vessels exposed to inhibitory strain levels (strains >30%) was tracked over time within both scaffolds. To understand the influence of the scaffold architecture on vessel growth, after decoupling their rate of growth from the mechanics, the number of vessels blocked by scaffold walls, and thus prevented from growing further, was tracked over time for both scaffolds. The distribution of the mechanical stimulus in the mid-longitudinal plane was visualised both post-surgery and after 12 weeks, for both scaffolds. Each lattice point was coloured based on the predicted mechanically favoured tissue type, according to Prendergast mechano-regulation theory [93]. Osteoblast proliferation and differentiation were tracked over time within the healing

region. Additionally, the percentage of MSCs unable to differentiate into bone due to a lack of neighbouring surfaces was monitored within both scaffolds over time.

2.4.7 Statistics

Statistical tests were performed on the *in silico* results and used to compare them with experimental data, using R (R 4.4.3) in the Posit Cloud environment (Posit Public Cloud, https://posit.cloud/). All datasets were checked for normality using the Shapiro-Wilk test and equality of variance through Levene's test. A two-way ANOVA was performed for bone volume quantifications with Tukey post-hoc test for pairwise comparisons. A one-way ANOVA was used for vessel density quantifications with Bonferroni post-hoc test. Unpaired Welch's t-tests were used to compare *in silico* vs. *in vivo* results, due to unequal variances between the two groups, for both bone volume and vessel density. The level of significance was defined as $p \leq 0.05$.

3

In silico investigation of stromal cell-driven sprouting angiogenesis within an anisotropic scaffold

In this Chapter, results from the computer model of stromal cell-driven sprouting angiogenesis within an anisotropic scaffold will be presented and discussed.

3.1 *In silico* prediction of cell and vessel organisation within an anisotropic scaffold

Computer model predictions of fibroblast and vessel organisation within the scaffold channel-like pore after 7 and 14 days agreed with experimental observations (Figure 3.1 A-B). Both *in silico* and *in vitro*, fibroblasts and vessels appeared to align mainly along the pore long-axis direction in each simulated scenario (Fig. 3.1 A-B). The quantification of vessel and fibroblast alignment showed that about 80% of fibroblasts and about 60% of vessel structures were aligned along the pore long-axis direction in each simulated scenario (Fig. 3.1 C). This suggested that *durotaxis*, i.e. the cell preference for stiffer environments, can explain the orientation of vessels and cells observed experimentally within an aligned geometry.

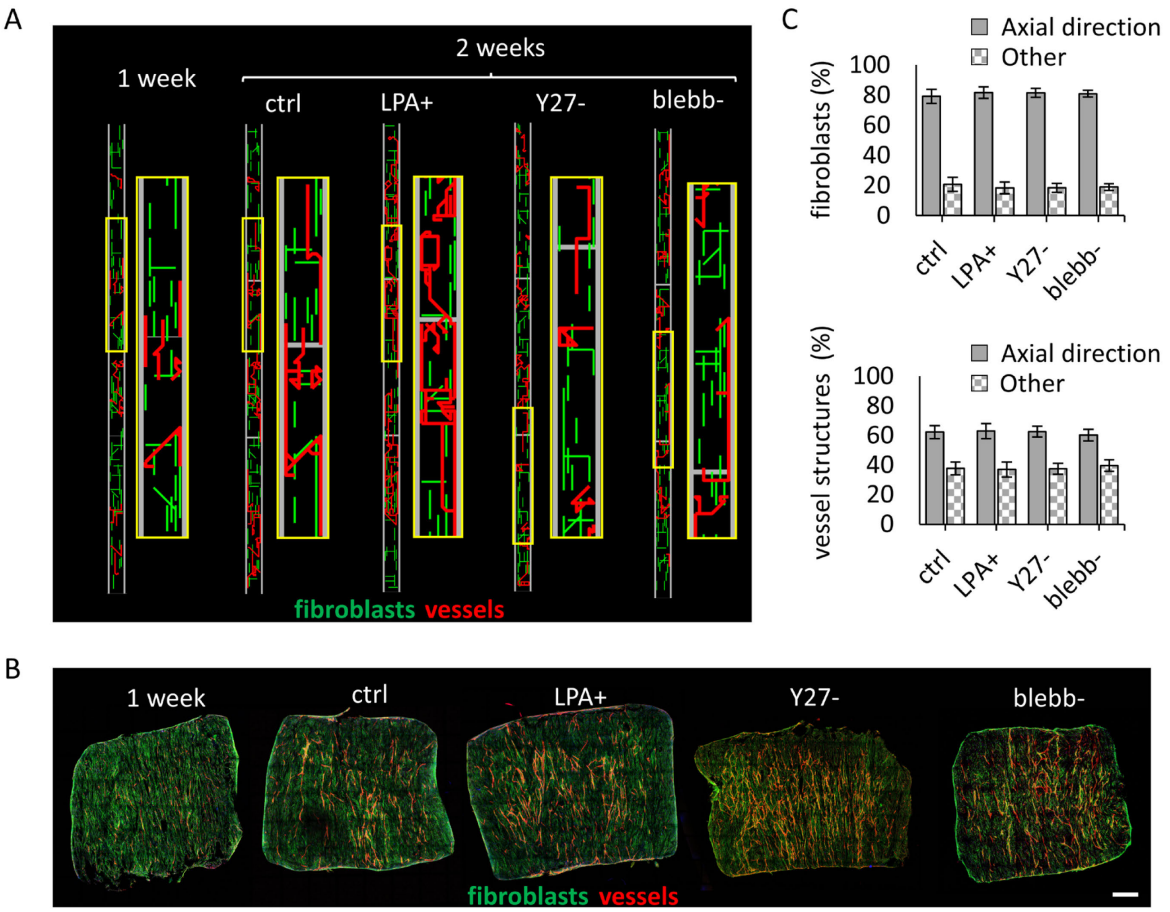

Figure 3.1: Cell and vessel organisation within an anisotropic scaffold. ***(A)*** *Predicted vessel and fibroblast organisation after 1 week (control) or 2 weeks under different chemical modulators. A closer view of the channel-like pore is enclosed in the yellow boxes.* ***(B)*** *Confocal images of co-culture samples after 1 week (control) or 2 weeks under different chemical modulators. Vessels were stained in red and fibroblasts in green. Chemical modulators were applied after 1 week. Scale bar 500 μm.* ***(C)*** *Percentage of fibroblasts (top) and vessel structures (bottom) aligned along the axial direction (pore long-axis) vs. any other direction for each scenario. N=20.*

3.2 Local strain levels modulate vessel elongation

The mechanical strains arising within the pore as a consequence of cell contractile activity were mainly compressive strains (Fig. 3.2). Strain levels predicted within the pore were related to the experimentally measured effect of chemical modulators on cell contractility (Fig. 2.3 B). Higher strains were predicted upon LPA+ as a consequence of the increased cell force magnitude, while lower strains were induced upon Y27- and blebb-, due to their inhibitory effect on cell contractility.

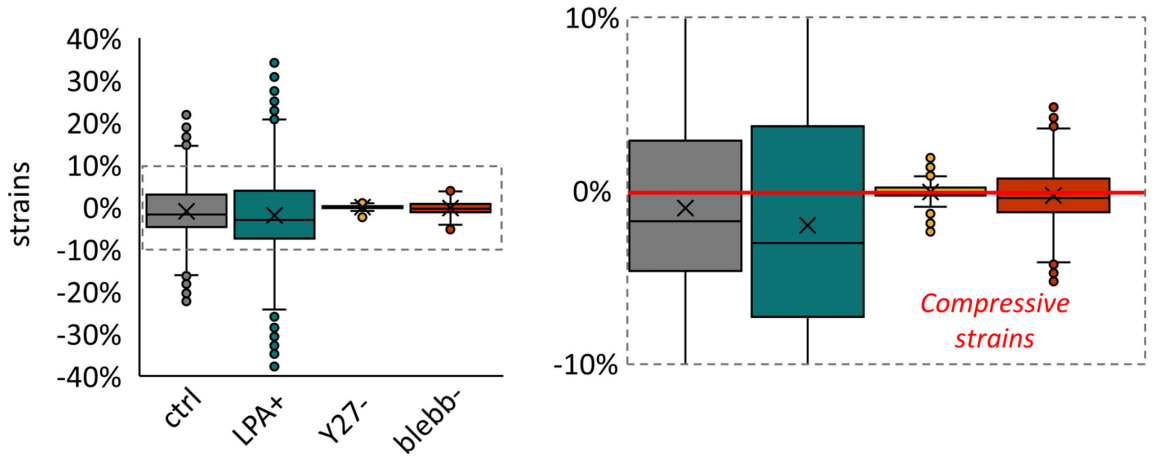

Figure 3.2: Modulation of cell forces influences strains within the scaffold. *Absolute maximum principal strain distribution within the scaffold pore for each scenario.*

Relevant predicted vessel network parameters were quantified (Fig. 3.3 A-C) and compared to the *in vitro* (Fig. 3.3 D-F) results. An increased number of branches per vessel was predicted between week 1 and week 2 in the control group, similar to *in vitro* observations. *In vitro* results showed a marked rise in the number of branches per vessel under Y27- treatment that was not predicted by the computer model (Fig. 3.3 A, D). The computer model predicted longer branches in the presence of LPA+ compared to the control, whereas both blebb- and Y27- were associated with shorter vessel segments (Fig. 3.3 B, E). This trend reflects experimental results and can be attributed to the levels of mechanical strains, higher under LPA+ and lower under blebb- and Y27-. The computer model predicted an increased total network length from week 1 to week 2 in the control group, which aligns with experimental findings. After 2 weeks, LPA+ was predicted to induce a mildly longer vascular network, while blebb- and Y27- resulted in shorter networks (Fig. 3.3 C, F). While this behaviour reflects the mechanical strain levels induced by each chemical treatment within the pore, it is in contrast with experimental observations showing a significantly greater total vessel length upon Y27- treatment. So far, the computer model failed to capture the increased number of branches per vessel and total network length observed experimentally under Y27- treatment.

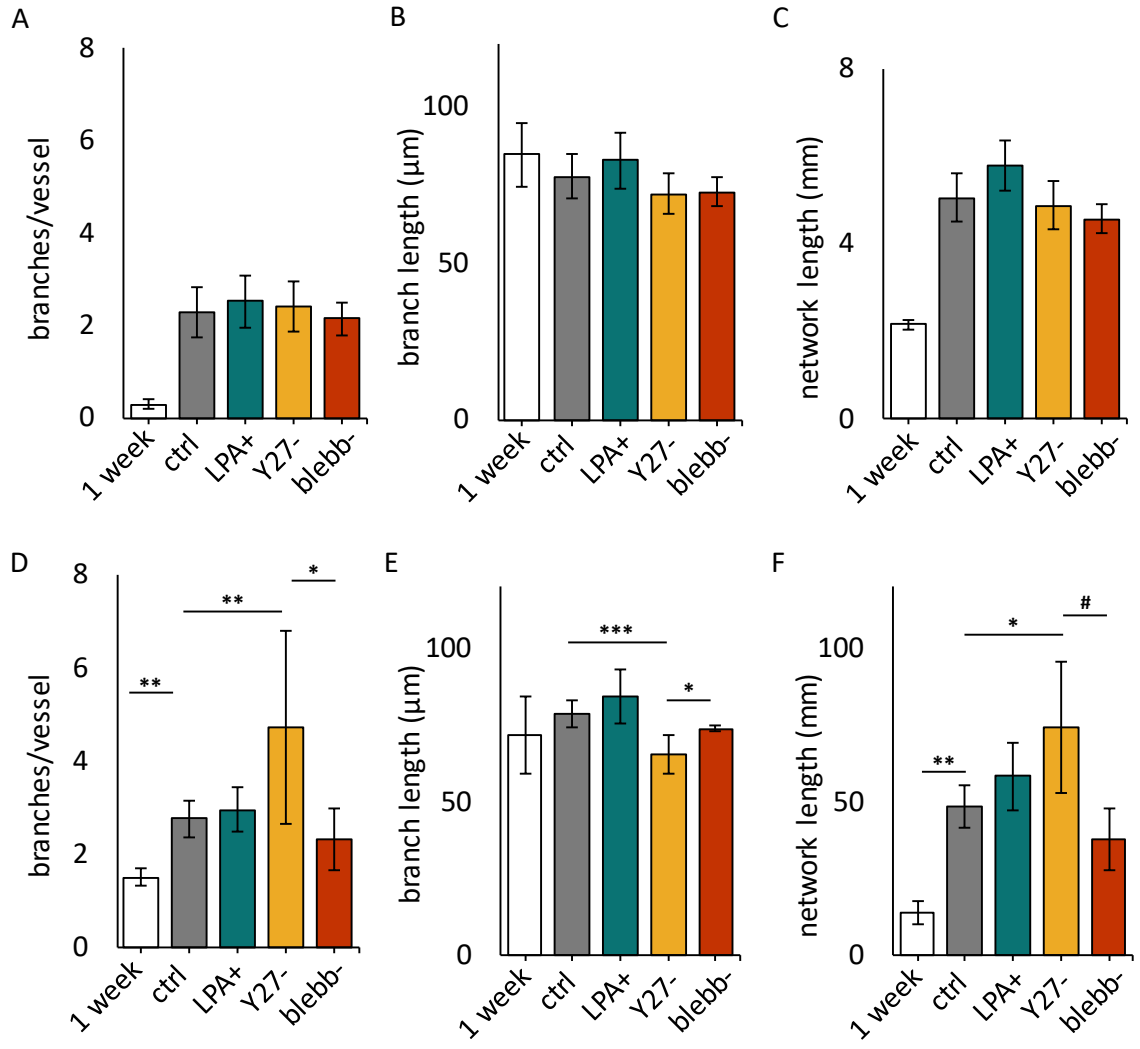

Figure 3.3: Predicted vascular network parameters and comparison with experimental data. (A-C) *Quantification of relevant vessel network parameters from in silico results: the number of branches per vessel, the average length of an individual branch (in µm), total network length as the sum of all vessels (in mm). N= 20.* ***(D-F)*** *Quantification of relevant vessel network parameters from in vitro results: the number of branches per vessel, the average length of an individual branch (in µm), total network length as the sum of all vessels (in mm). N ≥ 3 of at least 2 independent experiments. Significance levels are indicated as follows: # p<0.1, * p<0.05, ** p<0.01, *** p<0.001.*

3.3 Chemical modulators induce changes in cell morphology and force distribution

In addition to altering cell contractility, the applied chemical modulators appeared to impact cell morphology, in particular under Y27- treatment. Reconstructed cell contours based on 2D Traction Force Microscopy (TFM) images showed that Y27- treated cells exhibited a less polarised shape, while all other cases appeared to retain the typical polarised morphology and associated stress patterns (Fig. 2.3 B). To assess whether

fibroblast morphological differences resulted in distinct traction force patterns relevant to the computational model, single-cell simulations were performed using a 2D FE model replicating the TFM setup. It was examined whether non-axial force components were negligible, thereby justifying the dipole representation, or if a more isotropic representation, including other force components, was required upon chemical treatment. The FE model consisted of a 1mm x 1mm gel, matching the elastic modulus of the experimental substrate (E=12.3 kPa), discretised with 4-nodes elements (CPE4R) with a node spacing of 0.01 mm and the four corners constrained in all degrees of freedom (Fig. 3.4 A). One cell was seeded in the middle of the gel and concentrated loads mimicking cell traction forces were applied to surrounding nodes (Fig. 3.4 A). In the computer model, eight discrete positions were available around the cell core for force application (Fig. 3.4 B). To obtain representative force values along each discrete direction, experimentally measured traction forces were binned in three different groups accounting for the axial (0°-22.5°), diagonal (22.5°-67.5°) and orthogonal (67.5°-90°) directions, for each cell (Fig. 3.4 B). For every condition (Ctrl, LPA+, blebb-, Y27-), the median force within each angle group across all cells was computed. These values were then scaled to represent individual force vectors around the cell core: halved for the two axial and orthogonal force vectors and quartered for the four diagonal vectors (Fig. 3.4 B).

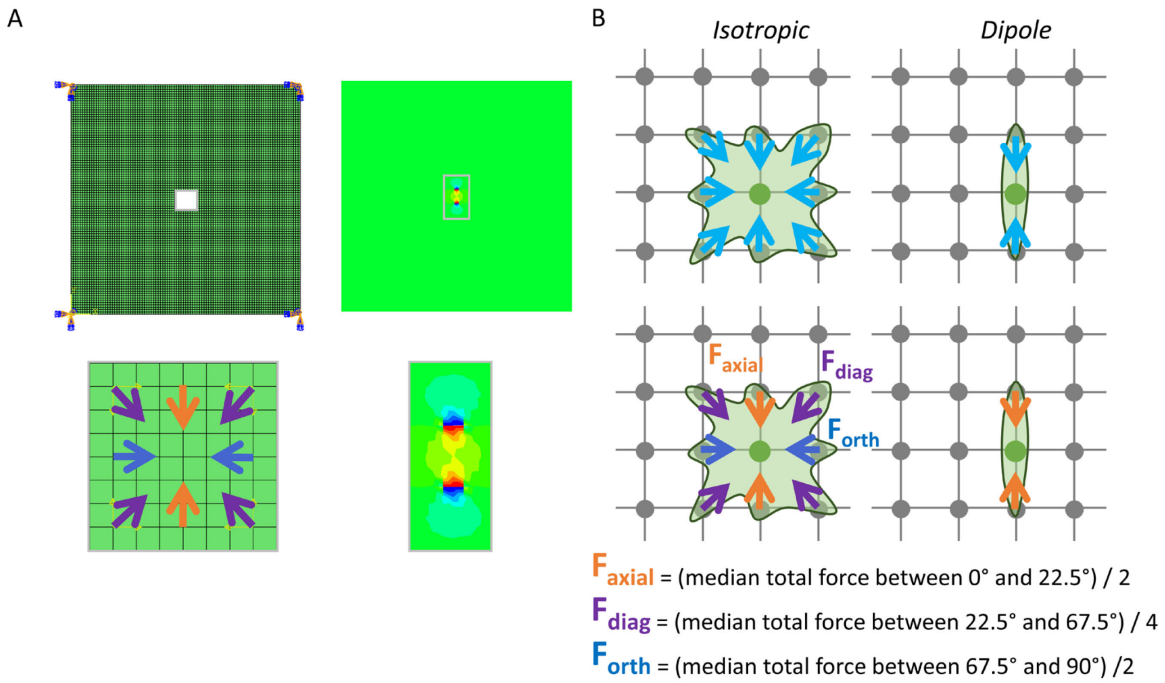

Figure 3.4: Integrating experimentally measured traction force patterns into the computer model. ***(A)*** *FE model replicating TFM experiments on single cells (left) and representative predicted strain distribution from the cell contractile activity (right).* ***(B)*** *Representation of how traction forces are distributed around the cell core in silico when assuming an isotropic (top-left) or dipole (top-right) configuration and representation of how traction force values are computed when assuming an isotropic (bottom-left) or dipole (bottom-right) configuration.*

Strain fields resulting from each simulated force configuration (dipole vs. isotropic) were generated for the control, LPA+, blebb- and Y27-. Qualitatively, dipole and isotropic configurations produced similar strain distributions in the control, LPA+ and blebb- cases. In contrast, isotropic Y27- led to a different strain pattern compared to the dipole Y27- configuration. This was confirmed quantitatively by computing the Relative Error (RE) between the strain fields of the two force configurations, defined as the ratio of the L^2 norm of their difference to the L^2 norm of the isotropic force configuration's field. Control, LPA+ and blebb- exhibited low RE values (≤ 6%), confirming that the non-axial force components contributed very little to the overall strain distribution, while Y27- reported a RE value >30% (Table 3.1).

	Absolute maximum principal strains			F_{axial} [nN]	F_{orth} [nN]	F_{diag} [nN]	RE
	Isotropic	**Dipole**	**Legend**				
Ctrl	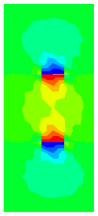	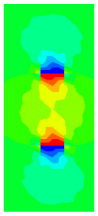	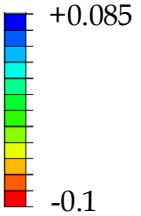	281	26	5	4.50%
LPA+	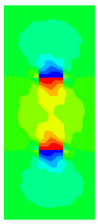	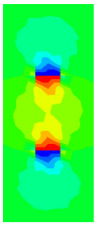	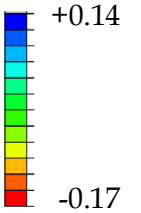	459	7	37	4.04%
blebb-	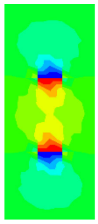	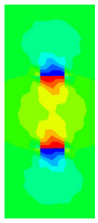	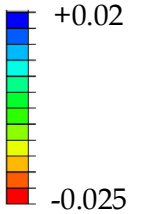	69	1	8	5.75%
Y27-	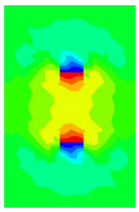	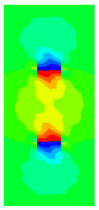	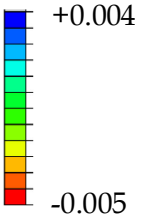	13	3	7	31.41%

Table 3.1: Comparison of strain fields generated by isotropic vs. dipole force patterns. *For each simulated scenario, from the left, contour plots of the strain distribution of the two tested configurations (isotropic vs dipole), the magnitude of each force component, and the relative error (RE).*

3.4 Cell force directionality regulates vessel sprouting

The computer model was expanded to include the cell-specific morphology and force distribution: while control, LPA+ and blebb- -treated cells remained dipoles, an isotropic force distribution (including all force components) was assigned to Y27-. After two weeks,

a denser and more intricate vascular network was predicted within the pore under Y27- isotropic compared to Y27- dipole (Fig. 3.5 A). The isotropic cell morphology resulted in a less aligned orientation of fibroblasts, while vessels showed a similar distribution as for all other conditions (Fig. 3.5 B). In agreement with *in vitro* findings, simulations predicted a significant increase in the number of branches per vessel upon isotropic Y27-, as more sprouting was driven by cell forces oriented orthogonally to the vessel axis (Fig. 3.5 C). The average branch length was significantly reduced upon isotropic Y27-, which can be attributed to not only the lower strain levels induced within the pore but also to the increased branching frequency, resulting in a higher number of newly formed and shorter vessels (Fig. 3.5 D). Nevertheless, the total vascular network length was higher under isotropic Y27- as a direct consequence of the increased number of branches or sprouts (Fig. 3.5 E), consistent with experimental data.

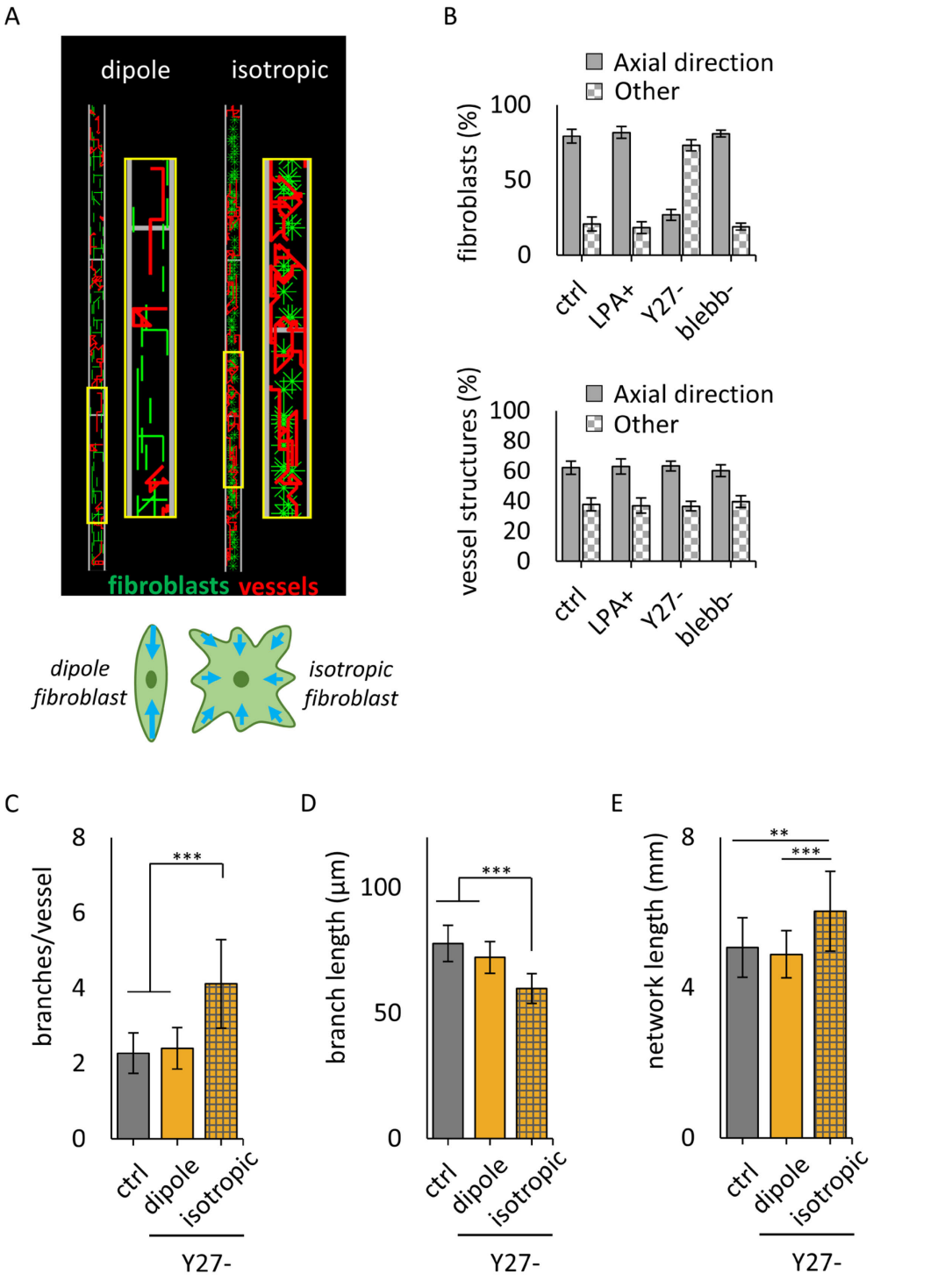

Figure 3.5: Influence of dipole vs. isotropic force configuration on cell organisation and angiogenesis. ***(A)*** *Predicted vessel and fibroblast organisation after 2 weeks for Y27- dipole vs. isotropic force patterns. A closer view of the pore is enclosed in the yellow boxes.* ***(B)*** *Percentage of fibroblasts (top) and vessel structures (bottom) aligned along the pore long-axis vs. any other direction for each scenario. N=20.* ***(C-E)*** *Quantification of relevant vessel network parameters from in silico results for control, dipole Y27- and isotropic Y27-: the number of branches per vessel, the average length of an individual branch (in µm), total network length as the sum of all vessels (in mm). N=20. Significance levels are indicated as follows: ** p<0.01, *** p<0.001.*

3.5 Discussion

Understanding how endothelial cells integrate mechanical signals from their microenvironment is fundamental to advancing bone regeneration strategies. In scaffolds with highly aligned pores, coculture experiments with ECs and fibroblasts showed preferential alignment of both vessels and cells along the pore principal axis, suggesting that scaffold anisotropy guides cellular and vascular organisation. Thereafter, fibroblast traction forces were chemically modulated: contractility was enhanced using LPA+ and reduced with blebb- or Y27-. These perturbations altered vessel morphology and patterning. Specifically, increased vascularity was observed under LPA+ treatment compared to control and blebb-, as a consequence of the higher fibroblast contractility under this condition. Surprisingly, however, Y27- treatment produced an even greater vascularity than LPA+, suggesting that fibroblast-ECs mechanical interactions are not governed solely by force magnitude. To address this inconsistency and better understand how scaffold anisotropy and cell-generated forces impact vessel patterning, a computer model of the mechanoregulation of sprouting angiogenesis in co-culture with fibroblasts within an anisotropic scaffold was developed, resembling the experimental setup. Fibroblasts were initially modelled as spindle-shaped cells following the existing literature and previous computational models [78, 80, 90], while traction force magnitudes under the different chemical modulators were retrieved from experimental TFM measurements. The *in silico* model successfully recapitulated the sprouting process within the scaffold over 14 days and captured the experimentally observed preferential alignment of vessels and cells along the pore long-axis, driven by *durotaxis*. Although the predicted vascular network under chemical modulation of cell forces reproduced several morphological features observed experimentally, the initial version of the model failed to capture the increased sprouting observed under Y27- treatment. Therefore, an extended version of the model was developed that incorporated not only the differences in cell force magnitude induced by chemical modulators, as measured by TFM, but also the associated changes in cell morphology and the spatial distribution of forces around the cell body. The refined model successfully matched experimental results, suggesting that while traction force magnitude and the induced levels of mechanical strains account for endothelial cell proliferation and vessel elongation, the directionality of these forces, determined by cell morphology, is a critical factor in controlling vessel sprouting and branching.

A few computational models of sprouting angiogenesis have investigated ECs-matrix interplay mediated by endothelial cell traction forces. Santos-Oliveira and colleagues [59] introduced a phase-field continuous model in which tip EC traction forces transmit tension to stalk cells, triggering strain-induced proliferation; the newly added cell relieves the tension and the cycle repeats, driving continuous sprout extension. Stephanou et al. [60] developed a hybrid continuous–discrete framework where discrete ECs exert traction forces on a continuum ECM. They identified a traction force window that allows network formation and showed that matrix rigidity can further influence ECs migration and angiogenesis. Van Oers and colleagues [61] coupled a Cellular Potts model of ECs to an FE model for the substrate and demonstrated a simple mechanical feedback that can explain sprout formation: ECs pull on the matrix and then follow the stiffer, strained tracks they create (*durotaxis*). While these studies proposed key mechanisms of ECs-matrix mechanical interplay during *in vitro* angiogenesis, they lack quantitative validation against dedicated experiments. Edgars et al. [62] developed a hybrid model coupled to dedicated *in vitro* experiments, in which discrete sprouts interact with a continuum, fibrous ECM. They showed that sprout-generated forces deform the ECM and reorient collagen fibres, which in turn guide vessel growth, thereby explaining the observed alignment under different geometric constraints. Although this model introduced the effect of geometrical cues, outer-vascular stromal cells were not modelled. This work presents, for the first time, a computer model of the mechanical crosstalk between OVSCs and endothelial cells during sprouting angiogenesis, within a highly aligned geometry, and validated against dedicated *in vitro* experiments.

Durotaxis-guided cell and vessel alignment

The computer model predicted a preferential alignment of vessels and fibroblasts along the pore long axis direction after 2 weeks, consistent with cell and vessel organisation observed experimentally within the scaffold (qualitative comparison due to lack of experimental data), supporting *durotaxis* as a key mechanism underlying the alignment. Indeed, cell migration and reorientation were modelled through a rule based on *durotaxis*, following the available literature [9, 23], where both cells and vessels measured the local deformation induced by their contractility and preferentially migrated toward stiffer regions. Noteworthy, these results were independent of the specific chemical modulators.

Cell traction force magnitude and spatial organisation

Specific morphological vessel features were quantified for both *in silico* and *in vitro* outputs and compared across the different scenarios. The computer model successfully captured the increased total network length and average branch length under LPA+ treatment, in agreement with experimental observations. This can be explained by the enhanced fibroblast contractility induced by LPA+, which led to strain levels within the scaffold pores promoting vessel growth. These findings are consistent with previous studies demonstrating that mechanical strains affect endothelial cell proliferation and thus vessel elongation, specifically, vessel growth is particularly favoured for strains between 5% and 10% [15-18, 89]. In contrast, the model failed to reproduce the increased branching observed experimentally under Y27- treatment, indicating that the levels of mechanical strains alone cannot explain experimental results and other mechanisms should be explored and incorporated into the computational framework.

Interestingly, Y27- treatment was found to influence not only the magnitude of cell-generated forces but also cell morphology and thus the spatial distribution of traction forces around the cell body. In particular, stresses induced by the cell contractile activity resulted more isotropically distributed around the cell body, departing from the classic spindle-shaped representation. Based on these experimental observations, it was hypothesised that changes in cell morphology and the associated force spatial distribution contribute to vessel growth and sprouting, along with matrix strain levels. In particular, it was proposed that isotropic fibroblasts exerting orthogonal forces on highly aligned vessels may promote branching events. Upon confirming *in silico* that non-axial force components upon Y27-treatment significantly affect the strain field generated by the cell, a more isotropic traction force distribution was assigned around the Y27- cell body, based on TFM data. After two weeks, this upgraded model predicted a marked increase in vessel branching in the presence of isotropic Y27- cells. Moreover, the overall vascular network was longer in the presence of isotropic Y27- cells as compared to all other cases, as a consequence of the increased branch formation, matching experimental findings. These results demonstrate that, beyond force magnitude, the spatial distribution of traction forces, determined by cell morphology, plays a key role in modulating strain orientation and patterning around sprouting vessels, ultimately influencing branching behaviour and vascular network architecture.

Limitations and future work

A few limitations of the developed computational framework should be mentioned. Due to the complexity and high level of detail of the collagenous scaffold architecture, only the mid-section of the scaffold was modelled. Despite this simplified representation, the modelled scaffold resulted mechanically equivalent to the one used in the experiment, specifically, the axial stiffness was comparable to the experimentally measured one. Although this approach served the scope of the study and provided insights into the mechanical interaction between fibroblasts and vessels, details on the 3D aspects of these interactions cannot be captured with the current framework. Future work should aim to incorporate the complete 3D geometry of the scaffold by using strategies relying on beam and shell elements, as previously proposed by Herrera et al. [85].

Although the refined computer model captured the experimentally observed increase in total network length under Y27- treatment, the predicted length value is lower than the one measured experimentally. This discrepancy can be attributed to the fact that the computer model evaluates the network length within a single pore, whereas the experimental quantification was performed across the entire scaffold cross-section. Thus, the comparison can only be considered qualitative.

The computer model did not include a description of ECM fibre deposition and remodelling. However, a previously published *in vitro* study with fibroblasts cultured in the same macroporous collagen scaffold showed the formation of highly aligned ECM fibres along the pore main axis over 14 days [84]. ECM fibre organisation has already been associated with cell orientation [128, 129] and is thought to provide contact guidance cues for vessel growth [130, 131]. Future extensions of the model should incorporate fibroblast-driven fibre deposition and remodelling, and enrich the angiogenesis algorithm with a rule for contact guidance. The presence of highly aligned collagen fibres is expected to reinforce, and not alter, the predicted vessel alignment. An open question is whether the deviations in fibroblast morphology and organisation predicted upon Y27- treatment could result in a more disordered matrix network, thereby contributing to the observed increase in sprouting.

Lastly, both *in vitro* and *in silico* models were designed as simplified systems to isolate the effects of cell-cell mechanical interactions on angiogenesis. *In vivo*, cells and vessels experience more complex and dynamic environments, including biochemical signals, multidirectional ECM organisation, spatially varying stiffness, blood flow and external

mechanical loads that affect cell morphology and vascular organisation. Moreover, the *in vitro* setup described here reduced morphological variability by promoting cell and vessel alignment; however, clear differences in sprouting potential still emerged, suggesting that findings are robust. Further studies are needed to evaluate how cell-generated traction forces impact vessel patterning *in vivo*. The following chapters will investigate angiogenesis in more physiologically relevant conditions.

4

In silico investigation of the mechano-regulation of stromal cell and vessel organisation during early bone healing

In this Chapter, results from the computer model of stromal cell and vessel organisation during early bone healing will be presented and discussed.

4.1 Strain magnitude and principal strain directions can explain vessel patterning during early bone healing

Mechanical strains developing within the healing region under both rigid and semirigid fixators were mainly compressive strains. Higher compressive strains were predicted under semirigid fixation compared to the rigid fixator (Fig. 4.1 A). The highest average compressive strains were found between the cortical fragments on the free (non-fixator) side (rigid fixator: -13.9±1.5%; semirigid fixator: -57.1±6.2%) compared to the fixator side (rigid fixator: -11.7±1.2%; semirigid fixator: -46±4.7%). Within the endosteal gap (fracture space inside the cortical bone), strains were predicted to be -11.1±0.9% and -44.8±3.9% in the case of rigid and semirigid fixators, respectively. The periosteal region (external to the cortices) exhibited the lowest compressive strains, still higher on the free side (rigid fixator: -7.9±2.2%, semirigid fixator: -32.5±9%) compared to the fixator side (rigid fixator: -6.2±1.7%, semirigid fixator: -23.9±6.7%). The absolute maximum principal strains were

predominantly aligned with the bone's longitudinal axis, consistent with the direction of the displacement boundary conditions applied at the cortices (Fig. 4.1 B).

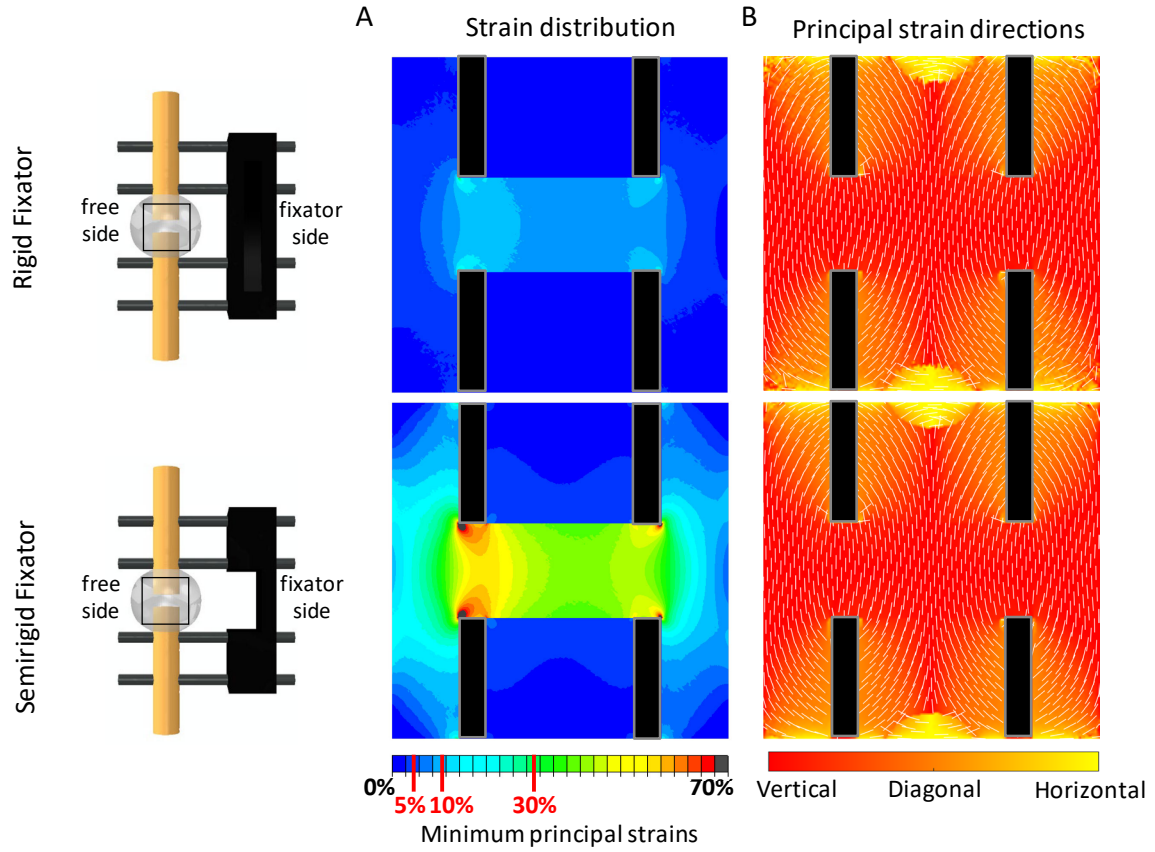

Figure 4.1: Predicted principal strain distribution and orientations. ***(A)*** *Predicted minimum principal strain distribution and* ***(B)*** *principal strain directions within the longitudinal mid-section of the healing region of a mouse defect stabilised with a rigid (top) and semirigid (bottom) fixator. Black rectangles are overlaid on the cortices.*

The predicted revascularisation of the healing region 7 days post-surgery reflected experimental results, both qualitative and in terms of vessel density in different ROIs. Under rigid fixation, vessels were predicted to invade the whole healing region, while under semirigid fixation, the endosteal region was not vascularised, similar to *ex vivo* results (Fig. 4.2 A-B). This is reflected by the significantly reduced vessel density within the gap (ROI1) obtained both *in silico* and *ex vivo* under semirigid fixation (Fig. 4.2 C), which can be linked to the high strain values at the endosteal gap, above 30% (Fig. 4.1 A).

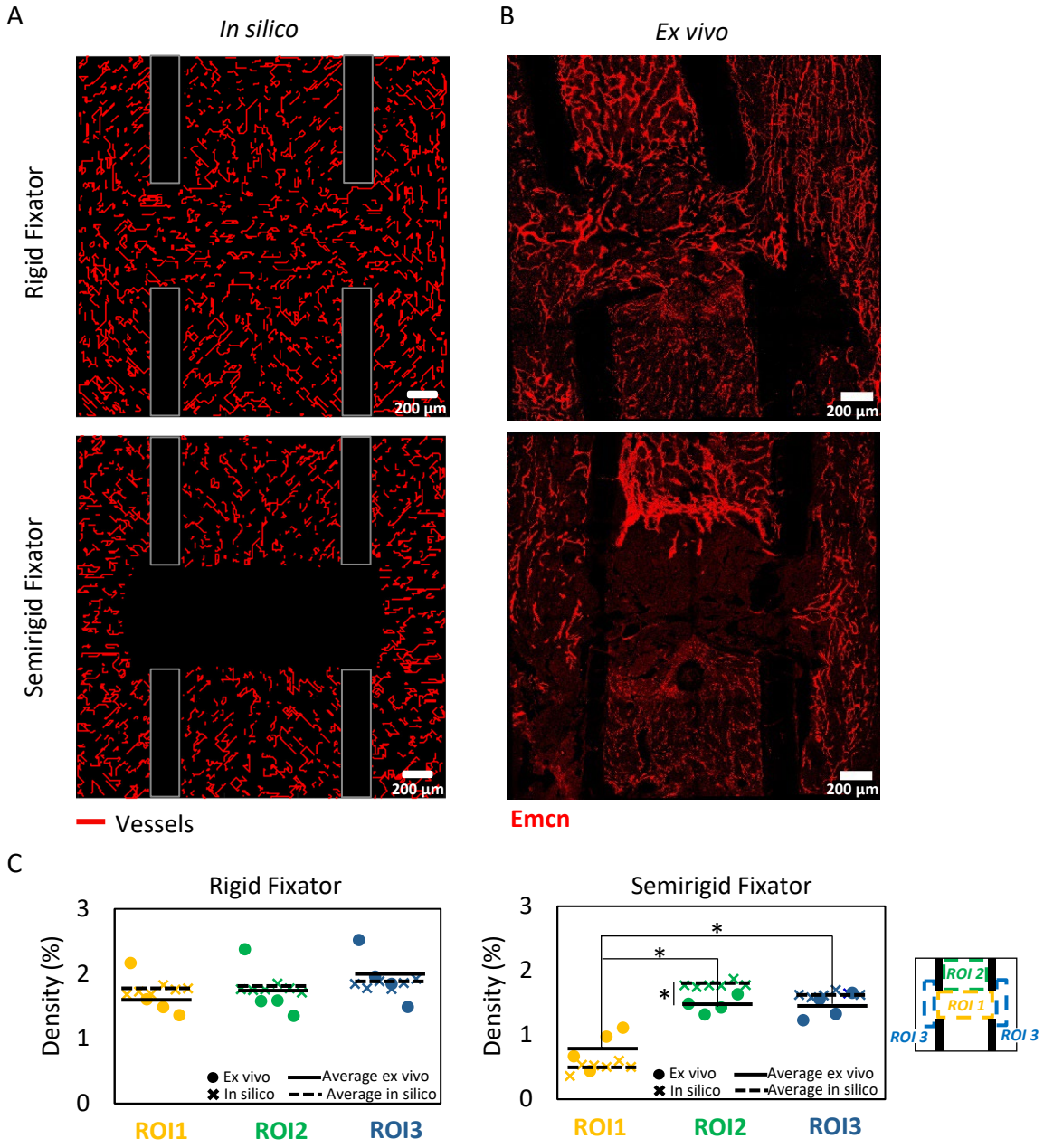

Figure 4.2: Predicted vessel organisation within the healing region and comparison with experimental data. ***(A)*** *Predicted vessel organisation on the 7th day post-surgery under rigid (top) and semirigid (bottom) fixation conditions.* ***(B)*** *Ex vivo vessel organisation on the 7th day post-surgery under rigid (top) and semirigid (bottom) fixation conditions. Vessels are stained in red (Emcn, Endomucin). Scale bar 200 µm.* ***(C)*** *Scatter plot of experimental vs. predicted vessel density in ROIs under rigid (left) vs. semirigid (right) fixation conditions. Circles represent experimental samples (N=4); crosses represent in silico realisations (N=6); solid lines indicate the average experimental vessel density; dashed lines indicate the average in silico vessel density. Significance levels are indicated as follows: * $p < 0.05$, ** $p < 0.01$.*

The predicted vessel organisation appeared to reproduce the preferential alignment of newly formed sprouts observed experimentally across the different ROIs (Fig. 4.3). Under

rigid fixation, vessels were found to align preferentially along the bone's long axis (90° direction) within the bone marrow (ROI 2) and in the periosteal region (ROI 3) (Fig. 4.3 A)., following the direction of absolute principal strains (Fig. 4.1 B). As vessels advanced towards the gap (ROI 1), increasing strain levels resulted in their gradual reorientation towards the direction orthogonal to the bone long axis (0° direction) (Fig. 4.3 A). Under semirigid fixation, vessels organised similarly to the rigid case within the bone marrow (ROI 2) but took on a preferential 0° direction at the periosteal site (ROI 3) (Fig. 4.3 B).

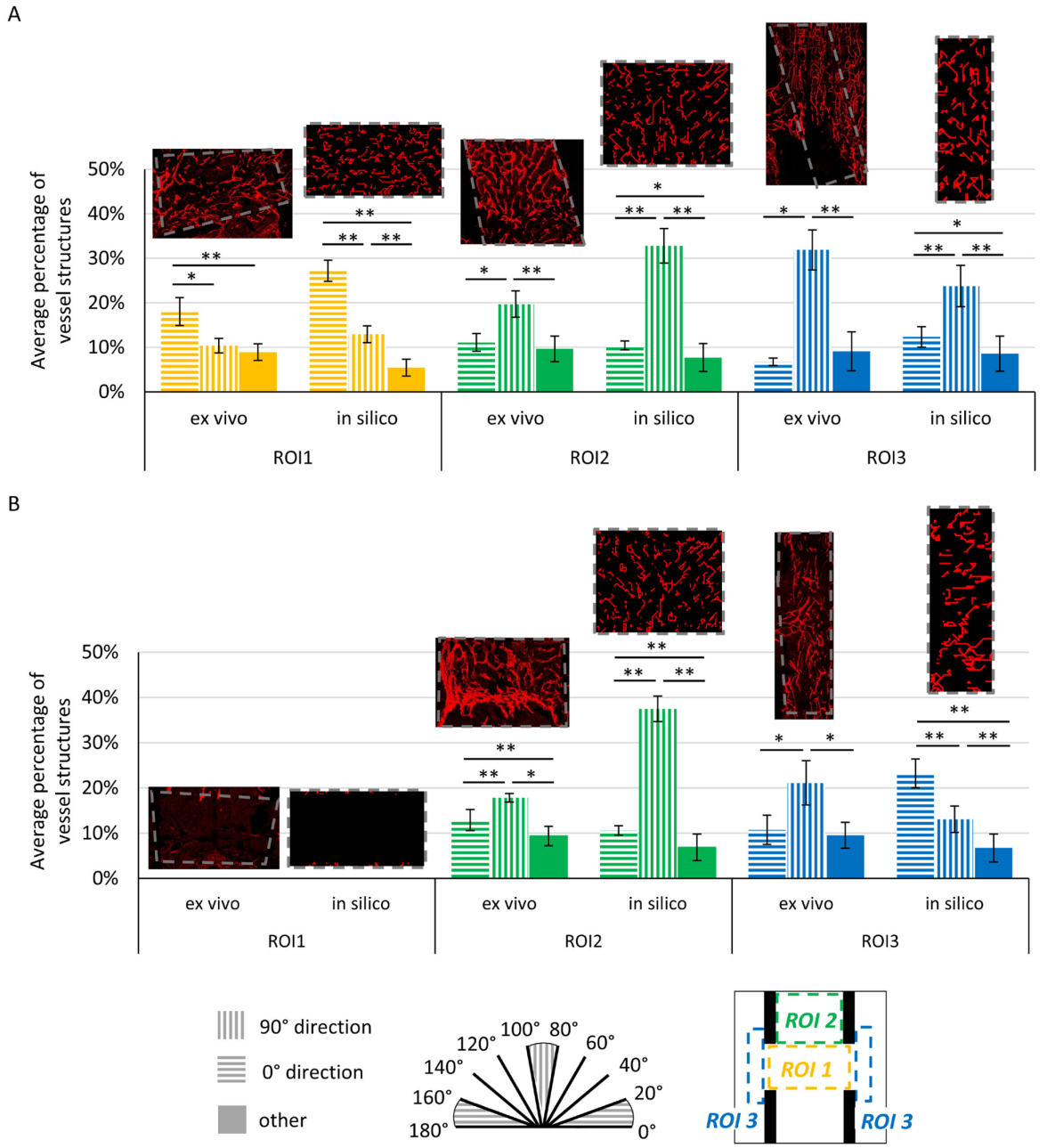

Figure 4.3 Comparison of the predicted vessel orientation with experimental data across ROIs. *Vessel orientation analysis ex vivo vs. in silico for the rigid* ***(A)*** *and semirigid* ***(B)*** *fixators. Zoomed-in ROIs above the bar plots illustrate qualitative differences between ex vivo and in silico vessel organisation. The colours represent the ROIs, the patterns represent the preferred direction: 90°, 0°, other. N=6. Significance levels are indicated as follows: * $p < 0.05$, ** $p < 0.01$.*

4.2 Tip EC response to mechanical cues appears to be key to vessel growth

After inhibiting the tip EC mechano-response, vessel organisation appeared altered compared to the baseline model (Fig. 4.4 A). While vessels were predicted to align preferentially orthogonal to the bone's long axis direction within the gap in the baseline model, no remarkable preferential orientation was observed upon the inhibition of tip EC mechano-response (Fig. 4.4 A). This was confirmed by the vessel orientation analysis of the EC_MR_KO model: significant differences occurred only between 80°-100° and 120°-140°, and between 80°-100° and 160°-180°, among the angle bins with a higher percentage of vessel structures (0°-20°,40°-60°,80°-100°,120°-140°,160°-180°) (Fig. 4.4 B). Analysis of vessel morphology revealed structural differences upon inhibition of EC mechano-response. Specifically, vessel length decreased under mechano-response inhibition compared to the baseline case, from an average length of 85 µm to 75 µm (p value < 0.01). This can be explained by the increased number of vessels that create closed loops by intersecting their own path (71±5.9 baseline vs. 85.3±8.1 EC_MR_KO), and thus no longer elongate.

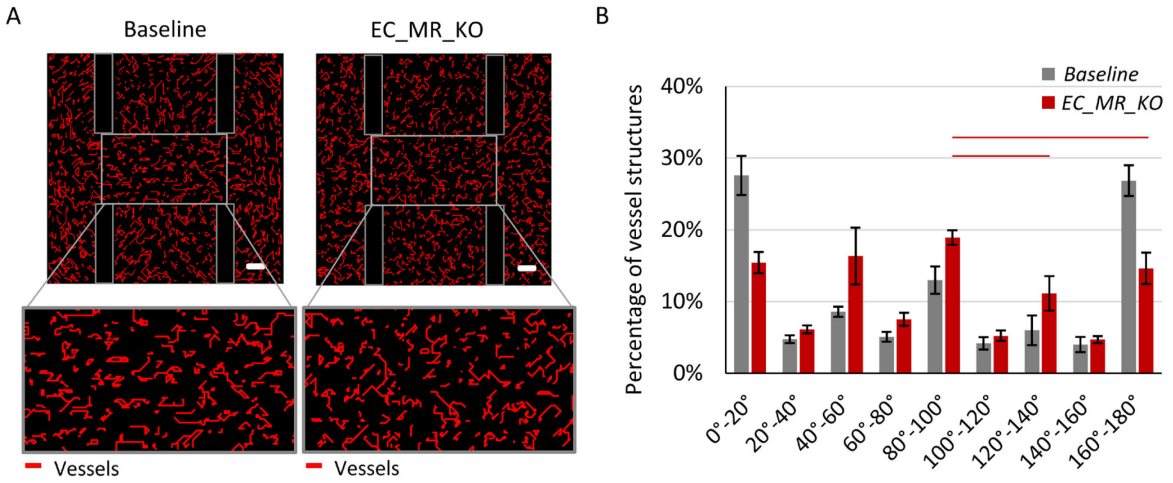

Figure 4.4: Predicted vessel organisation upon ECs mechano-response inhibition vs. baseline. ***(A)*** *Predicted vessel distribution for the baseline (left) and EC_MR_KO (right), with zoomed views of the osteotomy gap displayed below. Scale bar 200 µm.* ***(B)*** *Vessel orientation analysis for EC_MR_KO and baseline within the gap. Lines indicate a significant difference in the pairwise comparisons between angle bins in the EC_MR_KO model (p<0.05). N=6. EC_MR_KO=inhibition of tip ECs mechano-response.*

4.3 *Durotaxis* can explain OVSCs organisation during early bone healing

Due to a lack of experimental data on OVSCs organisation during the early stages of bone healing, a direct comparison was not possible. The predicted OVSCs alignment 7 days post-surgery was compared to the experimentally observed alignment of collagen fibres during the early healing phase. Indeed, it has already been shown that ECM fibre organisation relates well with cell orientation [128, 129], since cells remodel and align their ECM by exerting traction forces [24, 132] and in turn the aligned fibres are known to influence cell migration and reorientation [133]. Experimental data and *in silico* results were compared in two regions of interest where collagen fibres were preferentially aligned along the bone cortical surfaces (Fig. 4.5 A): the bone periosteum and the endosteal gap. Under both fixators, OVSCs were predicted to align similarly to collagen fibres: around 70% of OVSCs aligned perpendicular to the bone's long axis within the gap, while at the periosteum, nearly 50% of OVSCs aligned along the long bone axis direction (Fig. 4.5 B-C).

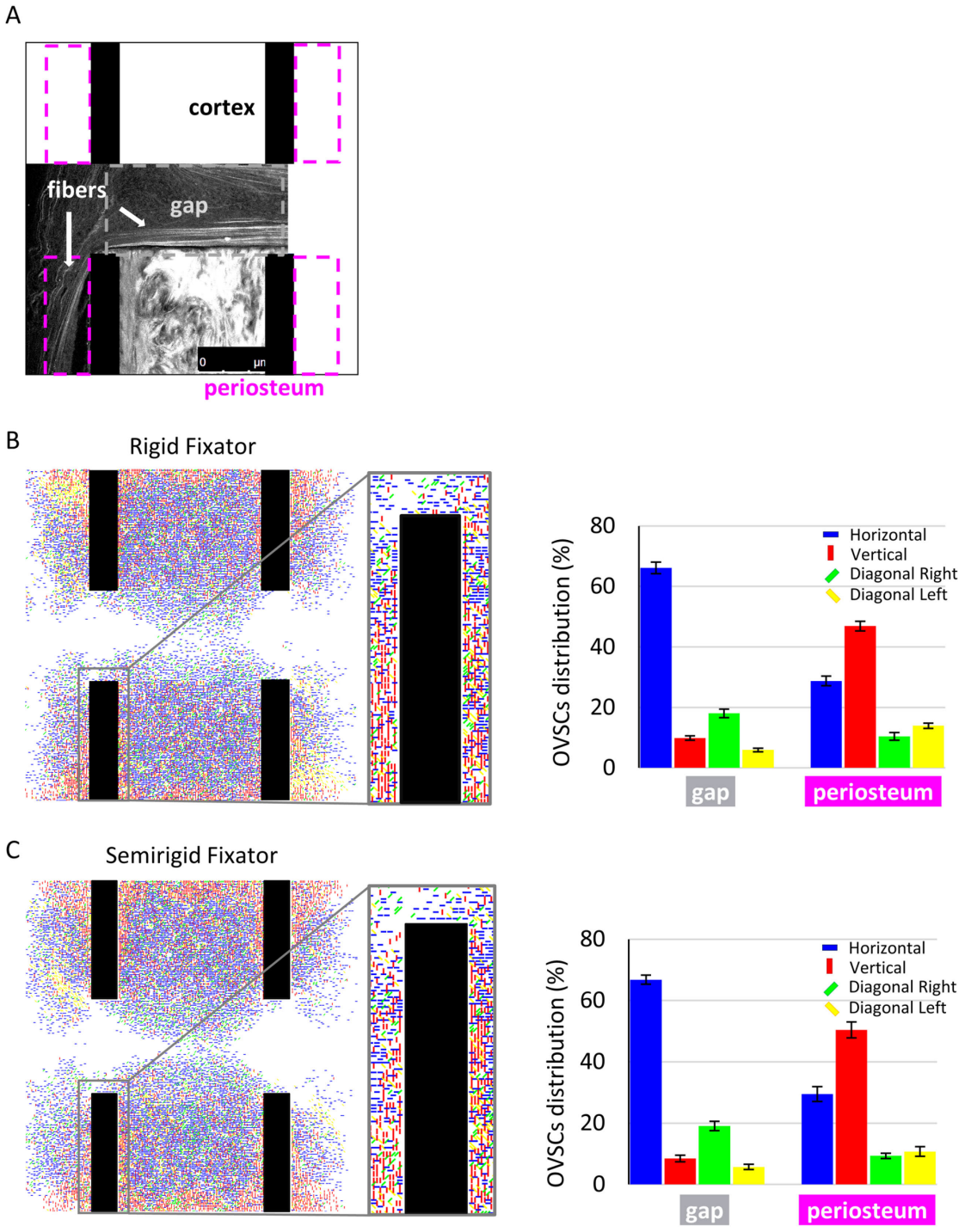

Figure 4.5: Predicted OVSCs organisation within the healing region and comparison with experimental data. ***(A)*** *Organisation of newly formed collagen fibres (indicated by white arrows) in the proximity of the cortex (second harmonic signal, two-photon microscopy) during the initial healing phase. The regions of interest considered in the analysis are identified with dashed lines.* ***(B-C)*** *Predicted OVSCs organisation on the 7th day post-surgery for the rigid* ***(B)*** *and semirigid* ***(C)*** *fixator (left) and percentage distribution of OVSCs orientation within the gap and along the periosteum (right). N=6.*

4.4 High external loads overrule cell-cell mechanical interactions

To better understand the impact of OVSCs-induced traction forces on sprout patterning, traction forces exerted by OVSCs were removed from the model. Interestingly, vessel organisation upon traction forces inhibition in OVSCs appeared similar to the baseline model (Fig. 4.6 A). The vessel orientation analysis revealed an analogous distribution of vessel orientations for both the baseline and the OVSC_TF_KO models in the three regions of interest and over each angle interval (Fig. 4.6 B).

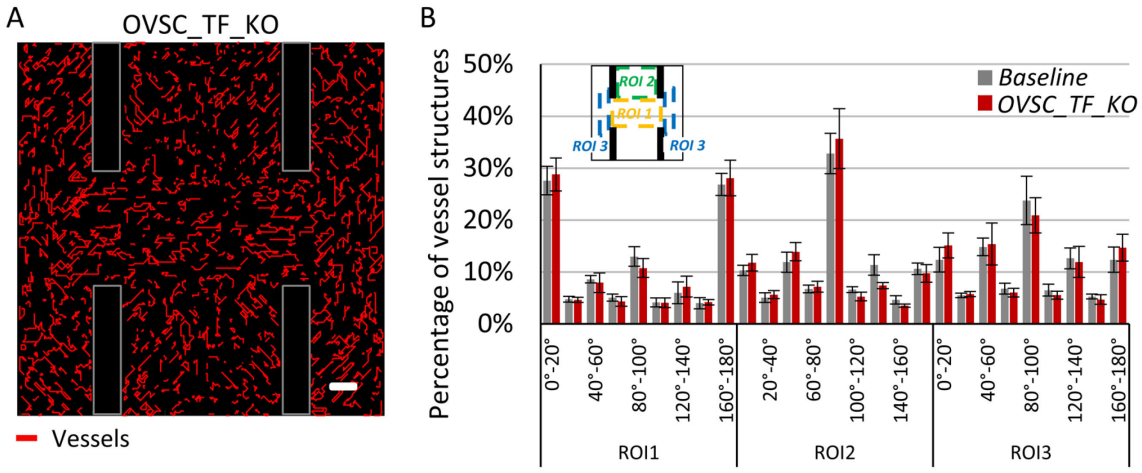

Figure 4.6: Predicted vessel organisation upon OVSC traction force inhibition (OVSC_TF_KO) vs. baseline. (A) *Predicted vessel distribution for the OVSC_TF_KO model. Scale bar 200 µm.* ***(B)*** *Vessel orientation analysis for OVSC_TF_KO and baseline within the ROIs. N=6. OVSC_TF_KO=inhibition of OVSCs traction forces.*

4.5 Cell-cell mechanical interactions emerge after unloading the bone

Given the negligible influence of OVSCs traction force inhibition on vessel patterning, the effect of cell-generated forces was further isolated by unloading the cortices and applying fully restrained boundary conditions across all six degrees of freedom. Two cases were investigated: (1) unloaded bone but active OVSCs contractility (unloading baseline) and (2) unloaded bone with inhibition of traction forces in OVSCs (unloading OVSC_TF_KO). The predicted vessel network differed depending on the presence or absence of cell traction forces (Fig. 4.7 A). In the unloaded baseline model, vessel structures

within the gap were found to be mainly aligned along the bone long axis direction (Fig. 4.7 B), opposite to the baseline model with externally applied loads (Fig. 4.3). In the unloaded OVSC_TF_KO model, vessels did not show any preferential alignment (Fig. 4.7 B).

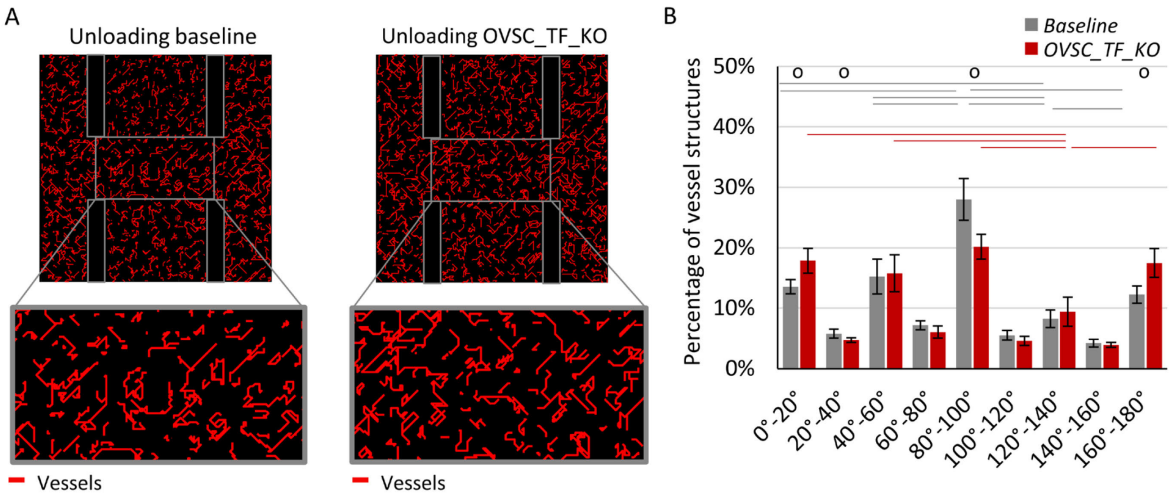

Figure 4.7: Predicted vessel organisation after unloading the cortices for the baseline vs. upon inhibition of OVSC traction forces. ***(A)*** *Predicted vessel distribution for the unloaded baseline model (on the left) and for the unloaded OVSC_TF_KO model (on the right) with zoomed views of the osteotomy gap displayed below.* ***(B)*** *Vessel orientation analysis for the unloaded baseline and unloaded OVSC_TF_KO models within the osteotomy gap. Empty circles indicate a significant difference ($p<0.05$) between the unloading baseline and unloading OVSC_TF_KO models. Lines indicate a significant difference in the pairwise comparisons between angle bins in the same model ($p<0.05$). N=6. OVSC_TF_KO=inhibition of OVSCs traction forces.*

To better investigate what is driving the vessel preferential alignment in the baseline unloaded model, the induced strain fields were analysed. Absolute maximum principal strains within the healing region were reduced as compared to the loaded cases, below 2% (Fig. 4.8 A). Cellular traction forces induced mainly compressive strains within the callus, however, mild tensile strains were predicted within the gap (Fig. 4.8 A). Interestingly, principal strain directions within the gap were found to be aligned along the bone long-axis (Fig. 4.8 B), similar to the vessel preferential orientation predicted in that region. After unloading, mechanical signals within the healing region are induced by the cell contractility only. Indeed, the OVSCs orientation within the gap aligns with principal strain directions: over 50% of OVSCs within the gap were predicted to align along the direction of the bone long axis (Fig. 4.8 C).

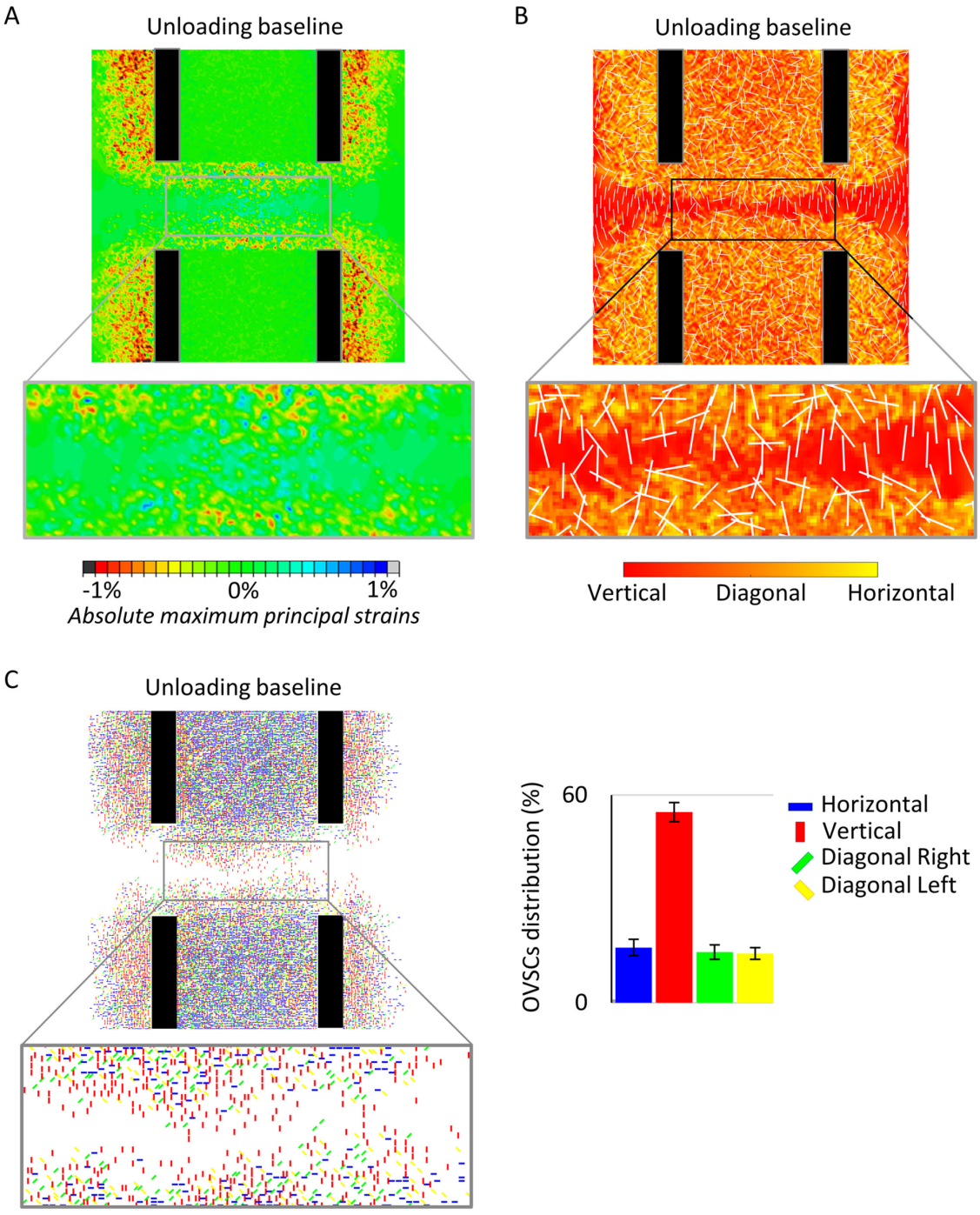

Figure 4.8: Predicted principal strain distribution, orientation and cell organisation after unloading the cortices for the baseline model. ***(A)*** *Predicted principal strain distribution for the unloaded baseline model with a zoomed view of the osteotomy gap.* ***(B)*** *Predicted principal strain directions for the unloaded baseline model with a zoomed view of the osteotomy gap.* ***(C)*** *Predicted OVSCs organisation for the unloaded baseline model with zoomed view of the gap and percentage distribution of OVSCs orientations for the unloaded baseline model within the gap.*

4.6 Discussion

Understanding the mechanobiological regulation of early angiogenesis is crucial to advance treatment strategies for bone fractures, as timely vascularisation is key to successful healing [2, 3]. Bone defects stabilised with fixators of different stability have been shown to influence vascularisation, leading to the formation of vascular networks with different patterns [90, 91], likely due to the different mechanical environment induced within the healing region. Outer vascular cell-induced traction forces and externally applied loads are both known to influence angiogenesis, however, their specific contribution to vessel patterning during early bone healing remains largely unknown. A multiscale computer model of the mechano-regulation of OVSCs and ECs organisation during the early stages of bone healing was developed to investigate the influence of both external loads and cell traction forces on the sprouting process. The computer model replicated an *in vivo* experiment in mice consisting of a bone defect stabilised with a rigid or a semirigid fixation [91]. Comparison of *in silico* results with *ex vivo* data confirmed that the implemented mechano-biological rules captured ECs and OVSCs organisation during early bone healing, showing that levels of mechanical strains and principal strain directions can explain vessel patterning, while *durotaxis* guides OVSCs organisation. Building on this, additional *in silico* experiments were carried out by selectively isolating the mechanical signals acting at the cell (traction forces) and tissue (external loads) levels to better understand their role in early sprout patterning. The results revealed a key role for tip EC mechano-response and demonstrated that high external loads primarily drive angiogenesis, whereas cell-generated forces appear to impact angiogenesis in the absence of high external loads.

Mechano-regulation of vessel patterning

The predicted vascular network within the healing region resembled the experimental one in terms of vessel density and patterning on the 7th day post-surgery. The lack of vascularity observed experimentally within the gap under semirigid fixation could be explained by the high mechanical strains locally, above 30%, known to inhibit vessel growth [89].

The predicted preferential alignment of vessels within the three regions of interest was in agreement with the *ex vivo* data under both fixators. Under both fixators, vessels were predicted to follow the principal strain directions in regions characterised by low levels of mechanical strains (<5%), such as the bone marrow or the periosteum for the rigid fixator. Under rigid fixation, vessels were found to gradually orient perpendicular to the principal strain directions while invading the endosteal gap, due to the high strains predicted in this region and the known tendency of vessels to align perpendicular to the strain directions for high levels of mechanical strain [19-22, 106].

Inhibition of tip ECs mechano-response, i.e. ECs ability to respond and adapt their behaviour based on local mechanical signals, resulted in a less organised vascular network with vessels characterised by shape defects as compared to the baseline simulation, suggesting a key role of tip EC mechano-response for vessel growth. This compares well with the disturbed vessel formation observed experimentally in the mouse retina upon inhibition of YAP-TAZ, i.e. molecules of a key mechano-signalling pathway [134]. From a clinical perspective, delayed bone healing in the elderly has been associated with a reduced cell mechano-response [92]. The present findings suggest that such an alteration in ECs may hinder early angiogenesis and thus contribute to the clinically observed delayed healing in the elderly.

Durotaxis-guided OVSCs organisation

OVSCs orientation distribution on the 7th day after surgery was compared with the early organisation of ECM collagen fibres in a comparable mouse osteotomy experiment [6], in line with the well-documented bidirectional interaction between ECM fibre orientation and cellular alignment [24, 128, 129, 132, 133]. Following a *durotaxis*-based rule, OVSCs were predicted to migrate and align predominantly along the cortical surfaces, in line with the collagen fibre orientation reported in the literature [6]. Moreover, within the gap, OVSCs were predicted to align mainly perpendicular to the bone long-axis under both fixators, in line with the preferential collagen fibre orientation measured in the dedicated mouse experiment [135], although the experimental orientation distribution was more dispersed under semirigid than under rigid fixation. Taken together, these findings suggest that *durotaxis*, a well-known mechanism guiding OVSC organisation *in vitro*, may also play a key role in directing early OVSC self-organisation *in vivo*.

External loads and cell-induced traction forces

In silico results upon inhibition of OVSCs traction forces suggest that high external loads can overrule the mechanical communication between OVSCs and ECs. Indeed, vessel organisation was not altered after preventing OVSCs from applying traction forces. This is a consequence of the high levels of strains induced by the external loads, replicating physiological activity, as compared to the small deformation induced locally by cell traction forces. Although this result appears in contrast with the known role of stromal cells in supporting the formation of the vascular network [25], experiments of OVSCs-ECs co-cultures available in the literature are usually performed without external loads [26, 27]. Further *in vitro* experiments, where inhibition of stromal cell traction forces would be performed on cyclically loaded substrates, should confirm these observations.

Although clinical studies have shown that unloading hinders bone healing [136, 137], the purpose of the unloading experiment was to isolate the cell-induced mechanical forces from the high external loads. After the cell-induced forces were isolated, hints of the ECs-OVSCs mechanical interaction emerged within the gap. OVSCs preferentially aligned along the bone long-axis, and their contractile activity generated strains oriented accordingly, thereby promoting vessel growth along the same direction. Gaggioli and colleagues [138] proposed a similar mechanism driven by stromal cells in the context of cancer research, demonstrating that stromal fibroblasts facilitate carcinoma cell migration and invasion by remodelling the matrix through force generation. The inhibition of OVSCs traction forces in the unloaded bone resulted in randomly oriented vessels, in line with observations by Rosenfeld and colleagues [26], who reported a loss of vessel alignment after inhibiting stromal cell ROCK (key regulator of cell contractility) within uniaxially constrained fibrin gels. Taken together, these findings suggest that in the absence of high external loads, matrix strains generated by OVSCs traction forces regulate vessel organisation, supporting previous experimental observations [26, 138].

Limitations and future work

The computer model presented here includes several limitations. A 2D model geometry was used to reduce computational time. Despite this simplification, the predicted average compressive strains matched the original 3D model [92] in terms of both magnitude and distribution in different regions of interest within the healing zone, validating the 2D

approach and its underlying assumptions for loading and boundary conditions. To further capture the 3D nature of the callus within this 2D framework, vessels were allowed to virtually grow in 3D space by allowing tip ECs to exit and/or re-enter the simulated plane. This approach allowed to obtain section-like images resembling *ex vivo* ones, by generating vessel fragments as the output of the model instead of a continuous vascular network, as seen in *ex vivo* 2D sections.

The model failed to reproduce a few aspects observed experimentally. First, the model slightly overestimated vessel density within the bone marrow under semirigid fixation. This could be due to the constant rate of vessel growth implemented in the model, derived from *in vivo* measurements [103], which does not account for the known sensitivity of ECs proliferation and migration to mechanical cues such as external loading [10] and matrix stiffness [139]. Second, under semirigid fixator, the model predicted a preferential alignment of vessels periosteally in the direction perpendicular to the principal strains, in contrast to the experiment. This can be explained by the high strain levels predicted in this region, above 20%, which caused vessels to deviate from the principal strain directions according to the mechano-biological rules implemented in the model. Other factors not included in the model, such as matrix fibres, are known to guide and direct vessel growth and might contribute to the vessel alignment observed in *ex vivo* images. Indeed, contact guidance from matrix topology has already been shown to override cell re-orientation in response to strains [140, 141]. Interestingly, here matrix fibres were found to align parallel to the bone cortices at the periosteum, matching the experimentally observed vessel alignment. This specific matrix organisation may prevent vessels from reorienting in response to strains due to contact guidance. Future improvements to the model should include fibre deposition and remodelling by OVSCs, as well as contact guidance for vessel growth, as already suggested in Chapter 3. These additions could help explain the vessel alignment observed experimentally in the periosteal region under semirigid fixation (along the bone long-axis) as stromal cells, known to contribute to fibre deposition and organisation, were predicted to align in a similar way (along the bone surface).

Although *in silico* results showed that external loads overrule the cell-cell mechanical interactions, this conclusion is based only on differences in force magnitude. Yet, traction forces and external loads act on different timescales (cell traction forces change over minutes [142] while external loads, like those from walking, vary over seconds [143]). To better understand how ECs integrate mechanical loads occurring at different frequencies,

future work should incorporate time-dependent and dissipative tissue behaviours, such as viscoelasticity.

5

In silico investigation of angiogenesis and bone regeneration during scaffold-aided bone healing

In this Chapter, results related to the computer model of angiogenesis and bone regeneration during scaffold-aided bone healing will be presented and discussed.

5.1 The *in silico* model recapitulates vessel and bone formation processes within MEW and FDM scaffolds

Blood vessels were predicted to invade both FDM and MEW scaffolds and to reach the scaffold core at week 12 post-surgery, as observed experimentally [108] (Fig. 5.1 A). Vessels appeared more homogeneously distributed within the MEW scaffold volume compared to the FDM scaffold (Fig. 5.1 A). Throughout the healing period, the total number of vessels increased in both scaffolds, with a consistently higher vessel count within the MEW at all time points (Fig. 5.1 B). *In silico* predictions were quantitatively compared to experimental results in terms of vessel density computed within the same region of interest at week 12. The predicted vessel densities for both scaffolds resulted in the same order of magnitude of the experimental values; however, the model estimated a higher vessel density in MEW compared to FDM, opposite to experimental findings (Fig. 5.1 C).

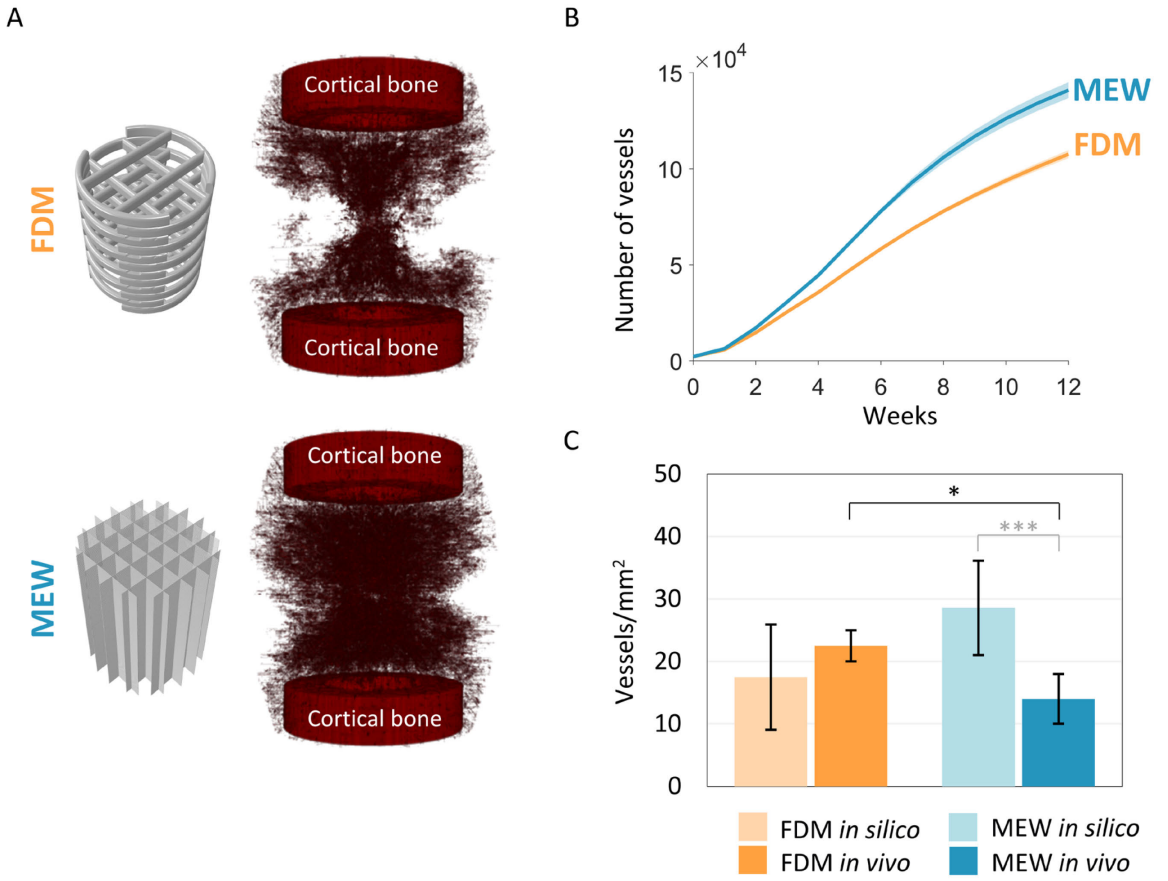

Figure 5.1: Vascularisation of FDM and MEW scaffolds. ***(A)*** *3D reconstruction of the predicted vessels within the callus at week 12 for FDM (top) and MEW (bottom) scaffolds.* ***(B)*** *Number of vessels predicted over time within FDM and MEW scaffolds. Solid lines display the mean value, shaded areas represent the range within one standard deviation (N=5 per scaffold type).* ***(C)*** *In silico (N=5 per scaffold type) vs. ex vivo (N=9 per scaffold type) vessel density within the region of interest after 12 weeks for FDM and MEW scaffolds. Error bars denote standard deviation. ∗ = statistical significance between scaffold groups; grey ∗ = statistical significance between in silico and experimental groups. Significance levels are indicated as follows: * $p < 0.05$, *** $p < 0.001$.*

The computer model predicted impaired bone healing in both scaffold types, as indicated by the incomplete closure of the defect, consistent with experimental observations (Fig. 5.2 A). The model reproduced the increased bone formation observed within the MEW scaffold after 12 weeks. The predicted bone morphology reflected features observed experimentally, showing tiny bone spicules through the FDM scaffold pores, although smaller than those visible in µCT scans, and more rounded bone ends within the MEW scaffold (Fig. 5.2 A). The regenerated bone volume was predicted to increase from week 6 to week 12 in both scaffold types, with values aligned with the experimental results (Fig. 5.2 B). Although the model slightly underestimated the bone volume within the FDM

scaffold at week 6, the predicted value remained within the experimental standard deviation (Fig. 5.2 B).

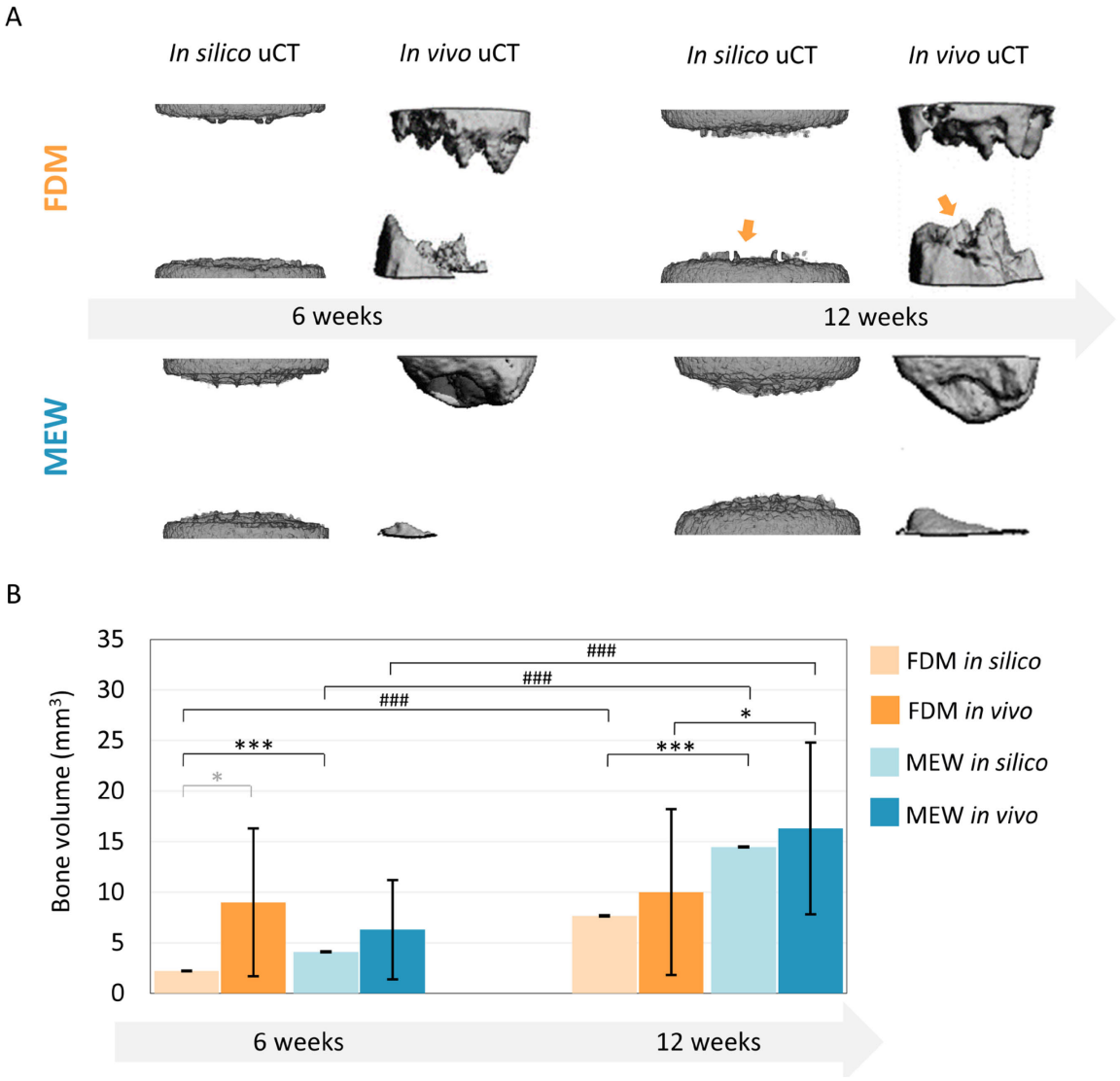

Figure 5.2: Newly regenerated bone within FDM and MEW scaffolds. (A) *In silico vs. in vivo µCT reconstructions of the newly regenerated bone after 6 and 12 weeks within the FDM (top) and MEW (bottom) scaffolds. Orange arrows indicate the spicules through the FDM pores. In vivo µCTs are reproduced from Eichholz et al., 2022 [108] under Creative Commons Attribution 4.0 License.* ***(B)*** *In silico (N=5 per scaffold type) vs. in vivo (N=9 per scaffold type) bone volume after 6 and 12 weeks within the FDM and MEW scaffolds. Error bars denote standard deviation. ∗ = statistical significance between scaffold groups; grey ∗= statistical significance between in silico and experimental groups; # = statistical significance within scaffold groups between time-points. Significance levels are indicated as follows: * $p < 0.05$, *** $p < 0.001$, ### $p < 0.001$.*

5.2 The *in silico* model captures tissue formation patterns within scaffolds

The organisation of the regenerating tissues within the two scaffold architectures was evaluated by generating histological-like images from *in silico* results at week 12, illustrating the spatial distribution of bone, cartilage and fibrous tissue. The computer model predicted the newly formed bone to close the bone marrow within both scaffolds, as observed experimentally in the Goldner's Trichrome-stained histological sections (Fig. 5.3 A). Fibrous tissue formation was predicted to be more pronounced in the FDM scaffold compared to the MEW scaffold (Fig. 5.3 A), as confirmed quantitatively by computing the percentage of fibrous tissue over the total regenerated volume: 20% for FDM and 12% for MEW. This is a consequence of the high mechanical stimuli around FDM struts, falling within the range that promotes fibrous tissue formation (Fig. 5.7 A). Cartilage was predicted to form in both scaffolds, with larger cartilage islands within the FDM scaffold compared to the MEW (Fig. 5.3 B), as confirmed by the percentage of cartilage tissue over the total regenerated volume: 12% for FDM and 6% for MEW. Notably, cartilage was predicted to accumulate near the bone ends, as observed in the Safranin O staining performed on *ex vivo* sections (Fig. 5.3 B).

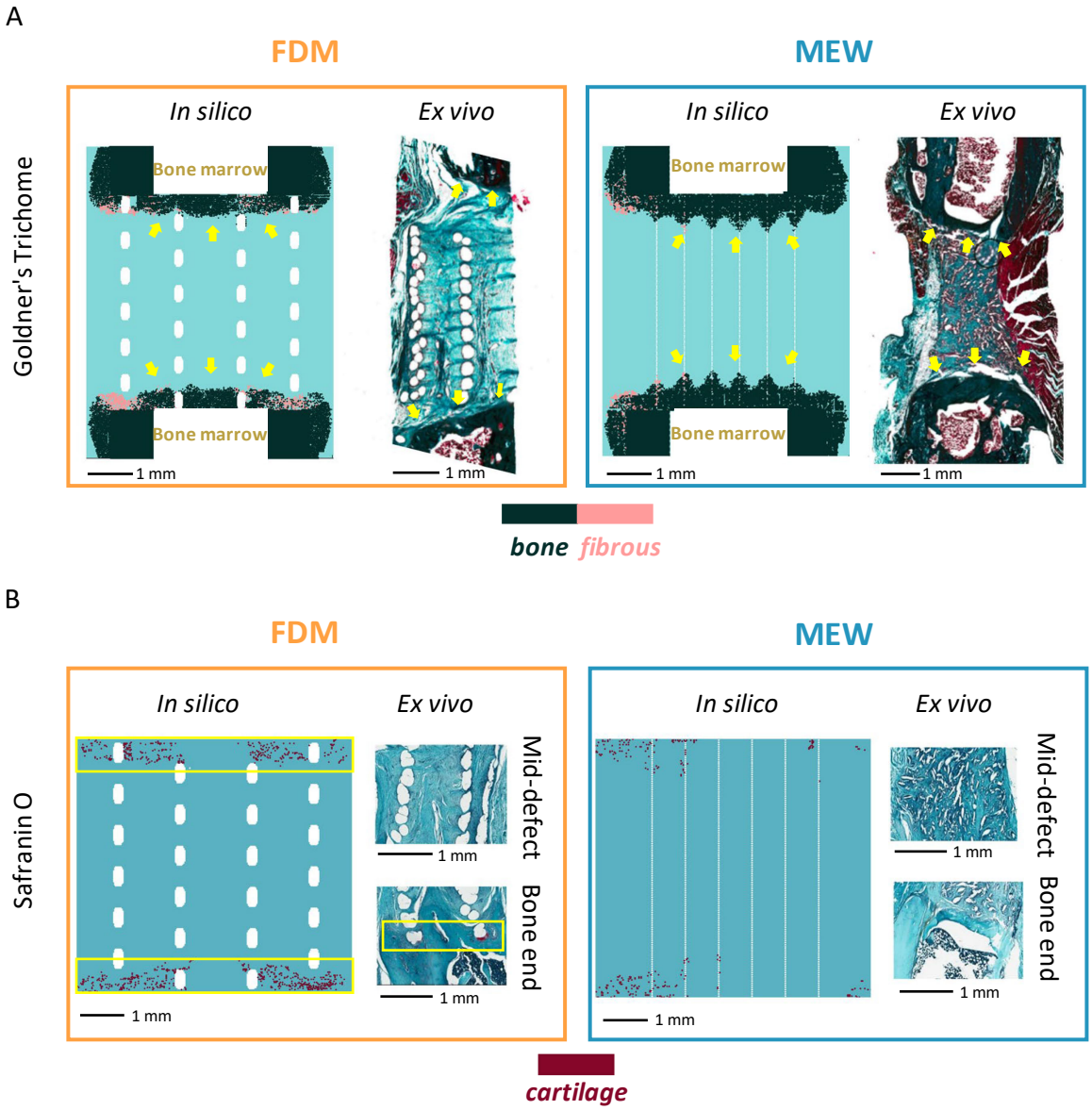

Figure 5.3: Tissue organisation within FDM and MEW scaffolds. (A) *In silico vs. ex vivo Goldner's Trichome staining within the longitudinal mid-section of FDM (left) and MEW (right) scaffolds. Histological staining shows bone in dark green and unspecific soft tissue in red. Predicted fibrous tissue is shown in pink. Yellow arrows indicate bone tissue closing the bone marrow gap.* ***(B)*** *In silico vs. ex vivo Safranin O staining within the longitudinal mid-section of FDM (left) and MEW (right) scaffolds. Histological staining shows cartilage in red. Yellow boxes highlight cartilage tissue near the bone ends. Ex vivo images are reproduced from Eichholz et al., 2022 [108] under Creative Commons Attribution 4.0 License.*

5.3 High porosity induces mechanical strains that accelerate angiogenesis

Lower mechanical strains were predicted within the FDM scaffold central pores compared to the MEW (Fig. 5.4 A). Broader regions characterised by strain levels falling within the 5-10% range, known to enhance vessel growth [15-18, 89], were predicted within the MEW scaffold (Fig. 5.4 A). Specifically, 48% of the callus volume in the MEW scaffold experienced strains within this range, compared to 31% in the FDM scaffold (Fig. 5.4 A). Although the FDM scaffold generally induced lower strain magnitudes, localised regions of high strains exceeding 30% were detected around scaffold struts (Fig. 5.4 A). These high-strain regions, known to inhibit vessel growth [89], were found to affect an increasing number of vessels over time within the FDM scaffold (Fig. 5.4 B).

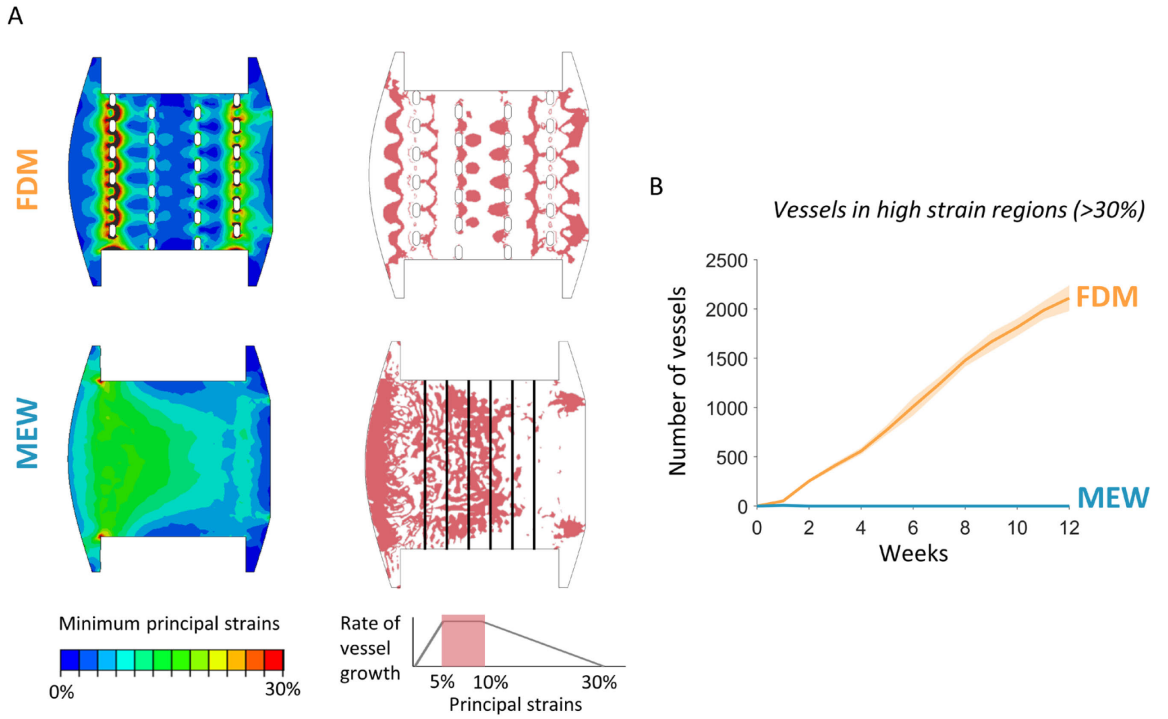

Figure 5.4: The role of the mechanical environment on the predicted vessel growth within FDM and MEW scaffolds. (A) *Contour plots of the minimum principal strains (left) with areas characterised by principal strains between 5% and 10% highlighted on the right, within FDM (top) and MEW (bottom) scaffolds.* ***(B)*** *Number of vessels predicted in regions characterised by strains above 30% within FDM and MEW scaffolds over time. Solid lines display the mean value, shaded areas represent the range within one standard deviation (N=5 per scaffold type).*

To isolate the influence of the scaffold architecture from the mechanical cues, vessel growth rate was set constant and corresponding to the optimal strain range for

angiogenesis (5-10%). As a result, the total vessel elongation over time increased within both scaffold types (Fig. 5.5 A). In particular, the FDM scaffold exhibited a more pronounced rise in total vessel elongation as compared to the simulations with mechanics-dependent vessel growth, further indicating that its mechanical environment compromised vessel ingrowth (Fig. 5.5 A). This was mainly visible from week 3, while the initial spike at the beginning of the curves in both scaffolds resulted from the higher rate of vessel growth assumed during the latency period. However, the total vessel elongation was still predicted to be higher for the MEW scaffold as compared to the FDM scaffold, and this appeared to be attributable to its more open and accessible architecture for vessels. Indeed, the number of vessels prevented from growing further because physically blocked by the scaffold struts was found to be higher in FDM throughout the simulation period (Fig. 5.5 B).

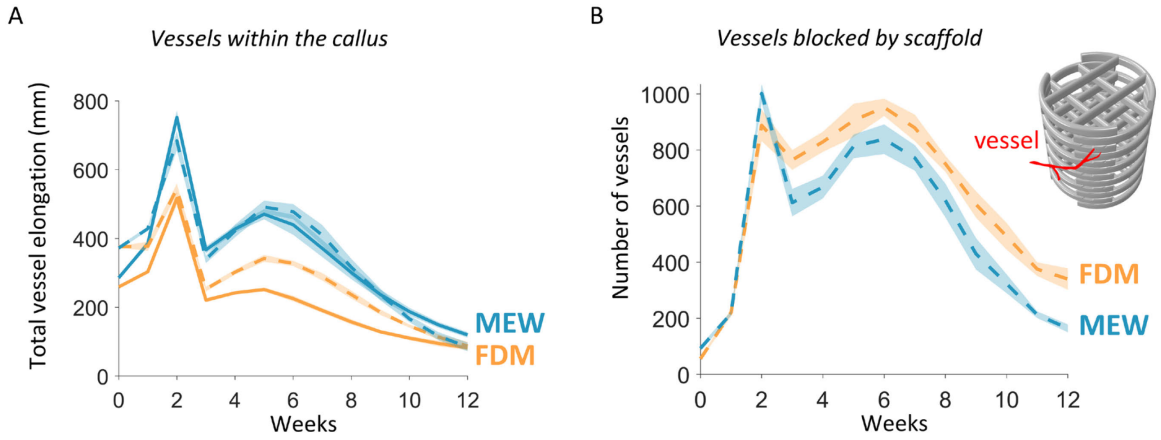

Figure 5.5: The role of the scaffold architecture on the predicted vessel growth within FDM and MEW scaffolds. ***(A)*** *Total vessel elongation when assuming mechanics-dependent (solid lines) vs. constant (dashed lines) growth rate within FDM and MEW scaffolds over time. Shaded areas represent the range within one standard deviation (N=5 per scaffold type).* ***(B)*** *Number of vessels over time blocked by the scaffold structure within FDM and MEW scaffolds, when assuming a constant vessel growth rate. Dashed lines display the mean value, shaded areas represent the range within one standard deviation (N=5 per scaffold type).*

5.4 Large pore size on the outer scaffold surface facilitates periosteal vessel infiltration

To better understand what is driving the increased vessel ingrowth observed experimentally within the FDM scaffold and not captured by the baseline computer model, *in silico* experiments were performed. First, the contributions from the two vessel sources, the periosteum and bone marrow, to vascular ingrowth within the scaffolds were evaluated independently by allowing vessels to grow exclusively from either the periosteum

("Periosteum only") or the bone marrow ("Bone marrow only"). The total number of vessels was observed to increase over time for both scenarios in both scaffolds, but a stronger angiogenic response was predicted from the periosteum (Fig. 5.6 A-B). Since periosteal vessels must infiltrate the scaffold from the lateral side, pore size on the outer surface plays a critical role in determining accessibility. Narrow pores of 20 μm, like those characterising the MEW scaffold outer surface, may physically restrict the entry of larger periosteal vessels. To test this hypothesis, a proof-of-concept simulation was performed assuming a larger vessel diameter of 40 μm. The model predicted an increased vascularisation within the FDM scaffold compared to MEW, reflecting experimental trends, although vessel density was generally underestimated (Fig. 5.6 C). Notably, the predicted newly deposited bone slightly decreased as a consequence of the reduced vessel ingrowth, but the MEW scaffold still supported higher levels of regenerated bone overall (Fig. 5.6 D).

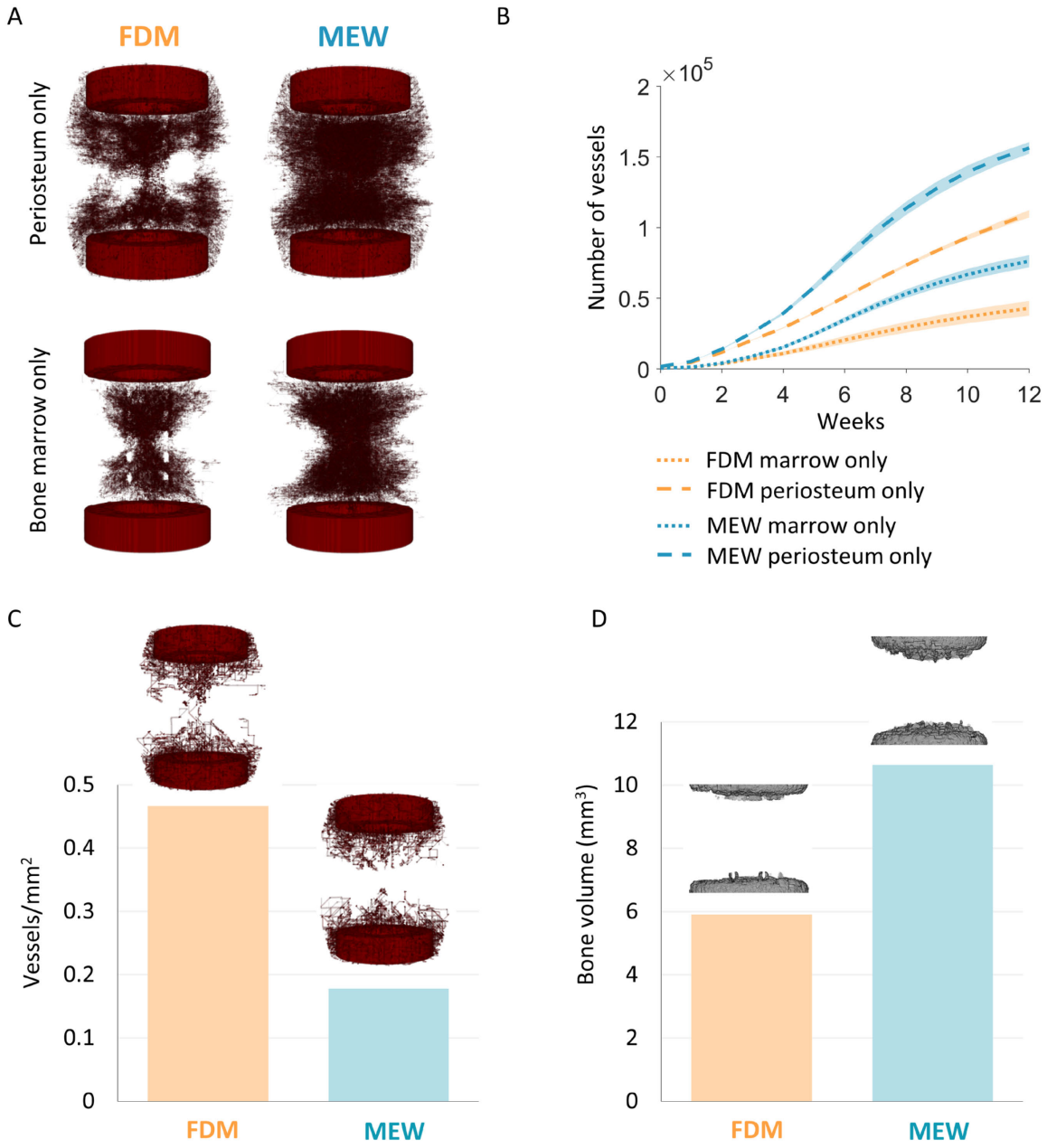

Figure 5.6: Influence of vessel source and diameter on scaffold revascularisation. ***(A)*** *3D reconstruction of the predicted vessels within the callus at week 12 for FDM (left) and MEW (right) scaffolds when allowing vessels to grow exclusively from the periosteum (top) or the bone marrow (bottom).* ***(B)*** *Number of vessels predicted over time within FDM and MEW scaffolds in the different scenarios simulated. The legend is displayed below the graph. Shaded areas represent the range within one standard deviation (N=5 per scaffold type).* ***(C)*** *In silico vessel density within the region of interest after 12 weeks for FDM and MEW scaffolds when assuming 40µm-diameter vessels. 3D reconstruction of predicted vessels is displayed above the barplots.* ***(D)*** *In silico bone volume after 12 weeks for FDM and MEW scaffolds when assuming 40µm-diameter vessels. µCT reconstructions of the predicted newly regenerated bone are displayed above the barplots.*

5.5 Reduced strut spacing and higher surface area-to-volume ratio lead to enhanced bone regeneration

The differentiation of MSCs into osteoblasts, chondrocytes or fibroblasts was modelled as a function of the mechanical stimulus, determined by strains and fluid flow, which is known to indicate the type of tissue most likely to form during the healing process [81]. The distribution of the mechanical stimulus across the callus appeared asymmetric due to the applied bending loads and the presence of the internal fixator on the medial (right) side (Fig. 5.7 A). This resulted in higher (fibrous) stimulus on the lateral (left) side of both scaffolds, even though this asymmetry appeared less pronounced in the FDM scaffold due to its higher stiffness [36, 144] and enhanced load-bearing properties. Larger proportions of volume exposed to bone-favourable mechanical stimuli were found within the FDM scaffold (60% post-surgery, 57% after 12 weeks) as compared with the MEW scaffold (30% post-surgery, 34% after 12 weeks). Despite this, enhanced osteoblast differentiation and proliferation were predicted within the MEW scaffolds, aligning with the higher level of bone formation observed in this group (Fig. 5.7 B-C). A higher percentage of MSCs within the FDM scaffold failed to differentiate into osteoblasts due to the absence of sufficient surfaces for cell attachment, a prerequisite for cell differentiation (Fig. 5.7 D). The percentage of MSCs that failed to find a surface increased sharply in both scaffolds during the first 18 days, after which the FDM curve was consistently above the MEW one (Fig. 5.7 D).

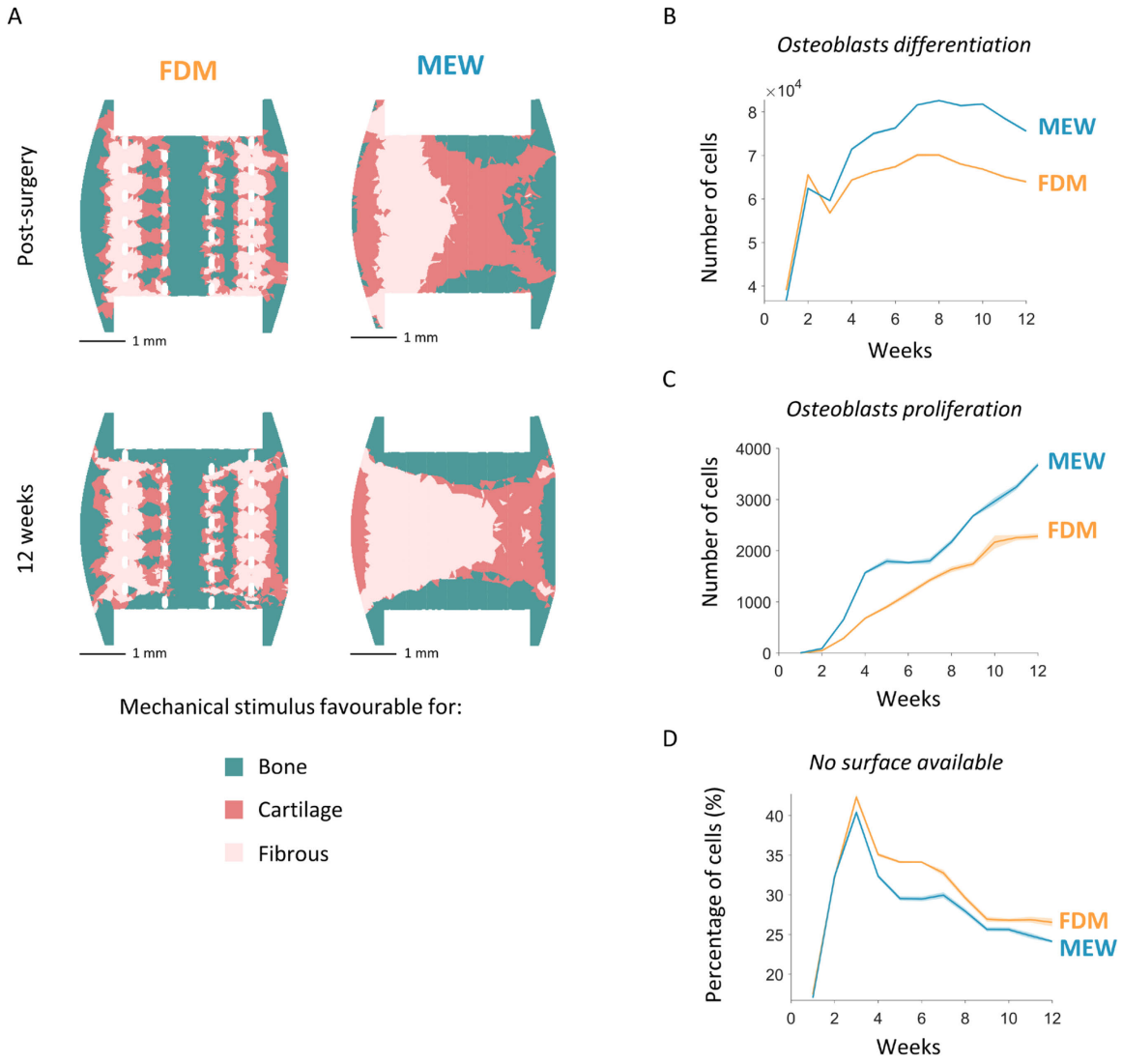

Figure 5.7: The role of the mechanical environment and scaffold architecture on bone regeneration within FDM and MEW scaffolds. ***(A)*** *Distribution of the mechanical stimulus within the longitudinal mid-section post-surgery (top) and after 12 weeks (bottom) within the FDM (left) and MEW (right) scaffold.* ***(B)*** *The number of MSCs differentiating into osteoblasts over time within FDM and MEW scaffolds.* ***(C)*** *The number of proliferating osteoblasts over time within FDM and MEW scaffolds.* ***(D)*** *The percentage of MSCs that could not differentiate into bone because of the absence of surfaces, over time, within FDM and MEW scaffolds. Solid lines display the mean value, shaded areas represent the range within one standard deviation (N=5 per scaffold type).*

5.6 Discussion

Three-dimensional printed scaffolds have emerged as a promising treatment alternative for large bone defects, as supported by several preclinical and clinical studies [30-37]. However, revascularisation of large scaffolds is one of the major limitations to their clinical translation. To optimise scaffold designs for improved vascularisation and subsequent

bone healing, a deeper understanding of the mechano-biological processes behind scaffold-aided angiogenesis and bone regeneration is essential. Scaffolds fabricated with different 3D printing techniques, either FDM or MEW, were shown to induce different levels and patterns of vessel ingrowth and bone regeneration in large defects in rats [108]. In this study, a mechano-biological computer model was developed to investigate the role of scaffold architecture and mechanical cues on angiogenesis and bone regeneration within FDM and MEW scaffolds. The computer model recapitulated vessel growth and the bone regeneration progression observed experimentally within the two scaffolds. Thereafter, the computational framework was used to separately assess the influence of scaffold architectural cues and the induced mechanical environment, challenging to isolate in experimental settings. Simulation results showed that the interplay between the mechanical environment within the scaffold and its architectural features can explain experimentally observed angiogenic and bone regeneration patterns. Specifically, strain levels, strut spacing, pore size and scaffold surface-area-to-volume ratio emerged as key regulators of angiogenesis and bone growth.

Previously, computational models have been developed to investigate angiogenesis and bone regeneration within scaffolds. Several computational models have provided insights into how the mechanical environment within scaffolds influences vessel growth and bone regeneration ([75-77, 145]), although the contribution of scaffold architectural cues was overlooked. A few computer models have been used to identify scaffold architectural features favouring angiogenesis and bone regeneration. For example, this study builds upon the mechanobiological scaffold-aided bone regeneration model of Perier-Metz et al. [109], who showed that a lower surface area-to-volume ratio can promote bone formation by facilitating cellular migration. However, angiogenesis was not included in the model. Mehdizadeh et al. [72] developed an agent-based model of angiogenesis within idealised porous scaffolds and found that large pore size and high porosity enhance vascularisation. Sun and colleagues [74] introduced a model coupling angiogenesis and bone regeneration, showing that porosity has a stronger influence than pore size on regeneration outcomes. However, both models were only partially validated against experimental results and did not include the effect of mechanical signals. This study introduces a computer model of angiogenesis during scaffold-aided bone regeneration, validated against dedicated in vivo experiments, to investigate how scaffold structural features and mechanical signals jointly orchestrate angiogenesis and bone formation.

Vessel and tissue growth patterns within scaffolds

The computer model predicted successful vascular infiltration throughout both scaffold types, reaching the scaffold core, in line with experimental observations [108]. Although the predicted vessel densities were in the same order of magnitude as those measured from *ex vivo* sections, the computer model showed higher vascular density within the MEW scaffold compared to FDM, in contrast to the experiment. Simulation results reproduced the bone healing progression within both MEW and FDM scaffold architectures. In particular, the model predicted the increased bone formation observed *in vivo* [108] within the MEW scaffolds. The predicted bone formation patterns were also consistent with *in vivo* findings, showing rounded bone ends within the MEW scaffolds and small bone spicules through the FDM scaffold pores.

Despite both scaffold types appeared well vascularised by week 12, full bone bridging was not achieved both experimentally and *in silico*. This result appears in contrast to the traditional positive correlation between vascularisation and bone regeneration. Previous studies have suggested that vascularisation is essential but may not be sufficient to ensure bone regeneration [146, 147]. For example, even within a vascularised environment, both optimal scaffold architecture (e.g. pore size [147]) and chemical properties (e.g. calcium ion depletion [146]) were shown to be fundamental to achieve successful bone regeneration.

The model captured additional features of the bone healing process, including the closure of the marrow cavity within both scaffolds and the formation of larger cartilage clusters within the FDM scaffold. These cartilaginous regions were located near scaffold struts, where high mechanical stimuli were predicted. Their presence may indicate ongoing endochondral ossification and potential for further bone formation beyond a 12-week period, as observed experimentally [108].

Strain levels and pore accessibility for vessel ingrowth

To better understand how the mechanical environment induced within the healing region contributed to the different vessel ingrowth predicted within MEW and FDM scaffolds, the mechanical strains induced within the two scaffolds were analysed. In the MEW group, a larger portion of the callus exhibited strains within the 5-10% range, known to support ECs proliferation and vessel elongation [10, 15-18]. Although the FDM scaffold induced generally lower strain levels due to its higher effective stiffness (8-26 MPa [36] for

FDM, 0.005-0.145 MPa [144] for MEW), elevated strains exceeding 30% were found at the FDM scaffold-tissue interface. These high strains further limited vessel invasion in the FDM scaffold, consistent with the experimental literature [89]. Overall, MEW scaffolds induced strains within the healing region favouring vessel ingrowth.

The role of the scaffold architecture on vessel growth was analysed by ruling out the vessel mechano-responsiveness, meaning that the vessel growth rate was set constant and independent of local strain levels. MEW scaffolds appeared to have a more accessible architecture for infiltration of 20 μm diameter vessels. Indeed, more vessels resulted in being blocked by the scaffold walls and prevented from growing further within the FDM as compared to the MEW scaffold. This suggests that the MEW structure is inherently more permissive to vascular ingrowth, as a consequence of its higher porosity and lower fibre diameter, leading to a higher probability for vessels to find open spaces. This is in line with the experimental literature reporting enhanced vessel infiltration for high porosity levels [52].

Pore size and vessel diameter

As previously discussed, the computer model failed to predict the increased vascularity observed experimentally within the FDM scaffold. One possible explanation for this discrepancy between *in silico* and *in vivo* results is a current simplification of the model, which is that vessels are assumed to have a constant diameter of 20 μm. While this approximation reflects the majority of vessel diameters in MEW scaffolds, FDM scaffolds exhibited a larger diameter distribution, including vessels with diameters up to 100 μm. This may be a consequence of the narrow space between MEW struts on the scaffold outer surface (space between struts=20 μm), which may limit the infiltration of larger vessels originating from the periosteal site. Although pores smaller than 400 μm have been generally associated with reduced vessel infiltration [46], among small sizes, 100-150 μm pores produced a denser vascular network *in vivo* than 25-50 μm pores [148]. Additionally, an increased vascular response was predicted from the periosteum as compared to the bone marrow, consistent with previous *in vivo* studies [5, 97]. Motivated by these considerations, a proof-of-concept simulation was carried out by increasing the vessel diameter to 40 μm. Model predictions showed increased vessel infiltration within the FDM scaffold as compared to MEW, aligning with experimental results, even though vessel densities were generally underestimated. Importantly, this reduced vascular ingrowth led to a slight

decrease in predicted bone formation within both scaffolds, but MEW still supported higher bone regeneration compared to FDM scaffolds, in line with the experiment [108]. These findings highlight the importance of carefully designing pore size to avoid restricting vessel infiltration, especially at the scaffold outer-surface.

Strut spacing and tissue deposition

To investigate the mechano-biological processes behind the increased bone formation within the MEW scaffold, key cellular activities were tracked throughout the bone healing simulation. Increased osteoblast proliferation and differentiation were observed over time within the MEW scaffolds, in line with the enhanced bone formation within this scaffold. Enhanced cell proliferation within MEW as compared to FDM scaffolds has already been observed during preliminary *in vitro* experiments by Eichholz and colleagues [108] and was associated with the higher porosity of the MEW scaffold, allowing a greater volume within which cells can proliferate, in line with other experimental studies [51]. Notably, the increased osteoblast differentiation within MEW contrasts with the larger volumes characterised by mechanical stimuli supporting bone formation in the FDM scaffold. Moreover, simulations revealed an asymmetric mechanical environment due to bending loads and the internal fixator, yet bone formation remained only mildly asymmetrical. These observations suggested that bone formation patterns within the two scaffold types cannot be explained by the mechanical environment alone. To assess whether scaffold architectural cues also affected the predicted higher osteoblast differentiation within the MEW scaffold, the percentage of MSCs unable to differentiate into osteoblasts, despite being exposed to the right mechanical stimuli, was quantified. This revealed that MSCs exhibited a lower differentiation within the FDM scaffold due to the difficulty in finding available surfaces for cell attachment. Such limitation may be due to the larger spacing between scaffold struts (higher pore size and lower surface-area-to-volume ratio), consistent with the experimental literature showing enhanced cell growth for shorter distances between scaffold inner surfaces [149]. A high surface area-to-volume ratio has been generally regarded as beneficial for bone regeneration, enhancing cell attachment [48] and supporting cell migration [50].

Limitations and future work

This study has a few limitations that need to be acknowledged. The computer model failed to replicate the increased vascularity observed experimentally within the FDM scaffolds if only small vessels (diameter of 20 μm) were included. Additional simulations incorporating an increased vessel diameter of 40 μm, better reflecting the presence of larger vessels observed experimentally within the FDM scaffolds, indicated that the reduced strut spacing on the outer surface of the MEW scaffold might explain experimental results. However, vessels are remodelled dynamically over time, and this process was not explicitly modelled. While blood flow, oxygenation and several signalling pathways are all thought to contribute to vessel remodelling during bone healing, the specific mechanobiological mechanisms regulating those processes have been largely overlooked and are still unknown [150-152]. As more experimental data become available, future work should extend the current model to incorporate aspects of vessel remodelling processes, such as a dynamic vessel diameter.

Although extracellular matrix (ECM) fibres play a key role in bone regeneration and angiogenesis by providing structural and directional cues for mineral deposition [153, 154] and vessel growth [24], their deposition was not explicitly simulated in the present model. Despite this, the model reproduced the morphology of the newly formed bone ends within the two scaffolds. In the case of FDM scaffolds, however, the predicted bone spicules appeared smaller compared to those observed experimentally. Previous research has attributed the formation of elongated bone spicules through large scaffold pores to a non-standard mineralisation mechanism driven by highly aligned collagen fibres [153]. Incorporating additional processes such as collagen fibre deposition and strain-induced remodelling could allow to improve the fidelity of the developed computational framework and better capture the formation of long bone cones within the FDM scaffold pores.

To reduce the computational cost of the simulation, the geometry of the FDM scaffold was slightly simplified. The original design featured struts with circular cross-sections, requiring over one million finite elements to be discretised and more than five hours to complete a single finite element analysis. Since the computational framework is iterative and involves 26 finite element analysis steps to cover the 12 weeks of healing, the setup was computationally expensive. To reduce the simulation time, adjacent overlapping struts were merged in pairs, forming single struts with oval cross-sections. This reduced the

simulation time by more than a factor of five. It is worth noting that the initial scaffold geometry is itself an idealisation of the actual printed structure.

This study analyses two scaffold architectures, printed through FDM and MEW, to investigate how mechanical cues and scaffold architectural features affect bone and vessel formation. These designs were chosen to replicate a specific *in vivo* experiment [108] and allowed model validation by comparing *in silico* and *in vivo* results. However, the developed computational framework is highly flexible, with mechanical and biological parameters easily adjustable to replicate various bone regeneration experimental conditions. Future work should validate the computer model across different scaffold designs to enrich and generalise the current findings.

6

Conclusions

6.1 Achievements and contributions to the field

Sprouting angiogenesis is a critical determinant for successful bone regeneration, yet its regulation remains poorly understood. Mechanical and structural cues, including physiological external loads, cell-generated traction forces and geometrical cues, likely influence angiogenesis after bone injury, however their individual contributions and interactions are not well known. To address this gap, I developed multiscale computer models replicating targeted experiments to investigate the mechano-regulation of angiogenesis during bone healing. The developed framework allowed to systematically investigate the effect of each individual factor, as well as their interactions, on the angiogenic process, thereby unravelling several mechanobiological principles behind angiogenesis during bone healing, as outlined below and summarised in Figure 6.1.

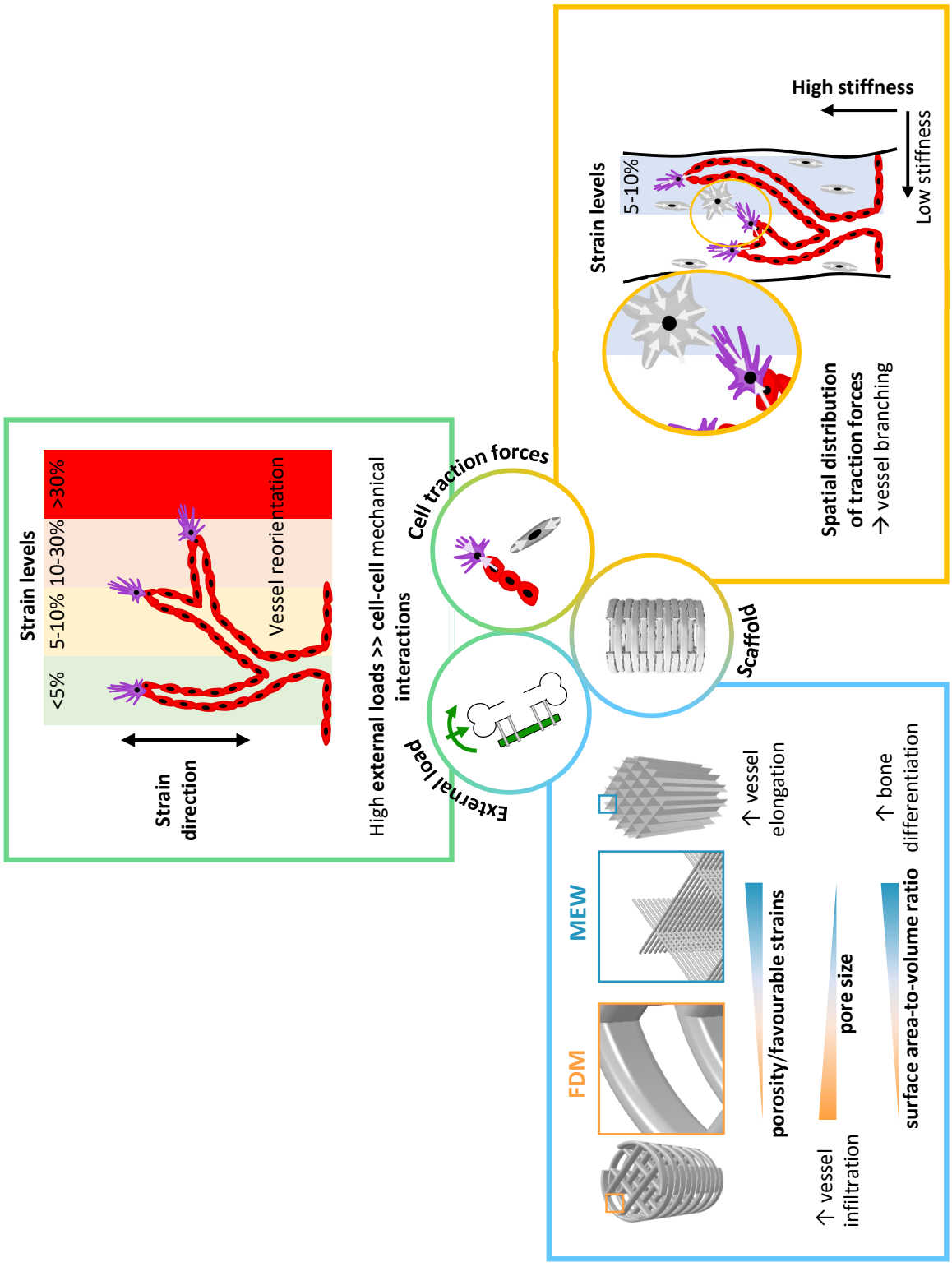

Figure 6.1: Graphical abstract. *The key findings of the thesis are illustrated. Colours indicate the three different Chapters (Chapter 3 in yellow, Chapter 4 in green, Chapter 5 in light blue) corresponding to the three objectives of the thesis.*

The first step of the thesis was the development of a computer model of the mechanical interplay between fibroblast and endothelial cells within a scaffold with highly aligned pores (Chapter 3). The computer model successfully replicated the vessel formation process

and fibroblast organisation observed *in vitro*. The comparison of simulation results with experimental data revealed that *durotaxis*, that is the cell preference for a stiffer environment, governed cell and vessel preferential alignment along the scaffold pores. Moreover, mechanical strain levels induced within the pore by cell-generated traction forces influenced vessel elongation, with strains between 5% and 10% boosting vessel growth. Besides cell traction force magnitude, cell morphology - and thus the spatial distribution of traction forces - was found to modulate vessel branching: forces acting orthogonal to the vessel body induced new sprouting events. However, it remained to be elucidated how cell-cell mechanical communication contributes to *in vivo* sprouting angiogenesis.

This was addressed in the second step of the thesis by extending the developed framework to simulate angiogenesis and stromal cell self-organisation during the early stages of bone healing (Chapter 4). The previously built computer model was expanded to account for the presence of external *in vivo*-like loading. The mechanobiological rules implemented in the model allowed to explain why microvascular networks established specific patterns in bone healing that comes to a fast and uneventful healing (rigid fixator) or delayed healing (semirigid fixator). Comparing predicted vessel patterns to experimental data revealed that principal strain magnitude and orientation, together with endothelial tip cell mechano-response, are essential for vessel organisation: at low strain levels, vessels align with the principal strain directions, whereas at high strain levels they reorient orthogonally, probably as a protective response to avoid damage. Regarding stromal cell self-organisation, *durotaxis* appeared to explain stromal cell patterns *in vivo* as well. Through *in silico* experiments, the different mechanical cues were isolated and *in vivo*-like external loads were found to overrule cell-cell mechanical interactions mediated by cell-generated traction forces.

Finally, a computer model of angiogenesis and bone regeneration during scaffold-aided bone healing was developed, specifically considering scaffolds fabricated by two different 3D printing techniques: FDM and MEW (Chapter 5). After model validation, the computer model was used to investigate the impact of scaffold architectural and mechanical cues on angiogenesis and bone regeneration. MEW high porosity induced mechanical strains within the range of those reported to foster vessel growth. However, the small pore size on the outer surface was found to prevent larger periosteal vessels from invading the scaffold over time. Moreover, architectural features such as small strut spacing and high surface-

area-to-volume ratio could explain the increased bone formation observed within MEW scaffolds, via enhanced osteoblast differentiation.

Beyond mechanobiological findings, this thesis presents a flexible computational framework that simulates angiogenesis across *in vitro* and *in vivo* contexts. This framework can be easily extended as new data become available and adapted to replicate specific experimental setups, thereby providing further insights into the mechanobiology of sprouting angiogenesis. The specific recommendations for the future steps are presented in the next section.

6.2 Recommendations for future work

Future work should address the limitations of this thesis. A recurrent limitation across all three studies is the lack of ECM fibre deposition and remodelling, which are key for cell and vessel organisation. Implementing this extension will require close collaboration with experimental teams. Time-resolved measurements of fibre organisation are needed to inform and validate the model, while dedicated mechanical tests are required to calibrate more advanced constitutive models (e.g. fibre-reinforced hyperelastic formulation). This would help capture experimental features that the current model failed to reproduce, such as the periosteal vessel alignment under semirigid fixator or the long bone spikes within FDM scaffold pores, and clarify how fibre contact guidance interacts with the mechanobiological rules identified in this thesis.

The angiogenesis model itself could be further complemented to improve its predictive power. Vessel remodelling is crucial for shaping the mature vascular network and was only indirectly represented. As more experimental data become available, future work should extend the current framework to incorporate aspects of vessel remodelling processes, such as a dynamic vessel diameter adaptation and regression rules driven by local oxygenation levels, VEGF concentration and shear stresses.

The mechanobiological principles identified in this thesis appeared consistent in murine long bones (mice and rats), however it remains to be assessed whether they extend to other bones and species. Future studies should test their transferability across species and bones, and, ultimately, in humans.

Future work should explore further scaffold and fixator designs. Systematic parametric studies varying pore size, orientation, porosity, surface area-to-volume ratio and material stiffness could quantify the contribution of each feature on angiogenesis and bone

regeneration. Building on that, multi-objective optimisation (e.g., optimising angiogenic infiltration and maximising bone formation) could identify the most promising scaffold architectures or fixators to test *in vivo*, thereby focusing experiments on the best candidates and reducing animal use.

Finally, developing a more integrated and user-friendly interface of the computer model would facilitate the adaptation of the model to the different scaffold and fixator designs as well as experimental settings.

A

Mesh convergence analyses

A.1 Fibrin gel within the anisotropic scaffold

A mesh convergence analysis of the fibrin gel within the collagen scaffold was performed to ensure that the predicted strain remained stable under mesh refinement. Three mesh sizes were investigated, with element sizes of 0.01 mm, 0.005 mm, and 0.0025 mm, corresponding to a constant refinement ratio of r=2. The analysis was restricted to the region of interest, i.e. the central pore of the scaffold. The analysis focused on the absolute principal strain values, since the mechanobiological model considers this quantity as the key stimulus for cell activity, independent of its sign.

The resulting distributions of principal strains within the pore appeared consistent across all three mesh sizes (Fig. A.1).

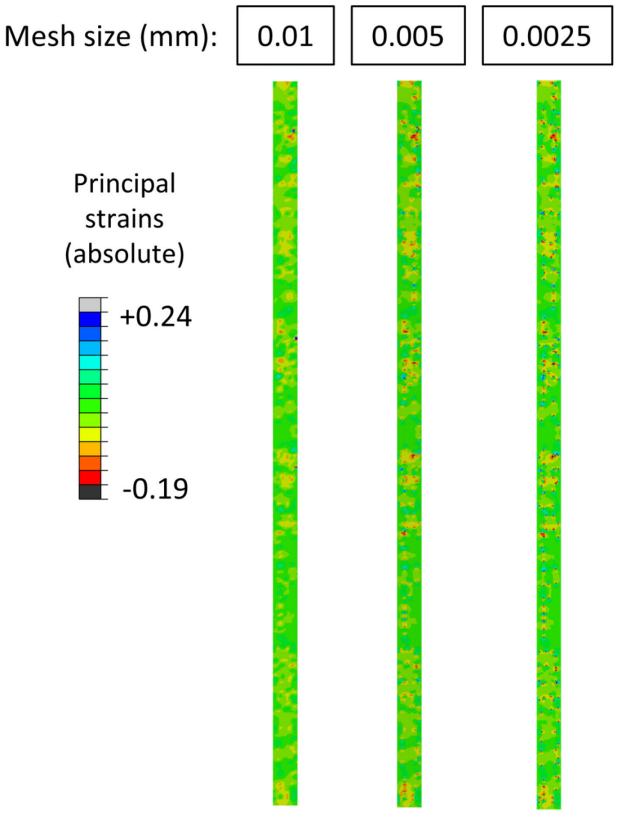

Figure A.1: Mesh convergence analysis of the fibrin gel. *Predicted distributions of the absolute principal strains within one pore of the anisotropic collagen scaffolds are shown for three mesh sizes: 0.01 mm, 0.005 mm and 0.0025 mm (from left to right).*

The absolute principal strain values obtained for each mesh refinement are reported in Table A.1. The difference between the coarsest (case 1) and the finest mesh (case 3) was 0.18%, while the computational run time was reduced by a factor of 20. Therefore, case 1 was assumed sufficiently accurate and adopted for subsequent simulations.

Case	Mesh size (mm)	Run time (s)	Principal strains (absolute)
1	0.01	4	0.0499
2	0.005	18	0.0509
3	0.0025	83	0.0500

Table A.1: Quantities of interest for the fibrin gel mesh convergence analysis. *For each case, scaffolds and callus mesh characteristic size, simulation run times and averaged absolute principal strain values within one pore.*

A.2 Callus and scaffolds

A mesh convergence analysis of the callus and both the FDM and MEW scaffolds was performed to evaluate whether the selected mesh sizes provided sufficient accuracy. The

coarsest mesh size was constrained by the FDM strut dimension (0.2 mm), while the finest mesh size was limited by the computational capacity of the server to handle models with several million elements. Accordingly, three mesh sizes were tested with a refinement ratio of approximately 1.4 between successive cases: 0.2 mm, 0.14 mm, and 0.1 mm. For each case, the same mesh size was assigned to both the callus and the scaffold. The resulting distributions of minimum principal strains appeared similar within the healing region cross-section for both scaffold types across mesh refinements (Fig. A.2).

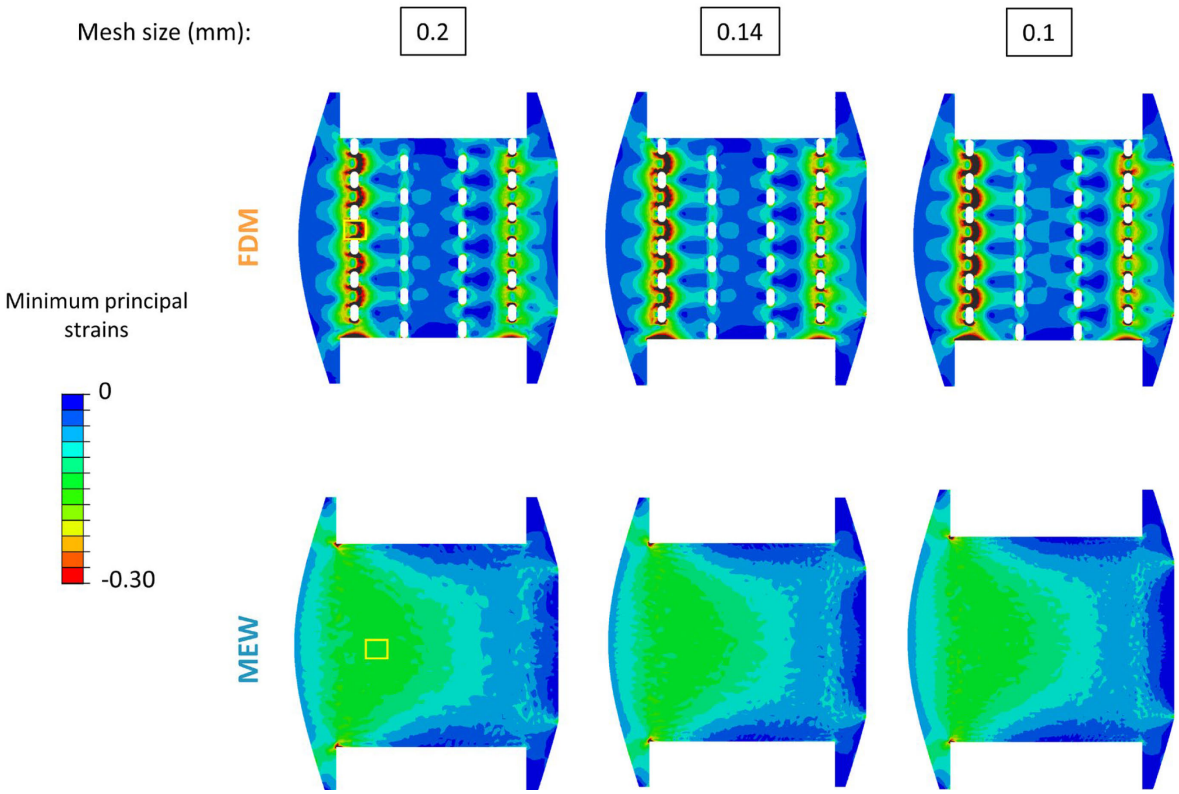

Figure A.2: Mesh convergence analysis of the callus and scaffolds. *Predicted distributions of the minimum principal strains within the healing region are shown for FDM (top) and MEW (bottom) scaffolds at three mesh sizes: 0.2 mm, 0.14 mm and 0.1 mm (from left to right). The yellow boxes indicate the location of the volumes of interest.*

To quantitatively assess the sensitivity of the predicted strains to mesh refinement, two volumes of interest were defined within scaffolds, corresponding to highly strained regions (Fig. A.2). In the FDM scaffold, this region was located between scaffold struts, whereas in the MEW scaffold, it was placed centrally on the left (non-fixator) side (Fig. A.2). Maximum and minimum principal strains computed at integration points were averaged within each volume of interest, and the corresponding values are reported in Table A.2.

For the FDM scaffold, a good agreement was observed across refinements, with a 3.4 % difference for the maximum principal strain and a 4.3 % difference for the minimum principal strain between the coarsest (case 1) and the finest mesh (case 3). Even greater

agreement was obtained for the MEW scaffold, with both strain measures deviating by less than 2% between the coarsest (case 1) and the finest mesh (case 3). On this basis, case 1 was considered sufficiently accurate for both the callus and scaffolds and was chosen for the simulations. This choice also reduced the computational cost by a factor of 10, which was essential since the finite element analysis had to be repeated multiple times within each bone regeneration simulation.

		FDM			MEW		
Case	Mesh size (mm)	Run time (s)	Maximum principal strain	Minimum principal strain	Run time (s)	Maximum principal strain	Minimum principal strain
1	0.2	304	0.2258	-0.2795	199	0.0957	-0.1361
2	0.14	623	0.2250	-0.2800	635	0.0946	-0.1353
3	0.1	2961	0.2338	-0.2920	2020	0.0939	-0.1357

Table A.2: Quantities of interest for the callus and scaffolds mesh convergence analysis. *For each case, scaffolds and callus mesh characteristic size, simulation run times and averaged principal strain values in a volume of highly strained elements (depicted in Figure A.2).*

B

Angiogenesis model calibration

B.1 Identification of traction force configuration

Tip ECs are known to exert traction forces on the surrounding environment, however their spatial configuration remains unclear. Traction force microscopy experiments [13] suggested that the sprout tip exerts radially distributed traction forces, whereas the entire sprout behaves as a force dipole. However, most of these studies investigated a single tip cell sprouting off from a cluster of ECs, which does not allow to separate the displacement field from the traction exerted by the spheroid at the sprout base.

To realistically reproduce traction forces generated by an angiogenic sprout, preliminary simulations were performed and compared with data from a 3D traction force microscopy experiment on a longer sprout (2-3 cells). A simplified 2D FE model of a growing sprout onto a gelatin substrate was developed and two different configurations of traction force configurations were tested: the tip cell acting as an active force dipole with traction forces aligned to the vessel growth direction, or exerting radially distributed forces on the substrate (Fig. B.1 a). Stalk cells were hypothesised not to contribute, in agreement with previous studies [155, 156].

The predicted displacement field generated by the sprout contractile activity was qualitatively compared with experimental data (Fig. B.1 b). The dipole configuration produced displacement vectors that more closely resembled the experimentally observed polarisation, and was therefore adopted in the simulations presented in this thesis.

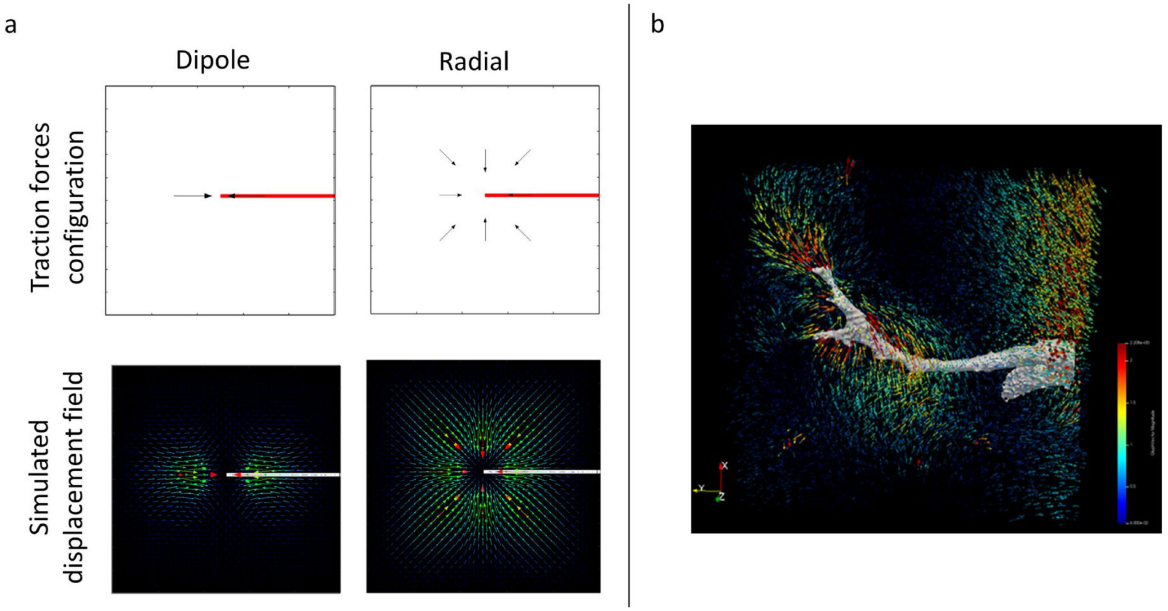

Figure B.1: Simulated vs. experimental displacement field around the sprout. *(a) Traction force configurations assigned to the sprout tip and the corresponding predicted displacement fields. (b) Displacement field obtained from 3D traction force microscopy experiments.*

B.2 Parameter sweep analysis for vessel growth direction

A parameter sweep analysis was carried out to identify the combination of probabilities governing tip ECs growth direction (P1=persistency, P2=randomness, P3=mechanics) that best reproduced the experimentally observed vessel orientation distribution during early bone healing. All three regions of interest were considered: the gap (ROI1), the bone marrow (ROI2), and the periosteal site (ROI3). Constraints were imposed to identify the relevant parameter combinations, which are reported in Table B.1:

P1+P2+P3 = 1;

P1, P2, P3 >= 0.2 in order to have a sufficient contribution of each parameter;

P2 < 0.6 since vessels resulted unrealistically short as compared to the histological images with P2 ≥ 0.6.

The analysis was performed for both the rigid and the semirigid fixation scenarios.

	1	**2**	**3**	**4**	**5**	**6**	**7**	**8**	**9**	**10**	**11**	**12**	**13**	**14**
P1	0.3	0.4	0.5	0.6	0.2	0.3	0.4	0.5	0.2	0.3	0.4	0.2	0.3	0.2
P2	0.5	0.4	0.3	0.2	0.5	0.4	0.3	0.2	0.4	0.3	0.2	0.3	0.2	0.2
P3	0.2	0.2	0.2	0.2	0.3	0.3	0.3	0.3	0.4	0.4	0.4	0.5	0.5	0.6

Table B.1: Parameter sets analysed. *Considered parameter combinations (P1, P2, P3) and corresponding model numbers.*

All parameter combinations reproduced the experimentally observed preferential vessel alignment within the different ROIs, with the exception of ROI 3 under semirigid fixator, which failed across all the parameter combinations and was therefore excluded from this analysis (Fig. B.2). The reasons for this discrepancy are discussed in Section 4.6 (Limitations and future work).

Figure B.2: Vessel orientation analysis. *Results for all probability value combinations (P1, P2, P3) across the three regions of interest for both fixators.*

To identify the optimal combination of probability values, the Mean Squared Error (MSE) between the computational and experimental vessel orientation distributions was computed within each ROI. For every parameter combination, the MSE values from all ROIs and both fixators were summed to obtain a Total MSE (Fig. B.3). The parameter set resulting in the lowest Total MSE corresponded to P1=0.4, P2=0.4, P3=0.2; therefore, it was adopted in the computer model.

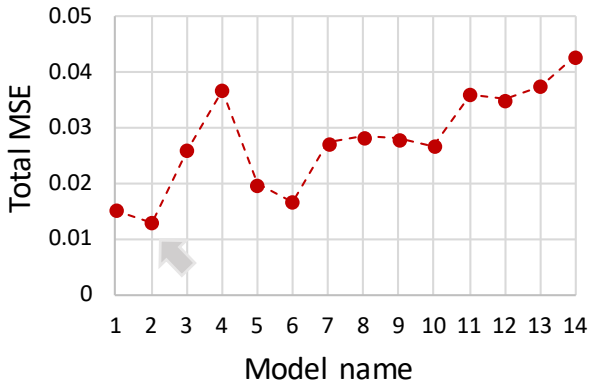

Figure B.3: Total MSE. *Total MSE values for each parameter combination, with the minimum indicated by the grey arrow.*

References

[1] J.M. Kanczler, R.O. Oreffo, Osteogenesis and angiogenesis: the potential for engineering bone, Eur Cell Mater 15 (2008) 100-14.
[2] M.R. Hausman, M.B. Schaffler, R.J. Majeska, Prevention of fracture healing in rats by an inhibitor of angiogenesis, Bone 29(6) (2001) 560-4.
[3] H.C. Brownlow, A. Reed, A.H. Simpson, The vascularity of atrophic non-unions, Injury 33(2) (2002) 145-50.
[4] K.F. Dickson, S. Katzman, G. Paiement, The importance of the blood supply in the healing of tibial fractures, Contemp Orthop 30(6) (1995) 489-93.
[5] L.C. Gerstenfeld, D.M. Cullinane, G.L. Barnes, D.T. Graves, T.A. Einhorn, Fracture healing as a post-natal developmental process: molecular, spatial, and temporal aspects of its regulation, J Cell Biochem 88(5) (2003) 873-84.
[6] K. Schmidt-Bleek, A. Petersen, A. Dienelt, C. Schwarz, G.N. Duda, Initiation and early control of tissue regeneration – bone healing as a model system for tissue regeneration, Expert Opinion on Biological Therapy 14(2) (2014) 247-259.
[7] G.N. Duda, S. Geissler, S. Checa, S. Tsitsilonis, A. Petersen, K. Schmidt-Bleek, The decisive early phase of bone regeneration, Nature Reviews Rheumatology 19(2) (2023) 78-95.
[8] P. Carmeliet, F. De Smet, S. Loges, M. Mazzone, Branching morphogenesis and antiangiogenesis candidates: tip cells lead the way, Nat Rev Clin Oncol 6(6) (2009) 315-26.
[9] M. Kretschmer, D. Rudiger, S. Zahler, Mechanical Aspects of Angiogenesis, Cancers (Basel) 13(19) (2021).
[10] C.A. Dessalles, C. Leclech, A. Castagnino, A.I. Barakat, Integration of substrate- and flow-derived stresses in endothelial cell mechanobiology, Communications Biology 4(1) (2021) 764.
[11] S. Barrasa-Ramos, C.A. Dessalles, M. Hautefeuille, A.I. Barakat, Mechanical regulation of the early stages of angiogenesis, J R Soc Interface 19(197) (2022) 20220360.
[12] M. Manetti, Molecular Morphology and Function of Stromal Cells, Int J Mol Sci 22(24) (2021) 13422.
[13] M.M. Vaeyens, A. Jorge-Penas, J. Barrasa-Fano, C. Steuwe, T. Heck, P. Carmeliet, M. Roeffaers, H. Van Oosterwyck, Matrix deformations around angiogenic sprouts correlate to sprout dynamics and suggest pulling activity, Angiogenesis 23(3) (2020) 315-324.
[14] J.R. Lange, B. Fabry, Cell and tissue mechanics in cell migration, Experimental Cell Research 319(16) (2013) 2418-2423.
[15] B.E. Sumpio, A.J. Banes, L.G. Levin, G. Johnson, Jr., Mechanical stress stimulates aortic endothelial cells to proliferate, J Vasc Surg 6(3) (1987) 252-6.
[16] X.-m. Liu, D. Ensenat, H. Wang, A.I. Schafer, W. Durante, Physiologic cyclic stretch inhibits apoptosis in vascular endothelium, FEBS Letters 541(1-3) (2003) 52-56.
[17] W. Li, B.E. Sumpio, Strain-induced vascular endothelial cell proliferation requires PI3K-dependent mTOR-4E-BP1 signal pathway, Am J Physiol Heart Circ Physiol 288(4) (2005) H1591-7.
[18] B. Kou, J. Zhang, D.R. Singer, Effects of cyclic strain on endothelial cell apoptosis and tubulogenesis are dependent on ROS production via NAD(P)H subunit p22phox, Microvasc Res 77(2) (2009) 125-33.

[19] J.H. Wang, P. Goldschmidt-Clermont, J. Wille, F.C. Yin, Specificity of endothelial cell reorientation in response to cyclic mechanical stretching, J Biomech 34(12) (2001) 1563-72.
[20] M. Moretti, A. Prina-Mello, A.J. Reid, V. Barron, P.J. Prendergast, Endothelial cell alignment on cyclically-stretched silicone surfaces, J Mater Sci Mater Med 15(10) (2004) 1159-64.
[21] I.S. Joung, M.N. Iwamoto, Y.T. Shiu, C.T. Quam, Cyclic strain modulates tubulogenesis of endothelial cells in a 3D tissue culture model, Microvasc Res 71(1) (2006) 1-11.
[22] J.R. Wilkins, D.B. Pike, C.C. Gibson, L. Li, Y.T. Shiu, The interplay of cyclic stretch and vascular endothelial growth factor in regulating the initial steps for angiogenesis, Biotechnol Prog 31(1) (2015) 248-57.
[23] S. Wong, W.H. Guo, Y.L. Wang, Fibroblasts probe substrate rigidity with filopodia extensions before occupying an area, Proc Natl Acad Sci U S A 111(48) (2014) 17176-81.
[24] C.D. Davidson, W.Y. Wang, I. Zaimi, D.K.P. Jayco, B.M. Baker, Cell force-mediated matrix reorganization underlies multicellular network assembly, Sci Rep 9(1) (2019) 12.
[25] T. Kaully, K. Kaufman-Francis, A. Lesman, S. Levenberg, Vascularization--the conduit to viable engineered tissues, Tissue Eng Part B Rev 15(2) (2009) 159-69.
[26] D. Rosenfeld, S. Landau, Y. Shandalov, N. Raindel, A. Freiman, E. Shor, Y. Blinder, H.H. Vandenburgh, D.J. Mooney, S. Levenberg, Morphogenesis of 3D vascular networks is regulated by tensile forces, Proc Natl Acad Sci U S A 113(12) (2016) 3215-20.
[27] M.K. Sewell-Loftin, J.B. Katz, S.C. George, G.D. Longmore, Micro-strains in the extracellular matrix induce angiogenesis, Lab on a Chip 20(15) (2020) 2776-2787.
[28] E. Roddy, M.R. DeBaun, A. Daoud-Gray, Y.P. Yang, M.J. Gardner, Treatment of critical-sized bone defects: clinical and tissue engineering perspectives, European Journal of Orthopaedic Surgery & Traumatology 28(3) (2018) 351-362.
[29] C. Schlundt, C.H. Bucher, S. Tsitsilonis, H. Schell, G.N. Duda, K. Schmidt-Bleek, Clinical and Research Approaches to Treat Non-union Fracture, Current Osteoporosis Reports 16(2) (2018) 155-168.
[30] J.A. Cobos, R.W. Lindsey, Z. Gugala, The Cylindrical Titanium Mesh Cage for Treatment of a Long Bone Segmental Defect: Description of a New Technique and Report of Two Cases, Journal of Orthopaedic Trauma 14(1) (2000).
[31] J.C. Reichert, A. Cipitria, D.R. Epari, S. Saifzadeh, P. Krishnakanth, A. Berner, M.A. Woodruff, H. Schell, M. Mehta, M.A. Schuetz, G.N. Duda, D.W. Hutmacher, A Tissue Engineering Solution for Segmental Defect Regeneration in Load-Bearing Long Bones, Science Translational Medicine 4(141) (2012) 141ra93-141ra93.
[32] F.A. Shah, O. Omar, F. Suska, A. Snis, A. Matic, L. Emanuelsson, B. Norlindh, J. Lausmaa, P. Thomsen, A. Palmquist, Long-term osseointegration of 3D printed CoCr constructs with an interconnected open-pore architecture prepared by electron beam melting, Acta Biomaterialia 36 (2016) 296-309.
[33] A.M. Crovace, L. Lacitignola, D.M. Forleo, F. Staffieri, E. Francioso, A. Di Meo, J. Becerra, A. Crovace, L. Santos-Ruiz, 3D Biomimetic Porous Titanium (Ti6Al4V ELI) Scaffolds for Large Bone Critical Defect Reconstruction: An Experimental Study in Sheep, Animals, 2020.
[34] A.-M. Pobloth, S. Checa, H. Razi, A. Petersen, J.C. Weaver, K. Schmidt-Bleek, M. Windolf, A.Á. Tatai, C.P. Roth, K.-D. Schaser, G.N. Duda, P. Schwabe, Mechanobiologically optimized 3D titanium-mesh scaffolds enhance bone regeneration in critical segmental defects in sheep, Science Translational Medicine 10(423) (2018) eaam8828.
[35] F.E. Freeman, D.C. Browe, J. Nulty, S. Von Euw, W.L. Grayson, D.J. Kelly, Biofabrication of multiscale bone extracellular matrix scaffolds for bone tissue engineering, Eur Cell Mater 38 (2019) 168-187.
[36] K.F. Eichholz, P. Pitacco, R. Burdis, F. Chariyev-Prinz, X. Barceló, B. Tornifoglio, R. Paetzold, O. Garcia, D.J. Kelly, Integrating Melt Electrowriting and Fused Deposition

Modeling to Fabricate Hybrid Scaffolds Supportive of Accelerated Bone Regeneration, Advanced Healthcare Materials 13(3) (2024) 2302057.
[37] N. Abbasi, R.S.B. Lee, S. Ivanovski, R.M. Love, S. Hamlet, In vivo bone regeneration assessment of offset and gradient melt electrowritten (MEW) PCL scaffolds, Biomaterials Research 24(1) 17.
[38] A.A. Zadpoor, Bone tissue regeneration: the role of scaffold geometry, Biomaterials Science 3(2) (2015) 231-245.
[39] S. Yin, W. Zhang, Z. Zhang, X. Jiang, Recent Advances in Scaffold Design and Material for Vascularized Tissue-Engineered Bone Regeneration, Adv Healthc Mater 8(10) (2019) e1801433.
[40] A.R. Amini, D.J. Adams, C.T. Laurencin, S.P. Nukavarapu, Optimally porous and biomechanically compatible scaffolds for large-area bone regeneration, Tissue Eng Part A 18(13-14) (2012) 1376-88.
[41] C.M. Murphy, M.G. Haugh, F.J. O'Brien, The effect of mean pore size on cell attachment, proliferation and migration in collagen-glycosaminoglycan scaffolds for bone tissue engineering, Biomaterials 31(3) (2010) 461-6.
[42] L.G. Sicchieri, G.E. Crippa, P.T. de Oliveira, M.M. Beloti, A.L. Rosa, Pore size regulates cell and tissue interactions with PLGA–CaP scaffolds used for bone engineering, Journal of Tissue Engineering and Regenerative Medicine 6(2) (2012) 155-162.
[43] C. Wu, Y. Zhang, Y. Zhu, T. Friis, Y. Xiao, Structure–property relationships of silk-modified mesoporous bioglass scaffolds, Biomaterials 31(13) (2010) 3429-3438.
[44] Y. Zhang, W. Fan, Z. Ma, C. Wu, W. Fang, G. Liu, Y. Xiao, The effects of pore architecture in silk fibroin scaffolds on the growth and differentiation of mesenchymal stem cells expressing BMP7, Acta Biomaterialia 6(8) (2010) 3021-3028.
[45] C. Correia, S. Bhumiratana, L.-P. Yan, A.L. Oliveira, J.M. Gimble, D. Rockwood, D.L. Kaplan, R.A. Sousa, R.L. Reis, G. Vunjak-Novakovic, Development of silk-based scaffolds for tissue engineering of bone from human adipose-derived stem cells, Acta Biomaterialia 8(7) (2012) 2483-2492.
[46] B. Feng, Z. Jinkang, W. Zhen, L. Jianxi, C. Jiang, L. Jian, M. Guolin, D. Xin, The effect of pore size on tissue ingrowth and neovascularization in porous bioceramics of controlled architecture in vivo, Biomed Mater 6(1) (2011) 015007.
[47] N. Abbasi, A. Abdal-hay, S. Hamlet, E. Graham, S. Ivanovski, Effects of Gradient and Offset Architectures on the Mechanical and Biological Properties of 3-D Melt Electrowritten (MEW) Scaffolds, ACS Biomaterials Science & Engineering 5(7) (2019) 3448-3461.
[48] F.J. O'Brien, B.A. Harley, I.V. Yannas, L.J. Gibson, The effect of pore size on cell adhesion in collagen-GAG scaffolds, Biomaterials 26(4) (2005) 433-441.
[49] T.D. Nguyen, O.E. Kadri, V.I. Sikavitsas, R.S. Voronov, Scaffolds with a High Surface Area-to-Volume Ratio and Cultured Under Fast Flow Perfusion Result in Optimal O2 Delivery to the Cells in Artificial Bone Tissues, Applied Sciences, 2019.
[50] J. Jiao, Q. Hong, D. Zhang, M. Wang, H. Tang, J. Yang, X. Qu, B. Yue, Influence of porosity on osteogenesis, bone growth and osteointegration in trabecular tantalum scaffolds fabricated by additive manufacturing, Frontiers in Bioengineering and Biotechnology Volume 11 - 2023 (2023).
[51] J. Jiao, Q. Hong, D. Zhang, M. Wang, H. Tang, J. Yang, X. Qu, B. Yue, Influence of porosity on osteogenesis, bone growth and osteointegration in trabecular tantalum scaffolds fabricated by additive manufacturing, Front Bioeng Biotechnol 11 (2023) 1117954.
[52] P. Xia, Y. Luo, Vascularization in tissue engineering: The architecture cues of pores in scaffolds, Journal of Biomedical Materials Research Part B: Applied Biomaterials 110(5) (2022) 1206-1214.
[53] L.A. Liotta, G.M. Saidel, J. Kleinerman, Diffusion model of tumor vascularization and growth, Bulletin of Mathematical Biology 39(1) (1977) 117-128.

[54] S.M. Peirce, Computational and mathematical modeling of angiogenesis, Microcirculation 15(8) (2008) 739-51.
[55] A.A. Qutub, F.M. Gabhann, E.D. Karagiannis, P. Vempati, A.S. Popel, Multiscale models of angiogenesis, IEEE Engineering in Medicine and Biology Magazine 28(2) (2009) 14-31.
[56] C. Kuhn, S. Checa, Computational Modeling to Quantify the Contributions of VEGFR1, VEGFR2, and Lateral Inhibition in Sprouting Angiogenesis, Front Physiol 10 (2019) 288.
[57] K. Bentley, H. Gerhardt, P.A. Bates, Agent-based simulation of notch-mediated tip cell selection in angiogenic sprout initialisation, J Theor Biol 250(1) (2008) 25-36.
[58] K. Bentley, G. Mariggi, H. Gerhardt, P.A. Bates, Tipping the balance: robustness of tip cell selection, migration and fusion in angiogenesis, PLoS Comput Biol 5(10) (2009) e1000549.
[59] P. Santos-Oliveira, A. Correia, T. Rodrigues, T.M. Ribeiro-Rodrigues, P. Matafome, J.C. Rodriguez-Manzaneque, R. Seica, H. Girao, R.D. Travasso, The Force at the Tip--Modelling Tension and Proliferation in Sprouting Angiogenesis, PLoS Comput Biol 11(8) (2015) e1004436.
[60] A. Stéphanou, S. Le Floc'h, A. Chauvière, A Hybrid Model to Test the Importance of Mechanical Cues Driving Cell Migration in Angiogenesis, Math. Model. Nat. Phenom. 10(1) (2015) 142-166.
[61] R.F. van Oers, E.G. Rens, D.J. LaValley, C.A. Reinhart-King, R.M. Merks, Mechanical cell-matrix feedback explains pairwise and collective endothelial cell behavior in vitro, PLoS Comput Biol 10(8) (2014) e1003774.
[62] L.T. Edgar, S.A. Maas, J.E. Guilkey, J.A. Weiss, A coupled model of neovessel growth and matrix mechanics describes and predicts angiogenesis in vitro, Biomechanics and Modeling in Mechanobiology 14(4) (2015) 767-782.
[63] D. Burke, D.J. Kelly, A mechanobiological model of endothelial cell migration and proliferation, Comput Methods Biomech Biomed Engin 19(1) (2016) 74-83.
[64] A.L. Bauer, T.L. Jackson, Y. Jiang, Topography of extracellular matrix mediates vascular morphogenesis and migration speeds in angiogenesis, PLoS Comput Biol 5(7) (2009) e1000445.
[65] A.L. Bauer, T.L. Jackson, Y. Jiang, A cell-based model exhibiting branching and anastomosis during tumor-induced angiogenesis, Biophys J 92(9) (2007) 3105-21.
[66] L.T. Edgar, S.C. Sibole, C.J. Underwood, J.E. Guilkey, J.A. Weiss, A computational model of in vitro angiogenesis based on extracellular matrix fibre orientation, Comput Methods Biomech Biomed Engin 16(7) (2013) 790-801.
[67] A. Carlier, L. Geris, K. Bentley, G. Carmeliet, P. Carmeliet, H. Van Oosterwyck, MOSAIC: a multiscale model of osteogenesis and sprouting angiogenesis with lateral inhibition of endothelial cells, PLoS Comput Biol 8(10) (2012) e1002724.
[68] L. Geris, A. Gerisch, J.V. Sloten, R. Weiner, H.V. Oosterwyck, Angiogenesis in bone fracture healing: a bioregulatory model, J Theor Biol 251(1) (2008) 137-58.
[69] J.J. Kendall, C. Ledoux, F.C. Marques, D. Boaretti, F.A. Schulte, E.F. Morgan, R. Müller, An in silico micro-multiphysics agent-based approach for simulating bone regeneration in a mouse femur defect model, Frontiers in Bioengineering and Biotechnology 11 (2023).
[70] S. Checa, P.J. Prendergast, A mechanobiological model for tissue differentiation that includes angiogenesis: a lattice-based modeling approach, Ann Biomed Eng 37(1) (2009) 129-45.
[71] A. OReilly, K.D. Hankenson, D.J. Kelly, A computational model to explore the role of angiogenic impairment on endochondral ossification during fracture healing, Biomech Model Mechanobiol 15(5) (2016) 1279-94.

[72] H. Mehdizadeh, S. Sumo, E.S. Bayrak, E.M. Brey, A. Cinar, Three-dimensional modeling of angiogenesis in porous biomaterial scaffolds, Biomaterials 34(12) (2013) 2875-87.
[73] H. Mehdizadeh, E.S. Bayrak, C. Lu, S.I. Somo, B. Akar, E.M. Brey, A. Cinar, Agent-based modeling of porous scaffold degradation and vascularization: Optimal scaffold design based on architecture and degradation dynamics, Acta Biomater 27 (2015) 167-178.
[74] X. Sun, Y. Kang, J. Bao, Y. Zhang, Y. Yang, X. Zhou, Modeling vascularized bone regeneration within a porous biodegradable CaP scaffold loaded with growth factors, Biomaterials 34(21) (2013) 4971-81.
[75] S. Checa, P.J. Prendergast, Effect of cell seeding and mechanical loading on vascularization and tissue formation inside a scaffold: a mechano-biological model using a lattice approach to simulate cell activity, J Biomech 43(5) (2010) 961-8.
[76] C. Sandino, S. Checa, P.J. Prendergast, D. Lacroix, Simulation of angiogenesis and cell differentiation in a CaP scaffold subjected to compressive strains using a lattice modeling approach, Biomaterials 31(8) (2010) 2446-52.
[77] L. Wang, Q. Shi, Y. Cai, Q. Chen, X. Guo, Z. Li, Mechanical-chemical coupled modeling of bone regeneration within a biodegradable polymer scaffold loaded with VEGF, Biomech Model Mechanobiol 19(6) (2020) 2285-2306.
[78] U.S. Schwarz, S.A. Safran, Elastic interactions of cells, Phys Rev Lett 88(4) (2002) 048102.
[79] W.M. Petroll, Dynamic assessment of cell-matrix mechanical interactions in three-dimensional culture, Methods Mol Biol 370 (2007) 67-82.
[80] S. Checa, M.K. Rausch, A. Petersen, E. Kuhl, G.N. Duda, The emergence of extracellular matrix mechanics and cell traction forces as important regulators of cellular self-organization, Biomech Model Mechanobiol 14(1) (2015) 1-13.
[81] P.J. Prendergast, R. Huiskes, K. Søballe, Biophysical stimuli on cells during tissue differentiation at implant interfaces, Journal of Biomechanics 30(6) (1997) 539-548.
[82] F. De Smet, I. Segura, K. De Bock, P.J. Hohensinner, P. Carmeliet, Mechanisms of Vessel Branching, Arteriosclerosis, Thrombosis, and Vascular Biology 29(5) (2009) 639-649.
[83] J. Kleinheinz, U. Stratmann, U. Joos, H.-P. Wiesmann, VEGF-Activated Angiogenesis During Bone Regeneration, Journal of Oral and Maxillofacial Surgery 63(9) (2005) 1310-1316.
[84] E. Brauer, E. Lippens, O. Klein, G. Nebrich, S. Schreivogel, G. Korus, G.N. Duda, A. Petersen, Collagen Fibrils Mechanically Contribute to Tissue Contraction in an In Vitro Wound Healing Scenario, Adv Sci (Weinh) 6(9) (2019) 1801780.
[85] A. Herrera, J. Hellwig, H. Leemhuis, R. von Klitzing, I. Heschel, G.N. Duda, A. Petersen, From macroscopic mechanics to cell-effective stiffness within highly aligned macroporous collagen scaffolds, Mater Sci Eng C Mater Biol Appl 103 (2019) 109760.
[86] H. Duong, B. Wu, B. Tawil, Modulation of 3D fibrin matrix stiffness by intrinsic fibrinogen-thrombin compositions and by extrinsic cellular activity, Tissue Eng Part A 15(7) (2009) 1865-76.
[87] S.C. Schwager, F. Bordeleau, J. Zhang, M.A. Antonyak, R.A. Cerione, C.A. Reinhart-King, Matrix stiffness regulates microvesicle-induced fibroblast activation, Am J Physiol Cell Physiol 317(1) (2019) C82-c92.
[88] M. Tortorici, E. Brauer, M. Thiele, G.N. Duda, A. Petersen, Characterizing cell recruitment into isotropic and anisotropic biomaterials by quantification of spatial density gradients in vitro, Frontiers in Bioengineering and Biotechnology 10 (2022).
[89] M.A. Ruehle, E.A. Eastburn, S.A. LaBelle, L. Krishnan, J.A. Weiss, J.D. Boerckel, L.B. Wood, R.E. Guldberg, N.J. Willett, Extracellular matrix compression temporally regulates microvascular angiogenesis, Sci Adv 6(34) (2020).
[90] C. Dazzi, J. Mehl, M. Benamar, H. Gerhardt, P. Knaus, G.N. Duda, S. Checa, External mechanical loading overrules cell-cell mechanical communication in sprouting

angiogenesis during early bone regeneration, PLOS Computational Biology 19(11) (2023) e1011647.
[91] J. Mehl, S. Farahani, E. Brauer, A. Klaus-Bergmann, T. Thiele, A. Ellinghaus, E. Bartels-Klein, K. Koch, K. Schmidt-Bleek, A. Petersen, H. Gerhardt, V. Vogel, G. Duda, External Mechanical Stability Regulates Hematoma Vascularization in Bone Healing Rather than Endothelial YAP/TAZ Mechanotransduction, Advanced Science 11 (2024).
[92] E. Borgiani, C. Figge, B. Kruck, B.M. Willie, G.N. Duda, S. Checa, Age-Related Changes in the Mechanical Regulation of Bone Healing Are Explained by Altered Cellular Mechanoresponse, J Bone Miner Res 34(10) (2019) 1923-1937.
[93] S. Checa, P.J. Prendergast, G.N. Duda, Inter-species investigation of the mechano-regulation of bone healing: comparison of secondary bone healing in sheep and rat, J Biomech 44(7) (2011) 1237-45.
[94] J.P. Califano, C.A. Reinhart-King, Substrate Stiffness and Cell Area Predict Cellular Traction Stresses in Single Cells and Cells in Contact, Cell Mol Bioeng 3(1) (2010) 68-75.
[95] T.A. Alcoser, F. Bordeleau, S.P. Carey, M.C. Lampi, D.R. Kowal, S. Somasegar, S. Varma, S.J. Shin, C.A. Reinhart-King, Probing the biophysical properties of primary breast tumor-derived fibroblasts, Cell Mol Bioeng 8(1) (2015) 76-85.
[96] B. Kruck, E.A. Zimmermann, S. Damerow, C. Figge, C. Julien, D. Wulsten, T. Thiele, M. Martin, R. Hamdy, M.K. Reumann, G.N. Duda, S. Checa, B.M. Willie, Sclerostin Neutralizing Antibody Treatment Enhances Bone Formation but Does Not Rescue Mechanically Induced Delayed Healing, J Bone Miner Res 33(9) (2018) 1686-1697.
[97] J.D. Boerckel, B.A. Uhrig, N.J. Willett, N. Huebsch, R.E. Guldberg, Mechanical regulation of vascular growth and tissue regeneration in vivo, Proc Natl Acad Sci U S A 108(37) (2011) E674-80.
[98] R.N. Brueton, M. Brookes, F.W. Heatley, The vascular repair of an experimental osteotomy held in an external fixator, Clin Orthop Relat Res (257) (1990) 286-304.
[99] J. Stefanowski, A. Lang, A. Rauch, L. Aulich, M. Kohler, A.F. Fiedler, F. Buttgereit, K. Schmidt-Bleek, G.N. Duda, T. Gaber, R.A. Niesner, A.E. Hauser, Spatial Distribution of Macrophages During Callus Formation and Maturation Reveals Close Crosstalk Between Macrophages and Newly Forming Vessels, Front Immunol 10 (2019) 2588.
[100] W. Fan, R. Crawford, Y. Xiao, Structural and cellular differences between metaphyseal and diaphyseal periosteum in different aged rats, Bone 42(1) (2008) 81-9.
[101] H. Isaksson, C.C. van Donkelaar, R. Huiskes, K. Ito, A mechano-regulatory bone-healing model incorporating cell-phenotype specific activity, Journal of Theoretical Biology 252(2) (2008) 230-246.
[102] P.A. Appeddu, B.D. Shur, Molecular analysis of cell surface beta-1,4-galactosyltransferase function during cell migration, Proceedings of the National Academy of Sciences 91(6) (1994) 2095-2099.
[103] B.M. Kenyon, E.E. Voest, C.C. Chen, E. Flynn, J. Folkman, R.J. D'Amato, A model of angiogenesis in the mouse cornea, Investigative Ophthalmology & Visual Science 37(8) (1996) 1625-1632.
[104] L.E. Claes, N. Meyers, The direction of tissue strain affects the neovascularization in the fracture-healing zone, Med Hypotheses 137 (2020) 109537.
[105] L.E. Claes, C.A. Heigele, Magnitudes of local stress and strain along bony surfaces predict the course and type of fracture healing, J Biomech 32(3) (1999) 255-66.
[106] P.C. Dartsch, E. Betz, Response of cultured endothelial cells to mechanical stimulation, Basic Research in Cardiology 84(3) (1989) 268-281.
[107] M.H. Elfarnawany, Signal Processing Methods for Quantitative Power Doppler Microvascular Angiography, Electronic Thesis and Dissertation Repository, 2015.

[108] K.F. Eichholz, F.E. Freeman, P. Pitacco, J. Nulty, D. Ahern, R. Burdis, D.C. Browe, O. Garcia, D.A. Hoey, D.J. Kelly, Scaffold microarchitecture regulates angiogenesis and the regeneration of large bone defects, Biofabrication 14(4) (2022) 045013.
[109] C. Perier-Metz, A. Cipitria, D.W. Hutmacher, G.N. Duda, S. Checa, An in silico model predicts the impact of scaffold design in large bone defect regeneration, Acta Biomaterialia 145 (2022) 329-341.
[110] C. Schwarz, D. Wulsten, A. Ellinghaus, J. Lienau, B.M. Willie, G.N. Duda, Mechanical load modulates the stimulatory effect of BMP2 in a rat nonunion model, Tissue Eng Part A 19(1-2) (2013) 247-54.
[111] D. Lacroix, P.J. Prendergast, G. Li, D. Marsh, Biomechanical model to simulate tissue differentiation and bone regeneration: Application to fracture healing, Medical and Biological Engineering and Computing 40(1) (2002) 14-21.
[112] D. Lacroix, P.J. Prendergast, A mechano-regulation model for tissue differentiation during fracture healing: analysis of gap size and loading, Journal of Biomechanics 35(9) (2002) 1163-1171.
[113] C.G. Pitt, F.I. Chasalow, Y.M. Hibionada, D.M. Klimas, A. Schindler, Aliphatic polyesters. I. The degradation of poly(ϵ-caprolactone) in vivo, Journal of Applied Polymer Science 26(11) (1981) 3779-3787.
[114] R.H. Wehrenberg, Lactic acid polymers: strong, degradable thermoplastics, 94:3 (1981).
[115] I. Engelberg, J. Kohn, Physico-mechanical properties of degradable polymers used in medical applications: A comparative study, Biomaterials 12(3) (1991) 292-304.
[116] T.F. Vandamme, R. Legras, Physico-mechanical properties of poly(ε-caprolactone) for the construction of rumino-reticulum devices for grazing animals, Biomaterials 16(18) (1995) 1395-1400.
[117] D.S. Rosa, I.C. Neto, M.R. Calil, A.G. Pedroso, C.P. Fonseca, S. Neves, Evaluation of the thermal and mechanical properties of poly(ε-caprolactone), low-density polyethylene, and their blends, Journal of Applied Polymer Science 91(6) (2004) 3909-3914.
[118] V.M. Correlo, L.F. Boesel, M. Bhattacharya, J.F. Mano, N.M. Neves, R.L. Reis, Hydroxyapatite Reinforced Chitosan and Polyester Blends for Biomedical Applications, Macromolecular Materials and Engineering 290(12) (2005) 1157-1165.
[119] S. Eshraghi, S. Das, Mechanical and microstructural properties of polycaprolactone scaffolds with one-dimensional, two-dimensional, and three-dimensional orthogonally oriented porous architectures produced by selective laser sintering, Acta Biomaterialia 6(7) (2010) 2467-2476.
[120] T. Wehner, U. Wolfram, T. Henzler, F. Niemeyer, L. Claes, U. Simon, Internal forces and moments in the femur of the rat during gait, J Biomech 43(13) (2010) 2473-9.
[121] M. Werner, N.A. Kurniawan, G. Korus, C.V.C. Bouten, A. Petersen, Mesoscale substrate curvature overrules nanoscale contact guidance to direct bone marrow stromal cell migration, Journal of The Royal Society Interface 15(145) (2018) 20180162.
[122] C. Perier-Metz, G.N. Duda, S. Checa, Mechano-Biological Computer Model of Scaffold-Supported Bone Regeneration: Effect of Bone Graft and Scaffold Structure on Large Bone Defect Tissue Patterning, Front Bioeng Biotechnol 8 (2020) 585799.
[123] A. Cipitria, C. Lange, H. Schell, W. Wagermaier, J.C. Reichert, D.W. Hutmacher, P. Fratzl, G.N. Duda, Porous scaffold architecture guides tissue formation, Journal of Bone and Mineral Research 27(6) (2012) 1275-1288.
[124] F. Rossi, H.E. MacLean, W. Yuan, R.O. Francis, E. Semenova, C.S. Lin, H.M. Kronenberg, D. Cobrinik, p107 and p130 Coordinately Regulate Proliferation, Cbfa1 Expression, and Hypertrophic Differentiation during Endochondral Bone Development, Developmental Biology 247(2) (2002) 271-285.

[125] C.l. Colnot, Z. Thompson, T. Miclau, Z. Werb, J.A. Helms, Altered fracture repair in the absence of MMP9, Development 130(17) (2003) 4123-4133.
[126] H.-P. Gerber, T.H. Vu, A.M. Ryan, J. Kowalski, Z. Werb, N. Ferrara, VEGF couples hypertrophic cartilage remodeling, ossification and angiogenesis during endochondral bone formation, Nature Medicine 5(6) (1999) 623-628.
[127] P. Carmeliet, Angiogenesis in health and disease, Nat Med 9(6) (2003) 653-60.
[128] R.J. Klebe, H. Caldwell, S. Milam, Cells Transmit Spatial Information by Orienting Collagen Fibers, Matrix 9(6) (1990) 451-458.
[129] O. Kostyuk, R.A. Brown, Novel spectroscopic technique for in situ monitoring of collagen fibril alignment in gels, Biophys J 87(1) (2004) 648-55.
[130] A. Senk, V. Djonov, Collagen fibers provide guidance cues for capillary regrowth during regenerative angiogenesis in zebrafish, Scientific Reports 11(1) (2021) 19520.
[131] M.G. McCoy, J.M. Wei, S. Choi, J.P. Goerger, W. Zipfel, C. Fischbach, Collagen Fiber Orientation Regulates 3D Vascular Network Formation and Alignment, ACS Biomaterials Science & Engineering 4(8) (2018) 2967-2976.
[132] A.S. Piotrowski-Daspit, B.A. Nerger, A.E. Wolf, S. Sundaresan, C.M. Nelson, Dynamics of Tissue-Induced Alignment of Fibrous Extracellular Matrix, Biophysical Journal 113(3) (2017) 702-713.
[133] W.Y. Wang, A.T. Pearson, M.L. Kutys, C.K. Choi, M.A. Wozniak, B.M. Baker, C.S. Chen, Extracellular matrix alignment dictates the organization of focal adhesions and directs uniaxial cell migration, APL Bioeng 2(4) (2018) 046107.
[134] F. Neto, A. Klaus-Bergmann, Y.T. Ong, S. Alt, A.C. Vion, A. Szymborska, J.R. Carvalho, I. Hollfinger, E. Bartels-Klein, C.A. Franco, M. Potente, H. Gerhardt, YAP and TAZ regulate adherens junction dynamics and endothelial cell distribution during vascular development, Elife 7 (2018).
[135] J. Mehl, S.K. Farahani, E. Brauer, A. Klaus-Bergmann, T. Thiele, A. Ellinghaus, E. Bartels-Klein, K. Koch, K. Schmidt-Bleek, A. Petersen, H. Gerhardt, V. Vogel, G.N. Duda, External Mechanical Stability Regulates Hematoma Vascularization in Bone Healing Rather than Endothelial YAP/TAZ Mechanotransduction, Advanced Science 11(13) (2024) 2307050.
[136] P. Consigliere, E. Iliopoulos, T. Ads, A. Trompeter, Early versus delayed weight bearing after surgical fixation of distal femur fractures: a non-randomized comparative study, Eur J Orthop Surg Traumatol 29(8) (2019) 1789-1794.
[137] D.P.J. Smeeing, R.M. Houwert, J.P. Briet, R.H.H. Groenwold, K.W.W. Lansink, L.P.H. Leenen, P. van der Zwaal, J.M. Hoogendoorn, M. van Heijl, E.J. Verleisdonk, M.J.M. Segers, F. Hietbrink, Weight-bearing or non-weight-bearing after surgical treatment of ankle fractures: a multicenter randomized controlled trial, European Journal of Trauma and Emergency Surgery 46(1) (2020) 121-130.
[138] C. Gaggioli, S. Hooper, C. Hidalgo-Carcedo, R. Grosse, J.F. Marshall, K. Harrington, E. Sahai, Fibroblast-led collective invasion of carcinoma cells with differing roles for RhoGTPases in leading and following cells, Nat Cell Biol 9(12) (2007) 1392-400.
[139] F. Bordeleau, B.N. Mason, E.M. Lollis, M. Mazzola, M.R. Zanotelli, S. Somasegar, J.P. Califano, C. Montague, D.J. LaValley, J. Huynh, N. Mencia-Trinchant, Y.L. Negrón Abril, D.C. Hassane, L.J. Bonassar, J.T. Butcher, R.S. Weiss, C.A. Reinhart-King, Matrix stiffening promotes a tumor vasculature phenotype, Proceedings of the National Academy of Sciences 114(3) (2017) 492-497.
[140] J.H. Wang, E.S. Grood, The strain magnitude and contact guidance determine orientation response of fibroblasts to cyclic substrate strains, Connect Tissue Res 41(1) (2000) 29-36.

[141] L. Krishnan, C.J. Underwood, S. Maas, B.J. Ellis, T.C. Kode, J.B. Hoying, J.A. Weiss, Effect of mechanical boundary conditions on orientation of angiogenic microvessels, Cardiovasc Res 78(2) (2008) 324-32.
[142] L. Trichet, J. Digabel, R. Hawkins, S. Vedula, M. Gupta, C. Ribrault, P. Hersen, R. Voituriez, B. Ladoux, Evidence of a large-scale mechanosensing mechanism for cellular adaptation to substrate stiffness. Proceedings of the National Academy of Sciences of the United States of America, Proceedings of the National Academy of Sciences of the United States of America 109 (2012) 6933-8.
[143] T. Histing, A. Kristen, C. Roth, J.H. Holstein, P. Garcia, R. Matthys, M.D. Menger, T. Pohlemann, In vivo gait analysis in a mouse femur fracture model, J Biomech 43(16) (2010) 3240-3.
[144] R. Schipani, D.R. Nolan, C. Lally, D.J. Kelly, Integrating finite element modelling and 3D printing to engineer biomimetic polymeric scaffolds for tissue engineering, Connective Tissue Research 61(2) (2020) 174-189.
[145] G. Nasello, A. Vautrin, J. Pitocchi, M. Wesseling, J.H. Kuiper, M.Á. Pérez, J.M. García-Aznar, Mechano-driven regeneration predicts response variations in large animal model based on scaffold implantation site and individual mechano-sensitivity, Bone 144 (2021) 115769.
[146] M. Bohner, R.J. Miron, A proposed mechanism for material-induced heterotopic ossification, Materials Today 22 (2019) 132-141.
[147] H. Wang, W. Zhi, X. Lu, X. Li, K. Duan, R. Duan, Y. Mu, J. Weng, Comparative studies on ectopic bone formation in porous hydroxyapatite scaffolds with complementary pore structures, Acta Biomaterialia 9(9) (2013) 8413-8421.
[148] Y.-C. Chiu, M.-H. Cheng, H. Engel, S.-W. Kao, J.C. Larson, S. Gupta, E.M. Brey, The role of pore size on vascularization and tissue remodeling in PEG hydrogels, Biomaterials 32(26) (2011) 6045-6051.
[149] S. Van Bael, Y.C. Chai, S. Truscello, M. Moesen, G. Kerckhofs, H. Van Oosterwyck, J.P. Kruth, J. Schrooten, The effect of pore geometry on the in vitro biological behavior of human periosteum-derived cells seeded on selective laser-melted Ti6Al4V bone scaffolds, Acta Biomaterialia 8(7) (2012) 2824-2834.
[150] N. Baeyens, S. Nicoli, B.G. Coon, T.D. Ross, K. Van den Dries, J. Han, H.M. Lauridsen, C.O. Mejean, A. Eichmann, J.-L. Thomas, J.D. Humphrey, M.A. Schwartz, Vascular remodeling is governed by a VEGFR3-dependent fluid shear stress set point, eLife 4 (2015) e04645.
[151] M.N. Nakatsu, R.C.A. Sainson, S. Pérez-del-Pulgar, J.N. Aoto, M. Aitkenhead, K.L. Taylor, P.M. Carpenter, C.C.W. Hughes, VEGF121 and VEGF165 Regulate Blood Vessel Diameter Through Vascular Endothelial Growth Factor Receptor 2 in an in vitro Angiogenesis Model, Laboratory Investigation 83(12) (2003) 1873-1885.
[152] C. Korn, Hellmut G. Augustin, Mechanisms of Vessel Pruning and Regression, Dev Cell 34(1) (2015) 5-17.
[153] M. Paris, A. Götz, I. Hettrich, C.M. Bidan, J.W.C. Dunlop, H. Razi, I. Zizak, D.W. Hutmacher, P. Fratzl, G.N. Duda, W. Wagermaier, A. Cipitria, Scaffold curvature-mediated novel biomineralization process originates a continuous soft tissue-to-bone interface, Acta Biomaterialia 60 (2017) 64-80.
[154] Y. Wang, T. Azaïs, M. Robin, A. Vallée, C. Catania, P. Legriel, G. Pehau-Arnaudet, F. Babonneau, M.-M. Giraud-Guille, N. Nassif, The predominant role of collagen in the nucleation, growth, structure and orientation of bone apatite, Nature Materials 11(8) (2012) 724-733.
[155] Y. Du, S.C. Herath, Q.G. Wang, D.A. Wang, H.H. Asada, P.C. Chen, Three-Dimensional Characterization of Mechanical Interactions between Endothelial Cells and Extracellular Matrix during Angiogenic Sprouting, Sci Rep 6 (2016) 21362.

[156] C. Yoon, C. Choi, S. Stapleton, T. Mirabella, C. Howes, L. Dong, J. King, J. Yang, A. Oberai, J. Eyckmans, C.S. Chen, Myosin IIA-mediated forces regulate multicellular integrity during vascular sprouting, Mol Biol Cell 30(16) (2019) 1974-1984.

Acknowledgements

These acknowledgements come at the end of this thesis, yet they are probably the pages that mean the most to me. The years behind these pages have certainly been filled with simulations, papers and deadlines, but also a lot of growth, laughter and countless memorable moments shared with truly wonderful people. I would like to express my deepest gratitude to each of them.

First and foremost, I would like to thank my supervisor Sara Checa. Thank you for your continuous support and guidance throughout these years, both scientifically and personally, and for all the opportunities you gave me along the way. I believe that a research group reflects its leader and I am very grateful I was part of the most supportive, brilliant, and friendly one. I would also like to thank Georg Duda for his valuable feedback, insightful discussions, and support throughout these years.

I want to deeply thank all my collaborators: Ansgar Petersen, Erik Brauer, Julia Mehl, Mounir Benamar, Petra Knaus, Daniel J. Kelly, Kian Eichholz, Fiona Freeman. This thesis would not have been possible without your scientific input, constructive discussions, and contributions.

I am incredibly grateful to have been part of such a talented and supportive team as the Computational Mechanobiology group. Vincenzo, Mahdi, Siddarth, Vahid, Özgür, Philipp, Giorgio, thank you all for always being willing to help, for the endless meetings making sure everyone received as much feedback as possible, but also for the wonderfully unproductive office days, the extremely long yet regenerating coffee breaks, the laughter, and all the moments we shared outside of work. Working with you never felt like being surrounded by colleagues only.

Very special thank yous also to Britt, Sofia and Zeynep, although you were only part of the group temporarily, the connection we have built and your friendship mean a lot to me.

Many thanks to the Hamburg group for welcoming me so warmly. Although I joined only recently, you made me feel part of the team from the very beginning.

Daniela, Vincenzo and Mahdi… where do I even begin? I will just say thank you for being my Berlin family, for giving me the comfort of knowing we are always there for each other, no matter what.

ACKNOWLEDGEMENTS

Anni, Annie, Andreia, Katriina, Lea, Constantin, thank you all for all the fun, trips, spontaneous adventures, workouts, dinners, parties and so much more. You made Berlin feel like home and these years far more enjoyable.

Simona and Giulia, whenever we have managed to meet, it has always been a source of lightness. Thank you for making life feel simple, fun, and carefree again, just as it did during our days in Milan.

Alessio, thank you for your loyalty, genuine support, and constant presence in my life in the past 13 years. I am very proud of you as I know you are proud of me. Federico and Christian, thank you for all the laughter, adventures and memories during our ski trips, New Year's Eve celebrations, birthdays or whenever we manage to meet. Despite living in three different countries, we have always shown up for one another when it mattered most.

My lifelong friends, Chiara, Sara, Greta, Martina, Silvia, Irene, Margherita. Thank you for always being there for me, cheering for me and especially for reminding me of my roots.

Chiara, thank you for the deep understanding between us, for our long phone calls venting about everything and nothing, for always listening without judgement.

My sister Giulia, thank you for teaching me, through your example, how to be braver and stand up for myself.

Mum and dad, thank you for the freedom and trust you gave me from the very beginning, for always supporting my choices and truly believing in me.

And lastly, Fabrizio, you have been my greatest teammate throughout these years. Thank you for being my biggest fan during good moments, but especially for your patience, understanding, and support during the more difficult ones. Thank you for always listening, for helping me keep things in perspective, and for making everyday life a little lighter and a lot more fun.